Utilization of nanostructured iron sulfides to remove metals and nutrients from wastewater

Yan Yang

Supervisor: Prof. Xinmin Zhan

Co-Supervisors: Prof. Tianhu Chen, Hefei University of Technology, China

Dr. Gavin Collins

A thesis submitted in partial fulfillment of the requirements for the degree of

Doctor of Philosophy

in the College of Engineering and Informatics

Submission date: Feb, 2017

Table of Contents

Declarations

This thesis or any part thereof, has not been, or is not currently being submitted for any degree at any other university.

Yan Yang

The work reported herein is as a result of my own investigations, except where acknowledged and referenced.

Yan Yang

Acknowledgments

First, I would like to thank China Scholarship Council (No. 201306690001) and Prof. Tianhu Chen, they give me the opportunity to start my Ph.D. studies in Ireland. I would like to express my special appreciation and thanks to my supervisor Prof. Xinmin Zhan for the continuous support of my Ph.D. studies. He is not only a supervisor in teaching, but also a supervisor in life. He guided me the way of doing research, writing papers, integrating into the local society, etc. The primary value of doing my Ph.D. is to have him as my supervisor. Special thanks to his wife Mrs. Jin Xu and their kids Daning and Aining, who made me feel at home and gave me a strong sense of belonging.

I would also like to thank Prof. Padraic O'Donoghue and Dr. Marcus Keane as the members of my graduate research committee for their insightful comments on the progress of the project. I would also like to thank Dr. Gavin Collin, Dr. Sean Gerrity, and Dr. Liam Morrison for their support of the project, widening my research from perspectives in microbiology and microscopy.

I would also like to thank my Irish, Brazilian, and Chinese colleagues who helped me a lot in work and life over the last three years, making my life abundant.

At the end, I would like express appreciation to my loving family. Words cannot express how grateful I am to my parents, brother and sister, and my boyfriend Pei Tao and his family. Thank you for all of your support of my overseas study, making me feel so beloved.

Publications

1. Application of iron sulfides (Pyrite, Pyrrhotite, and Mackinawite) into wastewater treatment, preparing for submission to Reviews in Environmental Science and Bio/Technology (Chapter 2).

2. Yang, Y., Chen, T., Li, P., Qing, C., Xie, Q., & Zhan, X. (2016). Immobilization of copper under an acid leach of colloidal pyrite waste rocks by a fixed-bed column. Environmental Earth Sciences, 75 (3), 1-8 (Chapter 3).

3. Yang Y., Chen T.H., Li P., Liu H. B., Xie J. J., Xie Q.Q., Zhan X.M., (2014), Removal and recovery of Cu and Pb from single-metal and Cu–Pb–Cd–Zn multimetal solutions by modified pyrite: fixed-bed columns, Industrial & Engineering Chemistry Research, 53 (4), 18180-18188 (Chapter 4).

4. Yang, Y., Chen, T., Li, P., Xie, Q., & Zhan, X. (2016). Cu removal in real acid mine drainage by modified pyrite: batch and column experiments. Mine Water and the Environment, accepted (Chapter 5).

5. Yang, Y., Chen, T.H, Morrison, L., Gerrity, S., Collins, G., Porca, E., Li, R.H., Zhan, X.M. (2016). Nanostructured pyrrhotite supports autotrophic denitrification for simultaneous nitrogen and phosphorus removal from wastewater, submitted to Scientific Report (Chapter 7).

Abstract

Wastewater containing metals and nutrients is a global environmental issue, threatening human life and natural ecosystems. Iron sulfide minerals are abundant on Earth and are commonly discarded as mine wastes, causing acid mine drainage (AMD). Thus, economically beneficial use of iron sulfides is of great significance, and one option is to use iron sulfide minerals to develop functional environmental materials, which can be applied into environmental pollution control. Nanostructured pyrrhotite (NPyr) was manufactured by calcination of pyrite mineral under N_2 atmosphere. This Ph.D. research was aimed at the assessment of efficiencies and mechanisms of NPyr into metal and nutrient removals from wastewater using laboratory-scale column reactors (diameter, 10 mm; height, 50 cm).

NPyr was added to Fixed–bed columns and used to test for the removal and recovery of Cu, Pb, Cd, and Zn from the single–metal and Cu–Pb–Cd–Zn multi–metal solutions. Results showed that the removal capacities of Cu and Pb were 77.42 $mg \cdot g^{-1}$ and 73.68 $mg \cdot g^{-1}$ NPyr from single–metal solutions, and were 30.79 $mg \cdot g^{-1}$ and 10.86 $mg \cdot g^{-1}$ NPyr from the Cu–Pb–Cd–Zn multi–metal solution. The Cu and Pb contents in the used NPyr particles were up to 17.4% and 15.4% in the single sorption column, and 6.8% and 2.5% in the multi–metal sorption column, respectively. The contents of Cu and Pb were high enough, so it would be economically feasible to extract Cu and Pb from the used NPyr particles by means of direct extractive metallurgy. The sequential extraction of the metals, X–Ray diffraction (XRD), and transmission electron microscopy (TEM) analyses showed that the major mechanisms for Cu and Pb removal by NPyr were precipitation and dissolution reactions via the formation of

covellite (CuS) and galena (PbS). Long–term Cu removal from real acid mine drainage (AMD) was investigated using a two-column reactor system consisting of Column A (added with limestone as neutralizer) and Column B (added with NPyr). The breakthrough capacity was 21.93 mg $Cu \cdot g^{-1}$ NPyr, and the maximum Cu content was up to 9.2% in the used NPyr in Column B.

The mechanisms and efficiencies of NPyr-based autotrophic denitrification for simultaneous nitrogen (N) and phosphorus (P) removal from secondary treated wastewater was investigated using two identical biofilters. The hydraulic retention time (HRT) of the nanostructured pyrrhotite autotrophic denitrification biofilters (PADBs) was gradually reduced from 7.2 to 0.6 h over a 536-day trial. Average concentrations of N of 0.05 $mg \cdot L^{-1}$ and P of 0.03 $mg \cdot L^{-1}$ in the treated effluent were achieved at a HRT of 1.2 h when treating real secondary effluent which contained N of 13.81 $mg \cdot L^{-1}$ and P of 2.44 $mg \cdot L^{-1}$. The low concentrations of N and P achieved in the nanostructured PADB effluent at very short HRTs indicate the potential of this technology for tertiary wastewater treatment and in meeting strict discharge standards. High-throughput sequencing of 16S rRNA genes showed that *Thiobacillus* was the most dominant genus (up to 87% relative abundance) in the PADBs. TEM analysis of the used NPyr indicated that P was mainly removed by the precipitation of $FePO_{4(s)}$. A significant SO_4^{2-} reduction with 32.50–58.01 $mg \cdot L^{-1}$ was observed in the nanostructured PADBs treating real secondary effluent. This observation highlights the sustainability of the nanostructured PADB technology.

This Ph.D. study shows the potential of synthesized NPyr as i) a novel, cost-effective sorbent for metal removal and recovery, in particular, Cu, from real AMD, and ii) biofilm substratum for autotrophic denitrification in nanostructured PADB technology as tertiary treatment for wastewater. It is suggested that the application of NPyr into wastewater treatment should be demonstrated in a large scale reactor.

Keywords: Acid mine drainage; Autotrophic denitrification; Biofilters; Fixed–bed column; Iron sulfides; Metal removal; Nanostructured; Nutrient removal; Thiobacillus

List of Tables

List of Figures

List of Nomenclature

A: cross-section area of biofilm substratum, mL

C_0: influent concentrations, mmol·L^{-1}

C_t: effluent concentrations, mmol·L^{-1}

$C_{NO_3^- - N,\ i}$: influent/initial concentration of NO_3^-–N, mg·L^{-1}

$C_{NO_3^- - N,\ t}$: concentrations of NO_3^--N at time t or different heights of the biofilters, mg·L^{-1}

$C_{NO_2^- - N,\ t}$: concentrations of NO_2^--N at different heights of the biofilters, mg·L^{-1}

H: height of the biofilters, cm

k_1: half-order reaction constants for NO_3^-–N, $mg^{1/2}L^{1/2}h$

k_2: half-order reaction constants for NO_2^-–N, $mg^{1/2}L^{1/2}h$

k: first-order reaction constants for NO_3^-–N, $mg\ L^{1/2}h$

M: relative atomic mass for metals

n: porosity of the added medium

Q: influent flow rate, $mL \cdot h^{-1}$

q: breakthrough capacity, $mg \cdot g^{-1}$

t_h: empty bed residence time, h

V_1: volume of the added medium in the column, mL

V_2: cumulative volume of treated water, L

X: mass of sorbent packed in the column, g

List of Abbreviations

AMD: Acid Mine Drainage

BET: Brunauer, Emmett, and Teller

CPWR: Colloidal Pyrite Waste Rocks

COD: Chemical Oxygen Demand

DO: Dissolved Oxygen

HRT: Hydraulic Retention Time

HRTEM: High Resolution Transmission Electron Microscopy

NMDS: Non-Metric Multidimensional Scaling

NPyr: Nanostructured Pyrrhotite

PADBs: Pyrrhotite Autotrophic Denitrification Biofilters

PCR: Polymerase Chain Reaction

PAHs: Polycyclic Aromatic Hydrocarbons

SSA: Specific Surface Area

SRB: Sulfate Reducing Bacteria

SEM–EDX: Scanning Electron Microscopy with X–ray Energy Dispersive Spectrometer

TON: Total Oxidized Nitrogen

TRFLP: Terminal Restriction Fragment Length Polymorphism

WWTPs: Wastewater Treatment Plants

XRF: X–ray Fluorescence

XRD: X–ray Diffraction

XPS: X–ray Photoelectron Spectroscopy

Chapter 1
Introduction

1.1 Background

Iron sulfides refer to a range of natural and synthetic chemical compounds composed of iron and sulfur. Natural iron sulfide minerals are formed by the reaction of iron oxides/hydroxides with sulfides produced by sulfate-reducing bacteria (SRB) under anoxic conditions (Jeong et al., 2007; Rickard and Luther, 2007). Pyrite (FeS_2) and pyrrhotite ($Fe_{1-x}S$, $0<x<0.125$) have been acknowledged as the two most abundant iron sulfides on the Earth. Colloidal pyrite is a kind of cryptocrystalline pyrite with nano-sized and submicron-sized crystals (Fig. 1.1a). Due to its nano-size property, colloidal pyrite is expected to be more active than normal pyrite mineral (Xie et al., 2014). Pyrite and pyrrhotite used to be the raw materials for the production of sulfuric acid. At present, it's more economical to use other sources (such as off-gas, sulfur, and gypsum) to manufacture sulfuric acid, so pyrite and pyrrhotite are mostly considered as gangue being disposed of in mine wastes (Chiriță & Rimstidt, 2014). They are easily oxidized, resulting in a discharge of significant amounts of Fe, Al, SO_4^{2-}, and toxic metals into the drainage, which is well known as acid mine drainage (AMD) (Sahoo et al., 2013). AMD is a serious and persistent environmental problem, which leads to contamination of surface and groundwater bodies, threatening living beings (Pierre Louis et al., 2015; Sahoo et al., 2013). According to recent studies, nearly 5×10^9 tonnes of mill tailings are generated resulting from mining activities per year globally (Lu & Wang, 2012). In Ireland, Gray and Delaney (2010; 2008) have reported that the Avoca River located in Co. Wicklow has been contaminated by AMD, resulting in extremely poor river water quality and significant losses of biodiversity. Therefore, it's of increasing importance to find alternative beneficial applications of pyrite and pyrrhotite. One alternative application is to utilize pyrite and pyrrhotite to remove contaminants (e.g. metals and nutrients) from wastewater.

Pyrite and pyrrhotite have been found to be able to remove divalent metals (e.g. Cu^{2+}, Cd^{2+}, Pb^{2+}, and Hg^{2+}, etc) from aqueous solutions through adsorption, and/or precipitation of insoluble metal sulfides (Borah & Senapati, 2006; Bower et al., 2008; Lu et al., 2006). Recently, natural pyrrhotite mineral has been used as biofilm substrum in pyrrhotite autotrophic

denitrification biofilters (PADB) to simultaneously reducing nitrogen (TON-N) and phosphorus (PO_4^{3-}) in secondary municipal effluent from 21.1 and 2.6 $mg \cdot L^{-1}$ to 1.9, and 0.3 $mg \cdot L^{-1}$, respectively (Li et al., 2016). However, the high symmetry of and the strong S–S bond in the crystal structure of natural pyrite mineral and the low specific surface areas of natural iron sulfides cause i) low sorption capacities because of their low chemical reactivity (Chen et al., 2014a), and (ii) a long hydraulic retention time (HRT) of up to 24 h needed to achieve efficient nutrient removal for PADBs, making this technology impractical to be used in mainstream wastewater treatment plants (WWTPs).

To improve the chemical activity of pyrite and pyrrhotite and to promote their engineering applications, nanostructured pyrrhotite (NPyr) was developed by calcining pyrite, colloidal pyrite, or pyrite and limonite (FeO(OH)) at 500−650 °C for 1 h in a N_2 atmosphere. The obtained nanostructured pyrrhotite has a high specific surface area (SSA) due to its porous structures (Chen et al., 2016; Chen et al., 2013b; Chen et al., 2014a). SSA is about 10 $m^2 \cdot g^{-1}$ for NPyr, and is less than 0.02 $m^2 \cdot g^{-1}$ for original normal pyrite mineral (Chen et al., 2014b). The larger surface area and porous structure of NPyr (Fig. 1.1b) can expose more functional groups and facilitate a greater capacity and kinetic rate when NPyr is used to remove metals and nutrients from wastewater. Therefore, it's worth investigating the applications of natural and synthesized nanostructured iron sulfides (i.e. nano-sized colloidal pyrite and NPyr) into the removal of metals and nutrients.

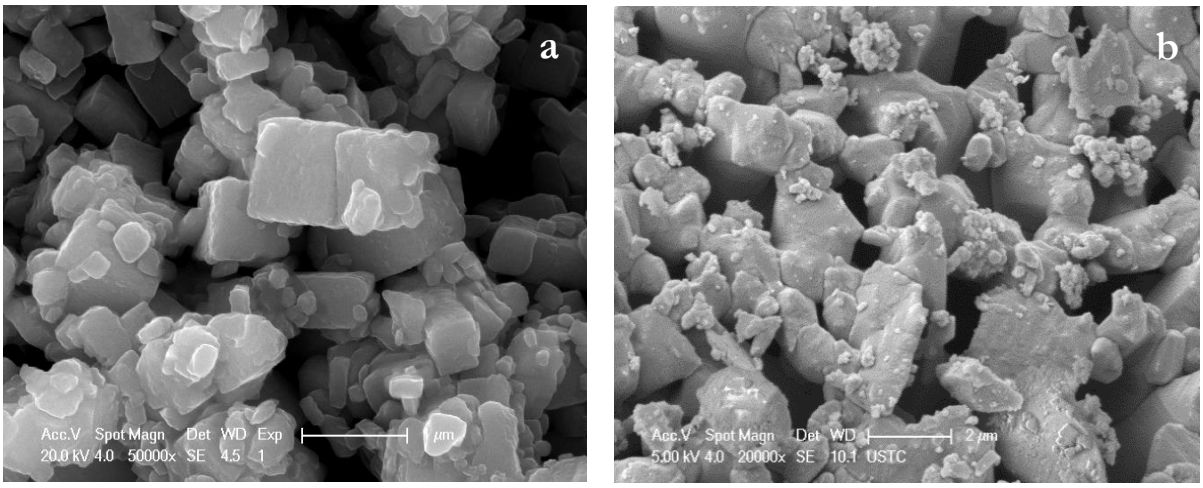

Figure 1.1: FE–SEM micrographs of the natural colloidal pyrite (a) and the nanostructured pyrrhotite (b)

1.2 Research Objectives

The primary aim of this research is to explore the application of natural nano-sized colloidal pyrite and NPyr as functional materials for the removal of metals and nutrients from wastewater and to study the removal mechanisms.

The specific objectives for the application of colloidal pyrite and NPyr into metal removal include:

1) to evaluate metal removal from wastewater by natural colloidal pyrite.
2) to investigate the sorption capacities and mechanisms of NPyr for metal removal from solutions containing single metal or multi–metals.
3) to evaluate the efficiency of NPyr in metal removal and recovery from real AMD.

For the application of NPyr as biofilm substratum in nanostructured PADBs into nutrient removal from wastewater, the specific objectives are:

1) to investigate the mechanisms and performance of simultaneous nitrogen (N) and phosphorus (P) removal in nanostructured PADBs at different HRTs.

2) to operate PADBs with real secondary municipal effluent collected from a local municipal WWTP at different HRTs.

1.3 Contribution to Knowledge

The core value of this Ph.D. study is to use pyrite (FeS_2) and pyrrhotite ($Fe_{1-x}S$) as environmental materials, in line with the national and European waste management policies to move towards a more resource-efficient and circular economy. In order to increase the SSA of natural iron sulfides, a simple method was developed to synthesize NPyr with porous structures. The NPyr should have increased efficiencies in metal and nutrient removals from wastewater than natural iron sulfides, and is worthy of investigation. This Ph.D. research is the first to systematically assess NPyr efficiencies in contaminant removal and to explore the mechanisms associated. Therefore, this research will make significant contributions to environmental research.

1.4 Procedures

The research contents consisted of synthesis of nanostructured iron sulfides, conducting laboratory-scale trials testing metal and nutrient removals, and characterization of iron sulfides using a series of techniques (Fig. 1.2). The procedures are briefed here, but will be detailed in individual chapters.

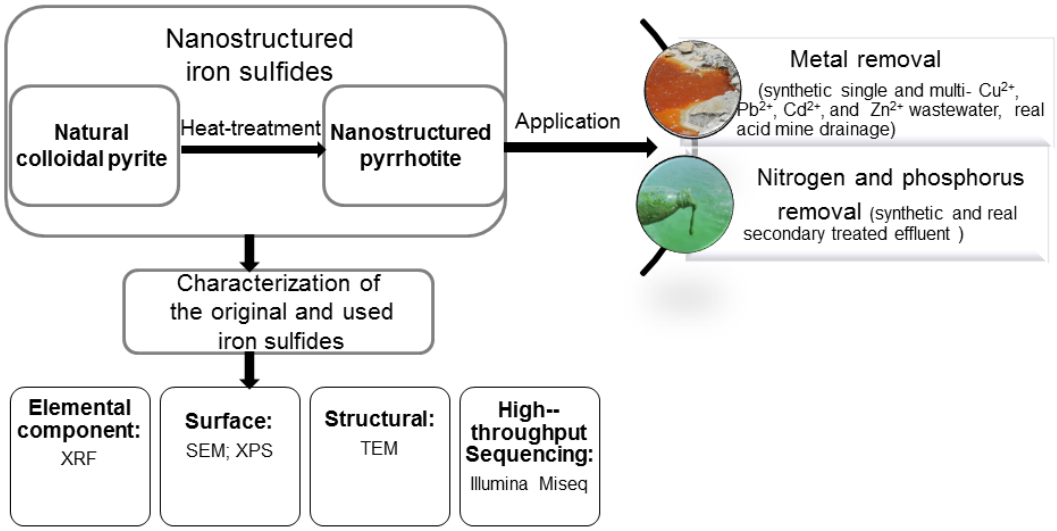

Figure 1.2: Research procedure

1.4.1 Synthesis of nanostructured pyrrhotite

Natural colloidal pyrite and pyrite minerals were collected from Xinqiao Mine of Tongling City in Anhui Province, China. The preparation of NPyr sorbents followed the method described by Chen et al. (2014b). The obtained NPyr particles were then stored in a vacuum desiccator until use.

1.4.2 Continuous column trials

The removal of metals and nutrients was studied with fixed-bed column reactors in laboratory-scale at room temperature. 50 g of iron sulfide particles were added into the columns (Fig. 1.3). When investigating metal removal, synthetic metal wastewater, and real AMD wastewater which was collected from a pond of Xiangshan Mine located in Ma'an Shan, Anhui, China, were pumped to the column reactors and treated. For nutrient removal, real secondary municipal effluent was collected from a local municipal WWTP in Galway, Ireland, and was

treated in nanostructured PADB where NPyr was used as the biofilm substratum for autotrophic denitrification. The description of these experimental systems is detailed in individual chapters.

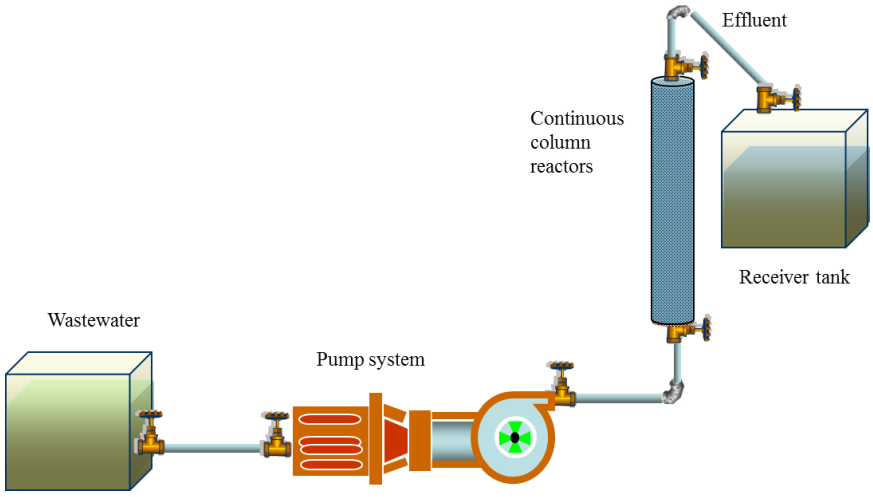

Figure 1.3: Experimental set-up of continuous column reactors for metal and nutrient removal

1.4.3 Characterization of iron sulfides

The original and used iron sulfides sampled after the trials were analysed using a number of techniques (Fig. 1.2). The chemical and mineralogical composition of iron sulfides were determined by X ray fluorescence (XRF) (Shimadzu–1800, Japan) and X–ray diffraction (XRD) (Dandong Haoyuan DX–2700, China). The surface morphology and chemical composition of iron sulfides were characterized by scanning electron microscopy (SEM) integrated with energy dispersive X–ray spectrometer (EDX) analysis (SEM–EDX, Hitachi S–4700, Japan). In addition, the outermost few nanometres layer of iron sulfides' surface was determined using X–ray photoelectron spectroscopy (XPS, Thermo ESCALAB–250, America). High resolution

transmission electron microscopy with energy dispersive X–ray (EDX) (HRTEM, JEOL–2100F, Japan) was used to determine the morphology, structure, element distribution of iron sulfides. High-throughput sequencing of 16S rRNA genes via the Illumina Miseq platform was used to investigate the bacterial community in the biofilm grown on NPyr in the nanostructured PADB.

1.5 Structure of Dissertation

This dissertation comprises 8 chapters:

Chapter 2 reviews the physicochemical properties of iron sulfides and their application for wastewater treatment.

Chapter 3 investigates Cu removal by natural colloidal pyrite waste rocks from synthetic low–concentration Cu wastewater.

Chapter 4 studies the removal and recovery of Cu, Pb, Cd, and Zn from single and multi–metal solutions by NPyr.

Chapter 5 explores Cu removal and recovery from real AMD by NPyr.

Chapter 6 presents an efficient and cost-effective method to enrich sulfur-based autotrophic denitrifiers from anaerobic sludge collected from a local WWTP.

Chapter 7 evaluates simultaneous nitrogen and phosphorus removal in NPyr-packed biofilters by autosulfurotrophic denitrification process.

Finally, Chapter 8 presents the conclusions drawn from all the lab studies described in Chapters 3–7. Recommendations for further research are also put forward.

Chapter 2
Literature Review

2.1 Overview

This Chapter presents a review of physicochemical properties of natural and synthesized iron sulfides (i.e. pyrite, pyrrhotite, and mackinawite), and of their applications into pollutant removal from wastewater. These pollutants include toxic metals (i.e. lead, mercury, cadmium, and hexavalent chromium) and metalloid (i.e. arsenic), radionuclides (i.e. uranium and selenium), organic contaminants (i.e. chlorinated organic pollutants, benzene and polycyclic aromatic hydrocarbons), and nutrients (i.e. nitrogen and phosphorus).

2.2 Introduction

Iron sulfide minerals include a diverse group of solids and dissolved complexes, such as pyrite (FeS_2, cubic), marcasite (FeS_2, orthorombic), greigite (Fe_3S_4, cubic), smythite (Fe_9S_{11}, hexagonal), mackinawite (FeS_{1-x}, $0<x<0.07$, tetragonal), pyrrhotite ($Fe_{1-x}S$, $0<x<0.125$, monoclinic and hexagonal), and troilite (FeS, hexagonal) (Rickard & Luther, 2007).

Pyrite and pyrrhotite are the most abundant in mantle rocks and meteorites. Mackinawite mineral is only formed in strongly anoxic sediments, active hydrothermal systems or near the midocean ridge (Mullet et al., 2002). Well-crystallized mackinawite is rarely found in sediments (Morse & Rickard, 2004), as mackinawite is prone to transformation to more stable phases like pyrite and pyrrhotite. Therefore, some researchers have explored physicochemical and biological approaches to synthesize mackinawite nanoparticles with high reactivity and availability, such as reaction of sulfide solution with metallic iron or reaction of sulfide solution with ferrous iron solution via sulfate reducing bacteria-assisted approach (Watson et al., 2000), hydrothermal process (Widlera & Seward, 2002), dendrimer-stabilization (Shi et al., 2006), chemical vapor condensation (Ha et al., 2006), biopolymer-stabilization (Xiong et al., 2009), and high-energy mechanical milling (Chin et al., 2005). Amongst these methods, the precipitation from an Fe^{2+} solution by adding Na_2S at a controlled pH is commonly used in the laboratory (Lennie, 1995). Pyrite and pyrrhotite, the two most ubiquitous iron sulfide minerals,

and mackinawite, laboratory synthesized nanocrystalline iron sulfide, have been extensively investigated as representative iron sulfides in the removal of a variety of contaminants from wastewater. The reducibility of surface iron and sulfur and functional groups (e.g. ≡S-H) on iron sulfides have been used to remove inorganic contaminants (metals and radionuclides). Iron sulfides, providing Fe^{2+}, can act as catalyst for degrading organic contaminants (chlorinated organic pollutants, benzene, and polycyclic aromatic hydrocarbons). Iron sulfides also contain reduced sulfur which can support autotrophic denitrification to remove nutrients (nitrogen and phosphorus). The overall goal of this chapter is to review the application of iron sulfides into wastewater treatment, and to elucidate the removal/degradation efficiency and the mechanism behind the removal of contaminants from wastewater by iron sulfides.

2.3 Physicochemical Propertites of Iron Sulfides

2.3.1 Structure and surface properties of iron sulfides

The crystal structures and the SEM micrographs of pyrite, pyrrhotite, and mackinawite are shown in Fig. 2.1. Pyrite displays a NaCl-type structure (Fig. 2.1 a). The two S atoms which form a dumbbell-shaped symmetry $[S_2]^{2-}$ structure are situated at the cube center and the midpoints of cube edges, whereas the Fe atoms are located at the corners and face centers. The average Fe–S distance is 2.26 Å (Fujii et al., 1986). The strong S-S bond and the symmetric cubic crystal structure render pyrite quite stable compared with pyrrhotite, which has Fe vacancy geometries, and mackinawite, which is sulfur-deficient in crystal structures (Belzile et al., 2004; Jeong et al., 2007). The SEM micrograph illustrates micrometer-scale particles in the range of 30–100 μm in the pyrite particles (Fig. 2.1 b).

Pyrrhotite displays various superstructures based on a NiAs structure (Fig. 2.1 b), which is caused by the ordered Fe vacancy geometries in the nonstoichiometric composition, with an average Fe–Sdistance of 2.50 Å (Belzile et al., 2004). Pyrrhotite has two basic subgroups: the

hexagonal pyrrhotite, which tends to be iron-rich (in the range of 47.4–48.3 at.%) with an empirical formula expressed as $Fe_{10}S_{11}$, and the monoclinic pyrrhotite, which tends to be iron-poor (in the range of 46.5–46.8 at.%) with an empirical formula expressed as Fe_7S_8. SEM micrograph of pyrrhotite shows only a fracture surface of a pyrrhotite particle at 10 μm scale, indicating pyrrhotite consists of bigger crystalline particles than pyrite particles (Fig. 2.1 d).

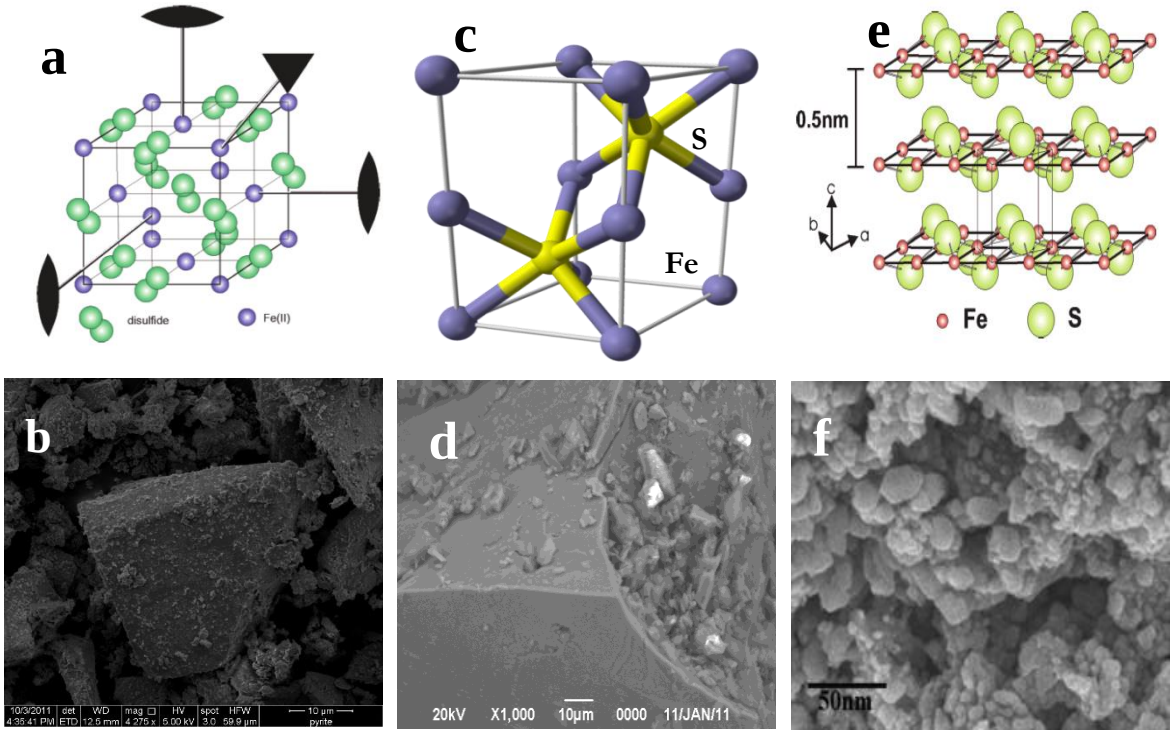

Figure 2.1: Crystal structure elements and SEM micrographs of pyrite (a, b), pyrrhotite (c, d), and mackinawite (e, f)

Mackinawite, a metastable sulfur-deficient iron sulfide, displays a tetragonal layer structure (Fig. 2.1 c) with each Fe atom coordinated by four S atoms, and the bonding length of Fe–S is 2.24 Å (Jeong et al., 2007). A SEM micrograph of synthesized nanocrystalline mackinawite (Fig. 2.1

f) reveals nanometer-sized particles are stacked irregularly, resulting in an intergranular porous structure (Chen et al., 2015). The SSA of mackinawite is 424 ± 130 $m^2 \cdot g^{-1}$, significantly higher than SSA of pyrite (i.e. 0.02–41 $m^2 \cdot g^{-1}$) and pyrrhotite (i.e. 0.01–2.1 $m^2 \cdot g^{-1}$) due to its nanocrystalline structure (Jeong et al., 2008).

The basic physicochemical properties of pyrite, pyrrhotite, and mackinawite are listed in Table 2.1. Pyrite and mackinawite are weakly diamagnetic, while pyrrhotite is magnetic. The magnetic properties of pyrrhotite are variable depending on the Fe/S ratio. Monoclinic pyrrhotite is ferromagnetic with a magnetic susceptibility of 4973 × 10^{-8} $m^3 \cdot kg^{-1}$; hexagonal pyrrhotite is approximately antiferromagnetic (Chen et al., 2013b; Watson et al., 2000). This property of pyrrhotite can be used to separate it from aqueous solutions by magnetic separation, and from other minerals by magnetic flotation.

In aqueous solutions, iron sulfides have been identified to have at least two different functional groups; they are surface hydroxyl (≡Fe-OH) and sulfhydryl functional groups (≡S-H) (Bostick & Fendorf, 2003; Mullet et al., 2004). ≡S-H bonds are dominant over ≡Fe-OH bonds at pH< 10 in solutions (Wolthers et al., 2005a). ≡S-H groups are Lewis bases, which have a great affinity to Lewis acids, such as divalent metals (e.g. Hg^{2+}, Cd^{2+}, Cu^{2+}). Therefore, these metals are expected to be adsorbed via surface complexation with ≡S-H functional groups on iron sulfides (Jean & Bancroft, 1986; Jeong et al., 2010c; Moyes et al., 2002; Patterson et al., 1997), and the details will be discussed in Section 2.3.1.1. The reductive surface iron and sulfur in iron sulfides can reduce electron-poor metals like hexavalent chromium (Section 2.3.1.1) and redox-sensitive radionuclides (Section 2.3.1.2) in wastewater, with production of oxidized surface iron and sulfur species (e.g. Fe^{3+}–O, Fe^{3+}–S, and SO_4^{2-}).

Table 2.1: Basic structures and physicochemical properties of pyrite, pyrrhotite, and mackinawite

Iron sulfides	Structure[a]	Physicochemical properties		
		Magnetism	Specific surface area	Others
Pyrite (FeS_2)	Cubic	diamagnetic	0.02–41 $m^2 \cdot g^{-1}$ [b]	Solubility: sparingly soluble; Active surface groups and species: iron(II) hydroxyl groups (≡FeOH), and sulfhydryl groups (≡ SH); reduced Fe and S species; pHzpc: below pH 3.3[e]
Pyrrhotite ($Fe_{1-x}S$)	Monoclinic Fe_7S_8; Hexagonal $Fe_{10}S_{11}$	magnetic	0.01–2.1 $m^2 \cdot g^{-1}$ [c]	
Mackinawite (FeS_{1-x})	Tetragonal	diamagnetic	276–424 ± 130 $m^2 \cdot g^{-1}$ [d]	

a: (Rickard & Luther, 2007) (Snowball & Torri, 1999)**;**

b: (Behra et al., 2001; Bostick & Fendorf, 2003; Bulut et al., 2013; Chen et al., 2014b; Han et al., 2013; Kang et al., 2011; Yang et al., 2014a)

c: (Chiriţă & Rimstidt, 2014; Janzen et al., 2000)

d: (Jeong et al., 2008; Renock et al., 2009)

e: (Bebie et al., 1998; Kantar et al., 2015b; Lin & Huang, 2008; Widlera & Seward, 2002; Wolthers et al., 2005a)

Generally, iron sulfides themselves have low solubility and dissolution rates. The dissolution rates of pyrite and pyrrhotite were in the range of 0–2 × 10^{-8} $mol \cdot m^{-2} \cdot s^{-1}$ and 1 × 10^{-8}–2 × 10^{-5}

$mol \cdot m^{-2} \cdot s^{-1}$ respectively, in deoxygenated $HClO_4$ at a pH of 1 at 50 °C (Thomas et al., 2000). It was much higher for mackinawite with up to 0.5×10^{-3} $mol \cdot m^{-2} \cdot s^{-1}$ in HCl at a pH of 2 (Chiriță & Schlegel, 2015). When pH is below 3, a proton-promoted dissolution of pyrrhotite (Eq. 2.1) and mackinawite (Eq. 2.2) results in production of H_2S (Belzile et al., 2004; Chiriță & Rimstidt, 2014; Ozverdi & Erdem, 2006).

$$\mathbf{Fe_{1-x}S + 2\,(1-x)H^+ \rightarrow (1-x)\,Fe^{2+} + (1-x)\;H_2S + x\,S^0} \qquad \textbf{(2.1)}$$

$$\mathbf{FeS_{1-x} + 2(1-x)\,H^+ \rightarrow Fe^{2+} + (1-x)\,H_2S} \qquad \textbf{(2.2)}$$

The generated H_2S can precipitate divalent metals (Me^{2+}, e.g. Hg^{2+}, Cu^{2+}, Pb^{2+}, Cd^{2+}) from aqueous solutions by forming metal sulfides (Ozverdi & Erdem, 2006), as described by Eq. 2.3.

$$\mathbf{H_2S + Me^{2+} \rightarrow MeS + 2H^+} \qquad \textbf{(2.3)}$$

When pH is ≥3, the dissolution of iron sulfides in metal wastewater would be promoted due to much lower solubility products (Ksp) of metal sulfides than iron sulfides. Consequently, dissolved S^{2-} precipitates divalent metals in solutions as metal sulfides as described by Eq. 2.4 (Yang et al., 2014a). Metal removal from wastewater by iron sulfides via precipitation will be discussed in Section 2.3.1.1.

$$\mathbf{Me^{2+} + FeS \rightarrow MeS + Fe^{2+}} \qquad \textbf{(2.4)}$$

The dissolved Fe^{2+} from iron sulfides can act as a catalyst in electro-Fenton degradation process for degrading organic pollutants in wastewater, such as chlorinated organic pollutants, benzene, and polycyclic aromatic hydrocarbons (PAHs), which will be discussed in Section 2.3.2. Sulfide (S^{2-}) in iron sulfides can donor electrons for sulfur oxidizing bacteria like

autotrophic denitrifiers in iron sulfide based autotrophic denitrification processes to remove NO_3^- from wastewater, which is discussed in Section 2.3.3 (Bosch et al., 2012; Jørgensen et al., 2009; Pu et al., 2014; Torrentó et al., 2010; Torrentó et al., 2011).

2.3.2 Oxidation of iron sulfides in aqueous solutions

Oxygen and Fe^{3+} are two important oxidants for iron sulfide aqueous oxidation, and Fe^{3+} has been confirmed to be a more aggressive and reactive oxidant than O_2 for iron sulfides at all pH values (Chandra & Gerson, 2010). Janzen et al. (2000) compared the mean aqueous oxidation rate of pyrrhotite by Fe^{3+} and O_2. It was $4\times10^{-9} \pm 6\times10^{-10}$ mol· m^{-2} ·s^{-1} by O_2, and $3.5\times10^{-8} \pm 1.5\times10^{-9}$ mol· m^{-2} ·s^{-1} by Fe^{3+} at an initial Fe concentration of 2×10^{-4} mol· L^{-1} and a pH of 2.75. When O_2 is the primary oxidant, the overall oxidation of iron sulfides is generally described by Eqs. 2. 5-7 (Belzile et al., 2004; Chandra & Gerson, 2010).

$$\mathbf{FeS_2 + \frac{7}{2}O_2 + H_2O \rightarrow Fe^{2+} + 2SO_4^{2-} + 2H^+} \quad \textbf{(2.5)}$$

$$\mathbf{Fe_{1-x}S + \left(2 - \frac{1}{2}x\right)O_2 + xH_2O \rightarrow (1-x)Fe^{2+} + SO_4^{2-} + 2x\,H^+} \quad \textbf{(2.6)}$$

$$\mathbf{FeS_{1-x} + \frac{7}{2}(1-x)O_2 + \frac{1-x}{2}H_2O \rightarrow \frac{1-x}{2}Fe^{2+} + (1-x)SO_4^{2-} + (1-x)\,H^+} \quad \textbf{(2.7)}$$

Fe^{2+} resulting from the oxidation of iron sulfides is further oxidized to Fe^{3+} as described in Eq. 2.8.

$$\mathbf{Fe^{2+} + \frac{1}{4}O_2 + H^+ \rightarrow Fe^{3+} + \frac{1}{2}H_2O} \quad \textbf{(2.8)}$$

The produced Fe^{3+} can in turn oxidize iron sulfides more aggressively in Eqs. 2. (9-11).

$$\mathbf{FeS_2 + 14\,Fe^{3+} + 8\,H_2O \rightarrow 15\,Fe^{2+} + 2SO_4^{2-} + 16\,H^+} \quad \textbf{(2.9)}$$

$$\mathbf{Fe_{1-x}S + (8-2x)\,Fe^{3+} + 4\,H_2O \rightarrow (9-3x)\,Fe^{2+} + SO_4^{2-} + 8\,H^+} \quad \textbf{(2.10)}$$

$$\mathbf{FeS_{1-x} + (8-6x)Fe^{3+} + 4(1-x)H_2O \rightarrow (9-6x)Fe^{2+} + (1-x)SO_4^{2-} + 8(1-x)H^+} \quad \textbf{(2.11)}$$

The oxidation state of sulfur increases stepwise, resulting in production of sulfur/sulfoxy species such as elemental sulfur (S), polysulfides (S_n^{2-}), thiosulfate ($S_2O_3^{2-}$), and sulfate (SO_4^{2-}) (Chandra & Gerson, 2010; Rimstidt & Vaughan, 2003).

Oxidized products of iron include iron oxides (Fe_2O_3, Fe_3O_4), ferric oxyhydroxides ($Fe(OH)_3$), and ferric (hydroxy)sulfates ($Fe_{16}O_{16}(OH)_{12}(SO_4)_2$) (Chiriţă et al., 2008). The formation of oxidation/intermediate products of iron sulfides is not only influenced by iron sulfides' grain sizes, crystal structures, and SSA, but also by the type and concentration of oxidants, solution redox potentials (Eh), temperature, and solution pH (Chandra & Gerson, 2011; Nicholson & Scharer, 1994; Nicol et al., 2013; Rickard & Luther, 2007; Sun et al., 2015). Oxidation products like ferrous sulfate ($FeSO_4$), ferric sulfate ($Fe_2(SO_4)_3$), and $Fe(OH)(SO_4)\cdot xH_2O$ are formed during the oxidation of iron sulfides at temperatures lower than 600–650 ^oC (Hu et al., 2006; Steger, 1982). An increase in temperature improves oxidation kinetics, which follows the Arrhenius behaviour (i.e. the oxidation rate increases with the increasing temperature) (Belzile et al., 2004). Studies have shown that low pH of 0–2 would not significantly influence pyrite's oxidation kinetics (Chandra & Gerson, 2010; Garrels & Thompson, 1960). A remarkable transition of the main oxidation products occurs when the final pH is around 4: the products are ferric (hydroxy)sulfates when pH is below 4, and are ferric oxyhydroxides when pH is above 4 (Bonnissel-Gissinger et al., 2001; Todd et al., 2003a). The formed Fe-oxyhydroxides (i.e. goethite (a-FeOOH)) have a high SSA of 10−132 $m^2\cdot g^{-1}$ and have surface hydroxyl groups (−OH) as effective adsorption sites (Liu et al., 2014a). Fe-oxyhydroxides also have positive surface charges in most solutions as their point of zero charge (pH_{zpc}) is about 9 (Sahoo et al., 2013). Therefore, Fe-oxyhydroxides can adsorb negatively charged inorganic oxyanions in

wastewater, like arsenic (Section 2.4.1) and phosphate (Section 2.4.4.2) (Chen et al., 2014b; Li et al., 2014b).

2.4 Application of Iron Sulfides into Wastewater Treatment

2.4.1 Removal of inorganic pollutants

2.4.1.1 Removal of toxic metals and metalloid

Toxic metal/metalloid wastewaters generated from the rapid development of industrial activities such as metal plating, mining operations, tanneries, batteries, paper industries, etc., are an ecological and environmental concern. Commonly found highly toxic metals include lead (Pb), mercury (Hg), cadmium (Cd), hexavalent chromium (Cr), and arsenic (As) a metalloid which usually exists as its oxidized species-arsenite (As^{3+} as H_3AsO_3, $H_2AsO_3^-$, $HAsO_3^{2-}$) and arsenate (As^{5+} as H_3AsO_4, $H_2AsO_4^-$, $HAsO_4^{2-}$) (Bulut et al., 2013). These elements are the top five in the Priority List of Hazardous Substances in 2015 by the U.S. Agency for Toxic Substances and Disease Registry which excludes organic toxicants (ATSDR, 2015). There are various methods to remove these metals and metalloid from wastewater, such as chemical precipitation, ionic exchange, biological uptake, and electrochemical processes. Among these methods, chemical hydroxide precipitation is widely used, but a large volume of hazardous metal-rich sludge is generated and separation of the sludge from wastewater is difficult (Chen et al., 2014a). Ionic exchange and electro-chemical treatment have high initial capital investment costs and high operation costs, restricting their applications (Fu & Wang, 2011). Biological uptake is strongly affected by the properties of the wastewater to be treated (Tetsuro & Shuzo, 2012). Nowadays, many studies are focused on the development of new and efficient sorbents from cost-effective materials for removal of metals and metalloid.

Iron sulfides have been widely investigated in recent decades as low-cost and easily available sorbents for metals and metalloid from wastewater. The dominant mechanisms of metals and metalloid removal by iron sulfides can be classified into: adsorption (Borah & Senapati, 2006; Bostick & Fendorf, 2003; Jean & Bancroft, 1986), dissolution/ precipitation (Chen et al., 2013b; Jeong et al., 2007), and reduction (Kantar et al., 2015a; Lin & Huang, 2008; Lu et al., 2006). Table 2.2 summarizes the sorption efficiencies and dominant mechanisms of metals and metalloid removal from wastewater using iron sulfides.

Table 2.2: Efficiencies and main mechanisms of metal and metalloid removal by iron sulfides

Main Mechanism	Iron sulfides	SSA ($m^2 g^{-1}$)	Target elements	pH	Initial Concentrations ($mg L^{-1}$)	Removal capacities ($mg g^{-1}$)	References
Adsorption	Pyrite	0.42	Hg^{2+}	6.4	0.4-8	2	(Behra et al., 2001; Bower et al., 2008)
	Pyrite	0.42	Hg^{2+}	4.1	0.4-8	1.23	(Bower et al., 2008)
	Pyrite	0.42	Hg^{2+}	10.4	0.4-8	3.5	(Bower et al., 2008)
	Pyrite	n	Cd^{2+}	6	100	2.08	(Erdem & Ozverdi, 2006)
	Pyrrhotite	n	Hg^{2+}	4.0	1-200	80.9	(Brown et al., 1979)
	Synthetic mackinawite	284	Hg^{2+}	5.5-6.0	1003	88.25	(Jeong et al., 2007)
	Synthetic mackinawite	350	As^{3+}	7.2	2.24	9.75	(Wolthers et al., 2005b)
	Synthetic mackinawite	350	As^{5+}	7.4	2.24	32.25	
Precipitation	Synthetic pyrite	41	As^{3+}	7	0-18.73	17.32	(Bostick & Fendorf, 2003)
	Synthetic pyrite	n	As^{3+}	10	0.6-63.4	20.1	(Han et al., 2013)
	Synthetic pyrite	n	As^{5+}	9.0	0.5-53.4	12.9	
	Synthetic pyrrhotite	n	Cu^{2+}	5	100	84	(Chen et al., 2014a)
	Synthetic pyrrhotite	6.86-10	Pb^{2+}	5	100	73.68	(Yang et al., 2014a)
	Synthetic pyrrhotite	6.86-10	Cd	5	100	8.42	
Reduction	Pyrite	4.13	Cr^{6+}	5.5	10	0.62	(Liu et al., 2015)
	Pyrrhotite	n	Cr^{6+}	1-10	52	0.24	(Lu et al., 2006)
	Synthetic mackinawite	n	Cr^{6+}	5	5.2-312	240	(Mullet et al., 2004)

Adsorption

Since 1979, researchers have found iron sulfide minerals (pyrite and pyrrhotite) are excellent adsorbents for metals and metalloids. Divalent metals like Pb^{2+}, Zn^{2+}, Cd^{2+}, and Hg^{2+} can be adsorbed on iron sulfides by forming inner sphere ion–surface complexes (Brown et al., 1979; Jean & Bancroft, 1986; Watson et al., 1995); As^{3+} and As^{5+} adsorption on iron sulfides shows primary coordination to four oxygens (As-O) with further iron and sulfur shells under anaerobic conditions (Farquhar et al., 2002); arsenic can also be immobilized by bidentate-type edge-sharing and double-corner sharing surface complexes with Fe (oxyhydr)oxides, a product of iron sulfides oxidation (Bulut et al., 2013; Jeong et al., 2010b).

The adsorption capacity is determined by the availability and density of reactive sites (e.g., ≡S-H groups) on iron sulfides' surface (Jeong et al., 2007; Watson et al., 1995). Therefore, synthesized mackinawite which have a high SSA of 424 ± 130 $m^2 \cdot g^{-1}$ compared with natural pyrite (0.02–41 $m^2 \cdot g^{-1}$) is expected to be efficient in metal and metalloid removal (Table 2.2). The maximum adsorption capacity was higher (9.47 mg Cd^{2+}/g) for synthesized iron sulfides than pyrite (3.43 mg Cd^{2+}/g) (Erdem & Ozverdi, 2006). The same tendency was found for As adsorption on mackinawite and pyrite, with the adsorption capacities being 1.19 mg $As^{3+} \cdot g^{-1}$ and 1.39 mg $As^{5+} \cdot g^{-1}$ for mackinawite, and only 0.36 mg $As^{3+} \cdot g^{-1}$ and 0.43 mg $As^{5+} \cdot g^{-1}$ for pyrite, respectively, at an initial As concentration of 15 $mg \cdot L^{-1}$ (Farquhar et al., 2002). A faster and higher extent of As^{5+} removal than As^{3+} removal by both pyrite and mackinawite was found (Couture et al., 2013; Han et al., 2013; Wolthers et al., 2005b). Han et al. (2013) observed a complete As^{5+} removal within 30 min and 95% of As^{3+} removal after 180 min. The logarithm of the equilibrium constant (log Keq) which is the parameter to indicate the extent of the reaction was estimated to be 0.5 and 0.7 for As^{3+} and As^{5+} onto mackinawite, respectively (Couture et al., 2013).

The adsorption of metals on iron sulfides is a function of pH, temperature, adsorbent dosages, contact time, and initial metal/metalloid concentrations (Borah & Senapati, 2006; Erdem & Ozverdi, 2006; Ozverdi & Erdem, 2006). Among these factors, pH plays a crucial role. Too low pH leads to dissolution of pyrrhotite and mackinawite (as in Eqs. 2.1-2), and too high pH results in hydrolysis of metals impacting the adsorption mechanisms. At acidic pH of ≤ 3.5, surface complexes between Hg and pyritic sulfur like $\equiv S^{-}$-Hg-OH are formed on pyrite's surface; at pH > 3.5, Fe (hydr)oxides and surface complexes between Hg and both oxides and pyritic sulfur are formed (Behra et al., 2001; Bower et al., 2008). The sorption capacity is enhanced with the increase in pH (i.e. 4.1, 6.4, and 10.4) when pH is above pHzpc (i.e. 3.3) for pyrite (Table 2.2). Bower et al. (2008) observed the highest sorption capacity on pyrite with 3.5 mg $Hg^{2+}\cdot g^{-1}$ at a pH of 10.4, 2.0 mg $Hg^{2+}\cdot g^{-1}$ at a pH of 6.4, and 1.23 mg $Hg^{2+}\cdot g^{-1}$ at a pH of 4.1. The increasing sorption capacity with the studied pH is attributed to a deeper level of negatively charged iron sulfides' surface by increasing pH when pH was above pHzpc.

Precipitation

Removal of divalent metals by iron sulfides via precipitation of metal sulfides can mainly be achieved by two mechanisms as discussed in Section 2.2. Differences in Ksp values between iron sulfides and other metal drive the precipitation of these metals by iron sulfides. Ksp of HgS, CuS, PbS, CdS, and ZnS is 1.4×10^{-56}, 1.2×10^{-36}, 3.4×10^{-28}, 3.6×10^{-29}, and 1.2×10^{-23}, respectively, much lower than Ksp of FeS, 1.5×10^{-19} (Yang et al., 2014a). Precipitation of HgS is the primary mechanism of Hg^{2+} removal on mackinawite when the adsorption capacity of Hg^{2+} reaches saturation (Jeong et al., 2007; Jeong et al., 2010c). The maximum removal capacity was 1641 mg Hg(II)·g FeS^{-1}, and precipitation accounted for 77% of the total Hg removal (Liu et al., 2008). Divalent metals with lower Ksp of their metal sulfides have a higher priority to precipitate on iron sulfides' surface. For instance, Cu is easier to be removed by iron sulfides via the precipitation of CuS than Pb, Zn and Cd (Yang et al., 2014a).

At a high As^{3+} concentration of 37.5 mg·L^{-1} and under acidic conditions, As^{3+} is removed by reduction followed by precipitation of realgar (AsS) on the surface of iron sulfides (Gallegos et al., 2007). Besides precipitation as arsenic sulfides (e.g., realgar (AsS) and orpiment (As_2S_3)), another type of precipitation is by the formation of surface precipitates like arsenopyrite (FeAsS) by a substitution of As for S with the formation of As−Fe bonds for As removal (Bostick & Fendorf, 2003; Bulut et al., 2013; Couture et al., 2013; Gallegos et al., 2008; Gallegos et al., 2007; Liu et al., 2016; Renock et al., 2009). However, As^{3+} removal due to precipitation decreases with an increase in pH when it's above 6 as the solubilities of iron sulfides decrease, and a formation of adsorbed surface complexes would dominate, which has been discussed above.

Besides surface precipitation for metal removal, disproportionation may occur at highly reactive defect Fe or S surface sites on iron sulfides. The surface defect structures may promote metal removal by serving as centers for electron transfer via disproportionation, which results in the formation of various surface species on defect surfaces, such as Fe^{3+} sulfides and polysulfides (S_n^{2-}, n=2, 3, ……， 9) (Bostick & Fendorf, 2003). For example, besides precipitation of CdS, Cd sorption on pyrite involves surface reconstruction of FeS_2 and sulfur disproportionation during Cd sorption, which leads to the formation of elemental S and $Fe(OH)_3$ as in Eq. 2.12 (Bostick et al., 2000).

$$\mathbf{Cd^{2+} + FeS_2 + H_2O \rightarrow Fe(OH)_3 + CdS + S + H^+} \quad \textbf{(2.12)}$$

Reduction

Iron sulfides can reduce Cr^{6+} to less toxic Cr^{3+} species due to reduced iron and sulfur in their crystal structures (Boursiquot et al., 2002; Demoisson et al., 2007; Doyle et al., 2004; Lin & Huang, 2008; Lu et al., 2006; Patterson et al., 1997; Zouboulis et al., 1995). Iron sulfides have been explored as functional materials for permeable reactive barriers (PRBs) for remediation of

Cr-contaminated groundwater (Kantar et al., 2015b; Liu et al., 2015). Generally, Cr^{6+} reduction reaction by iron sulfides takes place in two distinct stages, each consisting of multiple steps. Iron sulfides are first dissolved in acidic solutions releasing Fe^{2+} and S_2^{2-} or S^{2-} ions, followed by the adsorption of Cr^{6+} as $Cr_2O_7^{2-}$ or CrO_4^{2-} onto the iron sulfides' surface. Then the adsorbed Cr^{6+} is reduced to Cr^{3+} by iron and sulfide species at the surface of iron sulfides. Finally Cr^{3+} precipitates mainly as Fe^{3+}-containing Cr^{3+}-hydroxide solid phases $(Cr_xFe_{1-x})(OH)_3$ and SO_4^{2-} species (Boursiquot et al., 2002; Doyle et al., 2004; Lin & Huang, 2008; Lu et al., 2006; Patterson et al., 1997; Zouboulis et al., 1995). More surface precipitates are formed on iron sulfides at higher Cr^{6+} concentrations, pH values, and dissolved oxygen (DO) concentrations, which inhibit Cr^{6+} removal by iron sulfides (Kantar et al., 2015b; Liu et al., 2015). A stronger passivation of precipitates is formed at higher pH values for Cr^{6+} reduction by mackinawite. Mullet et al. (2004) found a lower removal capacity at a pH of 5 (240 mg Cr^{6+} g^{-1} FeS_{1-x}) than at a pH of 7 (130 mg Cr^{6+} g^{-1} FeS_{1-x}). Therefore, a number of improvements in minimizing the formation of a passivating layer on iron sulfides' surface have been utilized to improve Cr^{6+} reduction efficiency, such as using natural and/or synthetic complexing ligands. The efficiencies of organic ligands are in the order of citrate ≥ tartrate ≈ oxalate > EDTA > salicylate on Cr^{6+} removal by pyrite (Kantar et al., 2015a).

2.4.2 Removal of radionuclides

Radioactive waste is generated in nuclear power plants and its environmental risks are caused by their high radioactivity and long half-lives, which are strongly governed by redox conditions and their solubility and complexation behaviors in aqueous systems. Iron sulfides can adsorb radionuclides and then reduce them to low solubility solids under reducing conditions. Lots of studies have identified reduction species of radioactive elements on pyrite and mackinawite's surface using the X-ray absorption spectroscopy techniques (including X-ray absorption near-edge spectroscopy-extended and X-ray absorption fine structure; XANES and EXAFS) to understand the binding mechanisms. Reviews of these studies would give an insight to the migration behaviour of radionuclides in aquifers in the presence of iron sulfides.

However, further studies such as flow-through reactors are necessary to examine the long-term stability and uptake capacity of radionuclides by iron sulfides as a function of pH, hydraulic retention time (HRT), and dissolved oxygen (DO) concentration. Iron sulfides serve as electron sources or O_2 scavengers upon O_2 intrusions (Bi & Hayes, 2014; Hyun et al., 2012). Consequently, a weathered layer on the pyrite's surface is formed prior to reactions, which significantly limit the amount of radionuclide sorbed (Scott et al., 2007). Given that iron sulfides in natural systems are more likely to have weathered surfaces, effective radionuclides remediation by weathered iron sulfides needs to be studied further.

Similar to Cr^{6+} removal by iron sulfides, reduction of radionuclides such as Uranium (U), Selenium (Se), Plutonium (Pu), Neptunium (Np), and Technetium (Tc) by iron sulfides is attributed to reduced Fe^{2+} and S^{2-} species in iron sulfides. The reduction species of radioactive nuclides are presented in Table 2.3. Redox-sensitive radionuclides Se^{4+} can be reduced to more electron-rich Se species like Se^0 and Se^{2+} by iron sulfides with a production of oxidized surface sulfur and iron species (Ma et al., 2014; Oasmaa et al., 2009). Kang et al. (2011) proposed a dissolved Fe^{2+} mediated electron transfer during reduction of aqueous Se^{4+} by pyrite, explaining an increased aqueous Se^{4+} reduction rate at high pH values as the decrease in dissolved Fe^{2+}. Different from other radionuclide reductions, due to the similarities between the ionic radius of selenide ($r^{VI}(Se^{2-})$ = 1.98 Å) and sulfide ($r^{VI}(S^{2-})$ = 1.84 Å) in the tetragonal crystal structures of FeS and FeSe, Se can substitute S^{2-} in iron sulfides to form discrete surface precipitates (e.g. FeSe or $FeSe_2$) by a dynamical dissolution−recrystallization process (Finck et al., 2012; Moyes et al., 2000; Oasmaa et al., 2009).

Unlike Se sorption on iron sulfides, reductions of U^{6+} by iron sulfides is governed by the surface S groups, yielding a mixture of U^{6+}/U^{4+} oxides(s) and polysulfides, and simultaneously releasing Fe^{2+} to solution by an exchange reaction with U^{6+} under anoxic conditions (Hua & Deng, 2008; Hyun et al., 2012; Livens et al., 2004; Moyes et al., 2000; Scott et al., 2007;

Veeramani et al., 2013; Wersin et al., 1994). An inertness of Fe^{2+} in iron sulfides for U^{6+} reduction was observed with no production of Fe^{3+}−bearing phases following U^{6+} reduction by iron sulfides. Moreover, the inhibition role of surface−associated Fe^{2+} was proposed for the reduction of UO_2^{2+} in the acidic solutions on pyrite due to the electrostatic attraction of Fe^{2+} and UO_2^{2+} cations at the iron sulfide/water interface (Yang et al., 2014b).

Table 2.3: Summary of radionuclide removal by iron sulfides

Radionuclides	Iron sulfides	Initial Concentrations (mg Ł$^{-1}$)	pH	Major products	References
Se	Pyrite	Se^{4+}, 484.8	6.5 and 8.5	Se^0 and FeSe or $FeSe_x$, Fe^{3+}-O and Fe^{3+}-S	(Breynaert et al., 2008)
	Pyrite	Se^{4+}, 0.079 and 0.39	n	Se^0	(Bruggeman et al., 2005)
	Pyrite	Se^{4+}/Se^{6+}, 789.6	8.0	Se^0	(Curti et al., 2013)
	Pyrite	Se^{4+}, 7896	4.5–6.6	Se^0	(Kang et al., 2011)
	Pyrite	Se^{4+}, 789.6	2-10	Se^0 and FeSe	(Naveau et al., 2007)
	Pyrrhotite	Se^{4+}, 31.58	4.0-6.5	Se^0	(Ma et al., 2014)
	Mackinawite	Se^{4+}, 78.2–717.7	4.0-6.6	Se^0, Fe_7Se_8 and FeSe	(Scheinost & Charlet, 2008)
	Mackinawite	Se^{2-}	6.89-7.1	Dissolution−recrystallization, FeSe	(Finck et al., 2012)
U	Pyrite	U^{6+}, 476.4	3, 4, 5.5	UO_{2+x} solid phase and oxidized sulfur	(Descostes et al., 2010)
	Pyrite	U^{6+}, 5.61	4.8	UO_2 and U^{5+} form solid phase	(Scott et al., 2007)
	Pyrite	U^{6+},4.76–47.60	3.0-9.5	U_3O_8/U_4O_9/U_3O_7/ UO_{2+x}	(Yang et al., 2014b)
	Mackinawite	U^{6+}, 11.90	5-11	U_3O_8/U_4O_9/UO_2 and polysulfides, and Fe^{2+}	(Hyun et al., 2012)
	Mackinawite	U^{6+}, 119.01–1190.1	6.7-7.0	U_3O_8 /UO_2	(Moyes et al., 2000)
	Mackinawite	U^{6+}, 238.02	7.0	Nanoparticulate UO_2, SO_4^{2-}, Fe^{2+}	(Veeramani et al., 2013)
Pu	Mackinawite	Pu^{5+}, 3.17 ± 0.24	8	PuO_2	(Kirsch et al., 2011)
Np	Mackinawite	Np^{5+}, 63.99–649.38	7-8	$Np(OH)_4$	(Moyes et al., 2002)
Tc	Mackinawite	Tc^{7+}		TcS_2	(Livens et al., 2004; Wharton et al., 2000)

2.4.3 Removal of organic pollutants

Organic contaminants in water bodies result from anthropogenic agricultural and industrialization activities. Some of them are poorly biodegradable and recalcitrant to conventional biological and physicochemical treatments. In the last decades, iron sulfide Fenton process (Eqs. 2.13–14) in which iron sulfides are used as heterogeneous catalysts have been explored to boost the degradation of recalcitrant organic pollutants including chlorinated organic compounds, benzene, and PAHs, which are summarized in Table 2.4. There are two main advantages of using iron sulfides as catalysts in Fenton process: i) a long durability compared with classic Fenton process. Fe^{3+} produced according to Eqs. 2.13-14 is reduced on the iron sulfides' surface (Eqs. 2.9–11) , generating Fe^{2+} back to the systems (Che et al., 2011), and ii) dissolved Fe^{2+} and H^{+} from iron sulfides leads to self-regulation of a conducive pH. Hence, the necessity to adjust pH to 3 in conventional Fenton process to maintain the catalytic efficiency of Fe^{2+} is avoided.

$$\mathbf{FeS_2/Fe_{1-x}S/FeS + H_2O_2 \rightarrow Fe^{3+} + H_2O + SO_4^{2-} + H^+} \quad \textbf{(2.13)}$$

$$\mathbf{Fe^{2+} + H_2O_2 \rightarrow Fe^{3+} + OH^- + OH\bullet} \quad \textbf{(2.14)}$$

Table 2.4: Literature summary of organic contaminant removal by iron sulfide Fenton process

Types of pollutants	Specific pollutants	Iron sulfides	Maximum degradation rate constant (h^{-1})	Major Reduction Products	References
Chlorinated organic compounds	Hexachloroethane	Mackinawite	2.5±1.0	Tetrachloroethylene	(Butler & Hayes, 1997);
	Tetrachloroethylene	Mackinawite	$(3.84\pm0.27) \times 10^{-3}$	Trichloroethylene, Acetylene	(Butler & Hayes, 1999; Jeong & Hayes, 2007);
	Carbon tetrachloride	Mackinawite	1.24±0.266	Chloroform	(Choi et al., 2009);
	1,1,1-trichloroethane	Mackinawite	0.0375±0.0018	1,1- dichloroethane and ethylene	
	p-chloroaniline	Pyrite	-	-	(Zhang et al., 2015)
	Trichloroethylen	Pyrite	$(1.49\pm 0.14) \times 10^{-3}$	-	(Che, Bae, & Lee, 2011; Hayes, 1999;
		Mackinawite-coated iron nanoparticles	1.76 ± 0.03	-	(Kim et al., 2013)
		Mackinawite	$2.48 \pm 0.16) \times 10^{-3}$	Acetylene	(Jeong & Hayes, 2007)
Benzene	Toluene	Pyrite	-	-	(Choi et al., 2014a)
	Nitrobenzene	Pyrite	1.506	Nitrosobenzene, phenylhydroxylamine and aniline	(Zhang et al., 2014)
Polycyclic aromatic hydrocarbons	Pyrene (cetylpyridinium chloride-aided)	Pyrite	1.164	CO_2	(Choi et al., 2014b)
Others	Diclofenac	Pyrite	-	Organic acids, HCl, and CO_2	(Bae et al., 2013)
	copper phthalocyanine	Pyrite nanoparticles	0.07	-	(Gil-Lozano et al., 2014)
	4-amino-3-hydroxy-2-p-tolylazo-naphthalene-1-sulfonic acid (AHPS)	Pyrite	-	-	(Labiadh et al., 2015)
	Tyrosol	Pyrite	15-24.6	Oxalic acid	(Ammar et al., 2015)
	Herbicide 2,4-dichlorophenoxyacetic acid (2,4-D)	Mackinawite	1.284	Acetic Acid, formic acid, and oxalic acid	(Chen et al., 2015)
	COD and colour (Landfill leachate)	Pyrrhotite	-	-	(Li et al., 2010)

Iron sulfides provide sufficient Fe^{2+} which can eliminate the need to add soluble iron salts for conventional Fenton process. In addition, a continuous in-situ electro–generation of H_2O_2 instead of adding commercial H_2O_2 can be achieved by bubbling with compressed air via reduction of dissolved oxygen in iron sulfide electron–Fenton process (Fig. 2.2) (Ammar et al., 2015; Labiadh et al., 2015). H_2O_2 produces hydroxyl radical (HO•) and other radicals such as hydroperoxyl radical (OOH•) and superoxide radical (O_2•−) (Bissey et al., 2006). HO• (2.76 V) is an acknowledged strong oxidant for successful degradation of environmental contaminants (Zhang et al., 2015), and OOH• (1.78 V) does not significantly affect the degradation kinetics of organic pollutants due to its low oxidation potential (Bae et al., 2013; Smith et al., 2004). Nevertheless, the role of O_2•− (-2.4 V), which is involved in producing more H_2O_2 and mediates the generation of OH^- by iron sulfides (Zhang et al., 2015), in degradation of organic contaminants is inconsistent. O_2•− was reported to play a key role in reducing organic contaminants such as carbon tetrachloride and p–chloroaniline (Che & Lee, 2011; Teel & Watts, 2002; Zhang et al., 2015). However, Bae et al. (2013) found that degradation kinetics of diclofenac in the pyrite Fenton process showed no differences with/without adding O_2•− scavenger (i.e. chloroform). Further research is necessary to find out how O_2•− works in the degradation of organic pollutants.

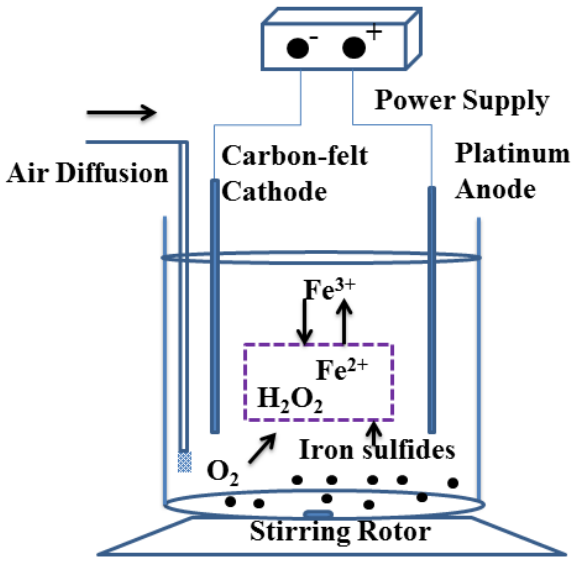

Figure 2.2: Scheme of the experimental set-up of iron sulfide electro-Fenton process (adapted from Oturan et al. (2008))

2.4.4 Removal of nutrients

2.4.4.1 Removal of nitrate

High concentrations of nitrate (NO_3^-) in water cause eutrophication which is one of the most widespread water environmental issues. Furthermore, NO_3^- in drinking water may be reduced to NO_2^- by gastrointestinal bacteria and then undergo nitrosation reactions to produce highly carcinogenic N-nitroso compounds (Shao et al., 2010). At present, the most common technology for NO_3^- removal from wastewater is biological heterotrophic denitrification, in which organic carbon is used as the electron donor for NO_3^- reduction (Li et al., 2008). However, if waters lack low biodegradable carbon substrates like groundwater and secondary treated municipal wastewater, the efficiency of heterotrophic denitrification is constrained. Thus, autotrophic denitrification using inorganic carbon (e.g. CO_2) provides an alternative for

NO_3^- removal. Autotrophic denitrification also has the advantages of lower operation costs, as well as less sludge production and carry-over of organic carbon to the effluent compared with heterotrophic denitrification. Sulfur-based autotrophic denitrification utilizes reduced sulfur compounds as electron donors, such as soluble thiosulfate ($S_2O_3^{2-}$), and insoluble elemental sulfur (S) and iron sulfides (Shao et al., 2010).

Iron sulfides have been found as efficient electron donors for sulfur oxidizing bacteria, such as *Acidithiobacillus Thiooxidans* and *Thiobacillus Denitrificans*, for autotrophic denitrification treating nitrate-contaminated wastewater as described by Eqs. 2. 15-16 (Bosch et al., 2012; Haaijer et al., 2007; Jørgensen et al., 2009; Li et al., 2013b; Pu et al., 2014; Schippers & Jørgensen, 2002; Torrentó et al., 2010; Torrentó et al., 2011). Furthermore, hydrolysis of dissolved S^{2-} generates OH^- which can buffer H^+ resulting from iron sulfides based autotrophic denitrification (Li et al., 2013b; Pu et al., 2014). Therefore, there is no need to add alkaline reagents like limestone to neutralize the produced acidity, which is inevitable in element-sulfur-based autotrophic denitrification.

However, autotrophic denitrification based on natural iron sulfide minerals is rarely applied in practice due to its low denitrification rate, which is much lower than that of heterotrophic denitrification with 2.65×10^6 mg NO_3^-–N kg_{vss}^{-1} d^{-1} (Koenig & Liu, 2001). The autotrophic denitrification rate was only 7.56 mg NO_3^-–N kg_{py}^{-1} d^{-1} in biofilters filled with natural pyrite particles (diameter, 50–100 μm) at a HRT of 11.6 h (Torrentó et al., 2010).

$$\mathbf{2FeS_2 + 6\,NO_3^- + 4\,H_2O \rightarrow 4\,SO_4^{2-} + 3\,N_2 + 2\,H^+ + 2\,Fe(OH)_3} \quad \textbf{(2.15)}$$

$$\mathbf{10\,FeS + 18\,NO_3^- + 16\,H_2O \rightarrow 10\,SO_4^{2-} + 9\,N_2 + 2H^+ + 10\,Fe(OH)_3} \quad \textbf{(2.16)}$$

2.4.4.2 Removal of phosphorus

Previous studies have reported that P can be removed by natural pyrrhotite via chemisorption according to Eq. 2.17, and the maximum adsorption capacity was 0.79–1.15 mg P $\cdot g^{-1}$ pyrrhotite at 11.3–29 °C (Li et al., 2013a). By calcining pyrite/ limonite ($FeO(OH)\cdot nH_2O$) and pyrite under an N_2 atmosphere at 600–650°C, the formed nanostructured pyrrhotite (NPyr) has a maximum P sorption capacity at 15–35 °C of 1.61–5.36 mg P$\cdot g^{-1}$ NPyr (Chen et al., 2016; Chen et al., 2014b). Baken et al. (2015) also found that phosphate can be removed by forming iron phosphate precipitates on iron sulfides' surface as described by Eq. 2.18.

$$\mathbf{pPO_4^{3-} + Fe_n(OH)_m \rightarrow Fe_n(OH)_m \cdot (PO_4)_p \downarrow} \quad \textbf{(2.17)}$$

$$\mathbf{Fe^{3+} + PO_4^{3-} \rightarrow FePO_4 \downarrow} \quad \textbf{(2.18)}$$

2.4.4.3 Simultaneous removal of nitrogen and phosphorus

In iron sulfide–based autotrophic denitrification processes (Section 2.4.4.1), autotrophic denitrifiers such as *Thiobacillus Denitrificans*, *Thiobacillus Thiooxidans,* and *Thiobacillus Ferrooxidans* have the ability to catalyze the oxidation of iron sulfides and formation of ferric iron hydroxides by increasing the kinetics of oxidation of Fe^{2+} to Fe^{3+} in solutions (Belzile et al., 2004; Bosch et al., 2012). Therefore, it is easy to hypothesize that iron sulfides could act as phosphorus scavenger via adsorption and precipitation on the surface of iron sulfides during iron sulfide-based autotrophic denitrification processes.

Liu et al. (2012) used biofilters added with pyrite: limestone to treat real secondary municipal effluent with concentration of NO_3^--N of 25.5 mg$\cdot L^{-1}$ and TP of 4.2 mg$\cdot L^{-1}$ at a HRT of 5 d, and effluent concentrations of N of 0.94 mg$\cdot L^{-1}$ and P of 0.04 mg$\cdot L^{-1}$ was achieved (Table 2.5). Li et al. (2016) proposed pyrrhotite autotrophic denitrification biofilter (PADB) technology for simultaneous N and P removal from municipal wastewater treatment plant secondary effluent.

Effluent N and P was 1.9 $mg \cdot L^{-1}$ and 0.3 $mg \cdot L^{-1}$ when treating real secondary municipal effluent with N of 21.1 $mg \cdot L^{-1}$ and P of 2.6 $mg \cdot L^{-1}$ at a HRT of 24 h by PADB technology. However, long HRTs of up to 24 h were required in natural iron sulfide biofilters, making it impractical to be applied in mainstream WWTPs. Thus, it's essential to solve this engineering issue by shortening HRTs.

Table 2.5: Nutrient removal by natural iron sulfide minerals-based autotrophic denitrification

Medium	Medium size (mm)	HRT (h)	N removal (%)	P removal (%)	References
Pyrite	0.05–0.1	11.6	100	–	(Torrentó et al., 2010)
Pyrite:Limestone (3-10:1, m/m)	<25	5 d	>90	100	(Liu et al., 2012)
Pyrrhotite	2–20	12–24	74–96	95–96	(Li et al., 2014a)
Pyrrhotite	2.36–5.12	24	91–95	87–95	(Li et al., 2016)

2.5 Summary

Pyrite (FeS_2), pyrrhotite ($Fe_{1-x}S$), and mackinawite (FeS_{1-x}) have been demonstrated as unique and promising materials due to its physicochemical properties. Fig. 2.3 summarizes the application of iron sulfides into the removal of inorganic toxic elements (As, Pb, Hg, Cd, and Cr), radionuclides (U and Se), organic contaminants (chlorinated organic pollutants, benzene, and polycyclic aromatic hydrocarbons), and nutrients (N and P) from wastewater and the dominant mechanisms involved in the processes. To increase their reactivity and efficiencies, natural nano-sized colloidal pyrite and synthesized NPyr with high SSA and porous structures have been investigated for metal removal from wastewater, which will be discussed in Chapter

3 and Chapters 4-5, respectively. By considering that NPyr has a higher SSA than natural iron sulfides, it shall be a more efficient electron donor for autotrophic denitrifiers. The PADB technology has been improved using NPyr as the biofilm substratum for autotrophic denitrifiers, which will be discussed in Chapter 7.

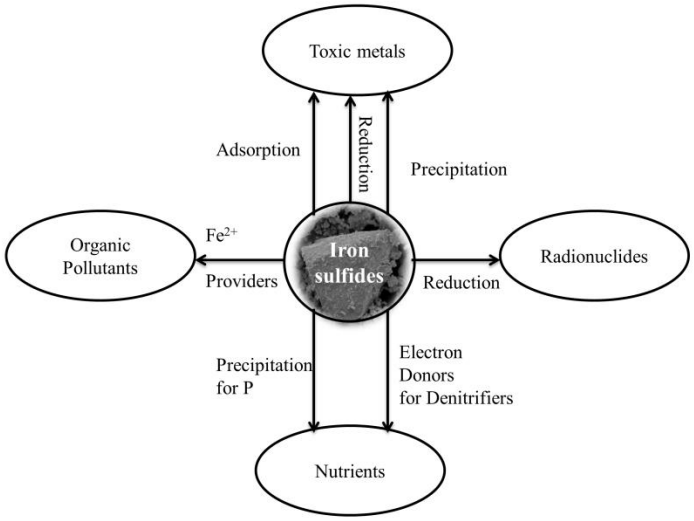

Figure 2.3: Schematic model of reaction mechanisms of iron sulfides with various environmental contaminants.

Chapter 3

Immobilization of Cu Under an Acid Leach of Colloidal Pyrite Waste Rocks

3.1 Overview

This Chapter presents the efficiency of nature colloidal pyrite waste rocks (CPWR) for removing low–concentration Cu (10 $mg \cdot L^{-1}$) under weakly acidic leach conditions (pH=5.0). A fixed–bed column was used to investigate the weathering and oxidation of CPWR and its role in immobilizing metals.

3.2 Introduction

The mixture of CPWR which are found dispersed in many igneous and metamorphic rocks and are highly concentrated in certain ore deposits, such as in the bottom sediment of Hercynian Carboniferous Huanglong group of the middle–lower Yangtze River metallogenic belt in Eastern China. The colloidal pyrite and siderite are always deposited together in CPWR, forming a unique deposition of paragenesis under a reducing environment (Kelly & Turneaure, 1970). At present, CPWR are generally considered as wastes and are disposed in mine wastes and mill tailings. Weathering of CPWR leads to AMD. One of the outstanding environmental issues in Europe is the release of excess metals from the continent around the Iberian Pyrite Belt into the Atlantic Ocean, which is mainly caused by oxidation of iron sulfides in the Iberian Pyrite Belt (Cerón et al., 2013; Sainz & Ruiz, 2006). The immobilization of toxic metals by CPWR was studied in this chapter. Copper (Cu) was chosen for the immobilization of toxic metals by CPWR because Cu containing minerals such as chalcopyrite ($CuFeS_2$), chalcocite (Cu_2S), covellite (CuS), and bornite (Cu_5FeS_4) frequently deposit along with pyrite (FeS_2) in ore deposits (Chandra et al., 2012; Equeenuddin, 2014; Malakooti et al., 2013; Yousefi et al., 2014). The co-occurrence of Cu-bearing minerals and iron sulfide minerals leads to a high concentration of Cu in AMD (Malakooti et al., 2013). According to the best of our knowledge, this study is a first remediation design to investigate the weathering and oxidation of CPWR, and the role of CPWR in immobilizing Cu under an acid leach by a fixed–bed column, and to explore whether it can be used as an economical material for Cu removal.

3.3 Experimental Section

3.3.1 Experimental materials

The CPWR used in the column experiment were collected from Xinqiao Mine of Tongling City in Anhui Province, China. It was finely crushed and sieved (0.45–0.90 mm) in a laboratory mill. The CPWR particles were soaked in 1% HCl for 12 h to remove any trace amounts of iron oxide films formed on its surface, then rinsed with deionized water until the pH of water was 7. The particles were dried in an O_2–free glovebox and stored in a vacuum desiccator until use.

Because Cu concentrations in actual AMD are usually in the range of 2–50 $mg{\cdot}L^{-1}$ (Motsi et al., 2009; Romero et al., 2011; Sahinkaya et al., 2011b), 10 $mg{\cdot}L^{-1}$ was selected as the influent Cu concentration value for the fixed-bed experiment. In order to prepare the influent solution, stock solution of 1000 $mg{\cdot}L^{-1}$ Cu^{2+} was prepared by dissolving $CuCl_2$ in distilled water. The influent Cu solution was prepared by diluting the stock solution to 10 $mg{\cdot}L^{-1}$ with tap water. The mine leachate usually has pH values of 2.1–6.6 (Grande et al., 2013). The pH value of the influent solution for the column was adjusted to 5.0 using 0.1 M NaOH and HCl solutions by considering two facts: (1) obvious competition between H^+ and Cu^{2+} for binding sites on CPWR sorbent should be avoided (Zhang, 2011); (2) Cu^{2+} would be the dominant species and Cu hydroxides were not expected to play a major role in solutions under this condition (Martínez & McBride, 1998).

3.3.2 Batch experiments

Batch experiments were performed to find the impacts of contact time and initial pH on Cu removal by CPWR. The experiment was conducted in 50 mL polypropylene centrifuge tubes in triplicate. Controls without CPWR or Cu were run to account for possible losses resulting from Cu sorption on tubes and any leaching of Cu from CPWR, respectively. The initial Cu

concentration was 10 mg·L^{-1} by diluting $CuCl_2$ stock solution with deionized water. Each tube contained 20 g·L^{-1} of CPWR particles with a diameter of 0.45–0.90 mm. HCl and NaOH solutions were used to adjust the initial pH of the solutions to 2–6. pH values below 6 were chosen to avoid precipitation of Cu (hydr)oxides. The tubes were placed on a rotating shaker with a rotation speed of 40 rpm to ensure complete mixing.

3.3.3 Column experiment

The CPWR column was made of a 50–cm–high transparent glass column with an internal diameter of 10 mm (Fig. 1.3). The column was packed with 50 g of CPWR particles to a depth of 22 cm, and the column packing density was 2.89 g CPWR per mL working volume. A 10 cm thick layer of crushed glass was placed at both ends so as to prevent the sorbent particles from flushing out of the column. The Cu solution was continuously pumped into the column from the bottom using a peristaltic pump (Lange BQ50–1J, China) at a flow rate of approximately 11.5 mL h^{-1}. The porosity (%) of the CPWR was measured to be 38.7% and the hydraulic retention time was calculated as 0.58 h in consideration of the filling volume of CPWR, the porosity of the CPWR, and the flow rate, according to Eq.3.1.

$$\mathbf{HRT} = \frac{\mathbf{V_1 n}}{\mathbf{Q}} \qquad \mathbf{(3.1)}$$

where: V_1 is the volume of the added medium in the column, mL; n is the porosity of the added medium; and Q represents the influent flow rate in mL·h^{-1}.

The breakthrough of the columns was defined as when the Cu^{2+} concentration in the effluent of Column B exceeded 0.5 mg·L^{-1}, which is the most strict discharge standard for Cu in wastewater in China (GB 8978-1996, China), indicating that sufficient sorption was no longer occurring. The trial was stopped at this point.

3.3.4 Analytical techniques

The column effluent solution was collected at regular time and immediately filtered through 0.45 μm filter paper. The concentrations of Cu and other toxic metals (i.e. Cd and Pb) in the filtrate were determined with an atomic absorption spectrophotometer (WYS2200, China). Cd and Pb, which are primary contaminants in drinking water regulated by the Environmental Protection Agency in U.S. (World Health Organization, 2005), were tested to know if there were any potentially–leachable trace metals during the process. SO_4^{2-} concentration in the filtered effluent was examined using ion chromatography (WY6100, China). Fe^{2+} concentration in the filtrate was determined by the Ferrozine method (Stookey, 1970). pH was monitored using a pH meter (pHS–3C, China). SSA of CPWR was measured using the BET–N_2 adsorption method (Quantachrome NOVA 3000e, USA).

After the breakthrough occurred in the CPWR column, the column was first rinsed with deionized water for 5 hours to remove free Cu^{2+} from the surface of CPWR particles. Then, the column was sealed and placed in a freezer until it was completely frozen. The glass column was gently hit by a hammer, and the glass was broken into pieces while the CPWR particles were intact. Finally, the particles were segmented into 11 sections from bottom to top along the column every 2 cm by a knife. The 11 samples were dried at 30 °C with nitrogen gas and then analysed by a number of techniques: X–ray diffraction (XRD) (Dandong Haoyuan DX–2700, China) for mineral compositions, X–ray fluorescence (XRF) (Shimadzu–1800, Japan) for the contents of Fe and Cu, and field emission scanning electron microscopy (FE–SEM) with energy dispersive X–ray (EDX) (Sirion–200, America) for morphology and mapping of different elements (i.e. O, S, Fe, Cu). A rapid oxidation status of the used CPWR samples collected at different depths of the column was indicated by the determination of free iron (refers to Fe in the form of iron oxides/hydroxides) which were extracted using the dithionite–citrate–bicarbonate method (expressed by the percentage of Fe^{3+} in the used CPWR) (Mehra &

Jackson, 1960). Along with this, the siderite ($FeCO_3$) content in CPWR samples was assessed by a determination of generated CO_2 after completely dissolving CPWR samples in aqua regia (MultiN/C2100, Germany). In addition, the species of Cu in each CPWR sample was analyzed by means of sequential extraction: the fractions of exchangeable Cu, Cu bound to carbonates, Cu bound to iron and manganese oxides, Cu bound to organic and sulfides, and residual Cu (Rapln F., 1988; Tessier et al., 1979).

3.4 Results and Discussion

3.4.1 Characterization of fresh CPWR

The original CPWR contained 48.05% Fe, 41.08% S, 0.57% Ca, 1.98% Mg, 1.56% Mn, 0.42% Cu, 0.29% Si, 0.25% Al, 0.18% Zn, and 0.01% As. The SSA of the CPWR was 0.63 $m^2 \cdot g^{-1}$. XRD analysis of the CPWR samples showed that it was mainly composed of colloidal pyrite and siderite (Fig. 3.1 a). The crystals of colloidal pyrite in CPWR were cubic and their grain sizes were from nanometer to submicron, which were much smaller than that of normal pyrite which has micrometer crystal sizes (Fig. 3-1 b). $FeCO_3$ content was estimated to be 22.75% in the fresh CPWR samples. Siderite had micron rhombohedral morphology in the CPWR (Fig. 3.1 c). Therefore, it is reasonable to hypothesize that the dissolution and oxidation of siderite would likely occur after colloidal pyrite which had much smaller nanometer–sized crystals.

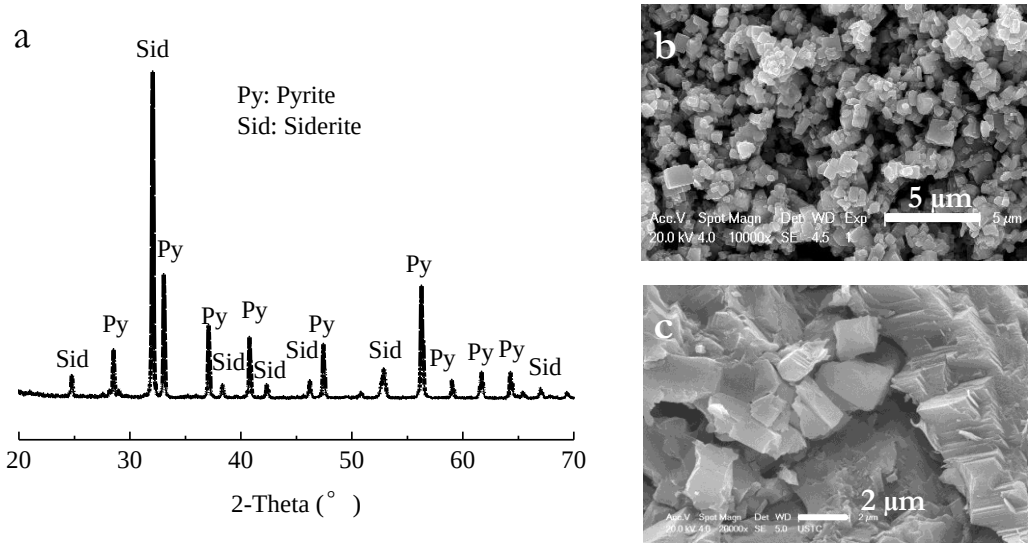

Figure 3.1: XRD pattern and SEM micrographs of the fresh CPWR

(a: XRD pattern; b: morphological image of pyrite in the CPWR; c: morphological image of siderite in the CPWR)

3.4.2 Contact time and pH on the removal of Cu by CPWR

Fig. 3.2 shows that Cu removal increases with contact time and then remains almost constant from 84 h at different initial pH values of 2, 3, 4, 5, and 6. Fig. 3.2a shows that there was no obvious pH dependence of Cu removal by CPWR. Considering that the mine leachate usually has pH values of 2.1–6.6, a pH of 5 was chosen as a representative for acid leachate to avoid obvious competition between H^+ and Cu^{2+} for binding sites on CPWR sorbent.

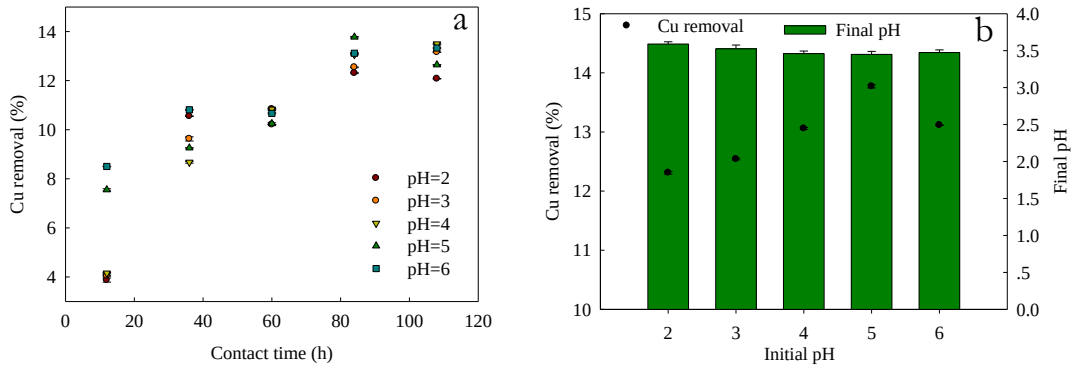

Figure 3.2: Effect of contact time (a) and initial pH (b) on Cu removal by CPWR (in Fig. 3.2 b, the contact time = 84 h).

3.4.3 Release of SO_4^{2-} and Fe^{2+}, and Cu removal

Dissolved oxygen (DO) in influent solution was critical to sustain the oxidation of pyrite and siderite in CPWR during the whole column experiment. In this study, SO_4^{2-} in the effluent only came from the oxidization of S^{2-} species in colloidal pyrite (FeS_2) in the CPWR described by Eq. 2.5, which has been reported in the previous studies (Donato et al., 1993; Shokri et al., 2013). It was increased initially indicating the oxidation of colloidal pyrite immediately occurred at the beginning of the column trial due to its high chemical reactivity resulting from its nanometer effect. Then SO_4^{2-} concentration leveled off at ca. 0.30 mmol·L^{-1}, which was below the maximum level of 250 mg·L^{-1} in drinking water set by Environmental Protection Agency U.S. when the throughput volume was from 2250 to 4726 bed volumes (BV) (Fig. 3.3a).

Effluent Fe^{2+} was in the range of 0.20–0.45 mmol·L^{-1} until the breakthrough occurred (Fig. 3.2b). If the released Fe^{2+} was only from the oxidation of the colloidal pyrite described by Eq. 3-1, it was supposed to be only 0.15 mmol·L^{-1}. The extra Fe^{2+} (the gap between 0.20–0.45 mmol·$L^{-1}$and 0.15 mmol·L^{-1}; ca. 0.05–0.30 mmol·L^{-1}) in the effluent was attributed to the

dissolution of siderite in the CPWR, which was initiated by the produced proton and generated CO_2 (described by Eq. 3.2). The percentage of Fe^{2+} in effluent resulting from the oxidation of colloidal pyrite was calculated to be 46.1% according to produced SO_4^{2-} in the effluent, and that resulting from the dissolution of siderite in CPWR was estimated to be 53.9%. The dissolution of CO_2 resulting from the dissolution of siderite buffered the solution and kept the pH values fluctuating around 4.5 (data not shown) during the simultaneous oxidization and dissolution processes of colloidal pyrite and siderite in the CPWR column. Under pH values of around 4.5, Fe^{2+} was easily oxidized to Fe^{3+} by DO in the influent solution (described by Eq. 3.3); the formed Fe^{3+} can act as an even more aggressive and effective oxidant than O_2 for pyrite oxidation (Moses & Herman, 1991; Moses et al., 1987). Fe^{3+} was not stable and easily precipitated in the CPWR column as ferric (hydr)oxides (Eq. 3.4) which could play two roles. On the one hand, ferric hydroxides precipitated on the CPWR's surface and acted as promising adsorptive materials for removing Cu (Jeong et al., 2010a); On the other hand, precipitation of ferric (hydr)oxides on the surface of CPWR can retard oxygen transport through this film. Consequently, the film retarded further dissolution and oxidation of the CPWR and would reduce the generation and diffusion rates of Fe^{2+} and SO_4^{2-}. The same passivation by building up of oxidation products was acknowledged (Sahoo et al., 2013; Todd et al., 2003a). Fe^{2+} concentration in the effluent decreased and then reached 0 when the throughput volume was from 3500–4500 BV, indicating decreased and ceased oxidation and dissolution of colloidal pyrite and siderite in the CPWR. When the formed ferric (hydr)oxides on CPWR particles' surface also reached its saturate adsorption capacity, the CPWR lost its removal capacity for Cu^{2+} and the breakthrough occurred.

$$\mathbf{FeCO_3 + 2H^+ \rightarrow Fe^{2+} + CO_2 + H_2O} \qquad \textbf{(3.2)}$$

$$\mathbf{Fe^{2+} + \frac{1}{4}O_2 + H^+ \rightarrow Fe^{3+} + H_2O} \qquad \textbf{(3.3)}$$

$$\mathbf{Fe^{3+} + 3H_2O \rightarrow Fe(OH)_3 + 3H^+} \qquad \textbf{(3.4)}$$

Cu^{2+} concentrations in the effluent from the CPWR column as a function of the number of BV treated are presented in Fig. 3.3c. The breakthrough curve demonstrates an efficient elimination of low–concentration Cu by the CPWR. Cu breakthrough of the CPWR column occurred when the throughput volume was up to almost 4081 BV. When the sorption breakthrough occurred, the amount of metals removed from water by CPWR, q ($mg \cdot g^{-1}$ CPWR), was calculated as follows:

$$q = \frac{M \int (C_0 - C_t) dV_2}{X} \qquad (3.5)$$

where, M is the relative atomic mass for Cu; C_0 and C_t are the influent and effluent concentrations of Cu ($mmol \cdot L^{-1}$); V_2 is the cumulative volume of treated water (L); and X is the mass of sorbent packed in the column (g).

Because of the much lower C_t before the column breakthrough than C_o, Eq. 3.5 can be simplified as Eq. 3.6.

$$q = \frac{MC_oV}{X} \qquad (3.6)$$

The Cu breakthrough capacity was calculated to be about 14.0 $mg \cdot g^{-1}$ CPWR according to Eq. 3.6. The result shows that the natural CPWR as a filling material had a high adsorption capacity for Cu even in comparison with other modified adsorbents. For example, the breakthrough capacity of manganese oxide coated zeolite was 8.32 mg $Cu \cdot g^{-1}$ (Han et al., 2006) and was 14.92 mg $Cu \cdot g^{-1}$ for chitosan immobilized on bentonite (Futalan et al., 2011) in fixed–bed columns under optimum operation conditions. Furthermore, the concentrations of other toxic metals (Cd and Pb) were all below detection limits (data not shown), suggesting that there was little leaching of trace metals from CPWR column.

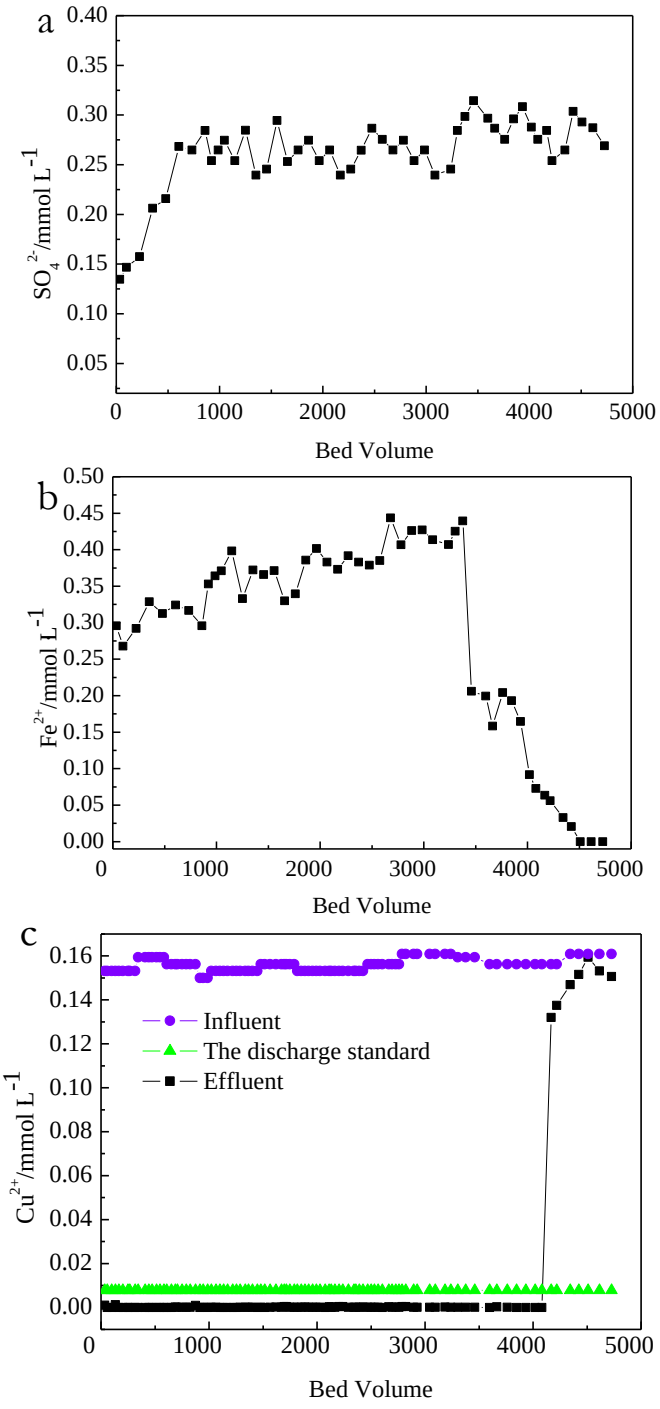

Figure 3.3: Development of SO_4^{2-} (a), Fe^{2+} (b), and Cu^{2+} (c) concentrations in the effluent of CPWR column

However, lower Cu removal efficiencies (13%) and removal capacities (0.050 mg/g CPWR) were obtained in the batch experiments than in the column study. The big difference between the batch and column studies is hard to fully understand. This phenomenon could be explained by the different final pH values in the solutions of batch and column studies. Previous studies have found that the main oxidation products of pyrite vary when the pH is around 4. The main oxidation product of pyrite is ferric (hydroxy)sulfate when pH is below 4, and it is ferric oxyhydroxide at higher pH (Todd et al., 2003b). In the batch experiments, a high degree of colloidal pyrite oxidation in CPWR occurred due to both dissolved O_2 in aqueous solutions and O_2 diffused from the atmosphere, leading to a final pH of around 3.5 (Fig. 1b). Therefore, insignificant amounts of ferric (hydr)oxides were formed. However, the oxidation of colloidal pyrite was limited in the column experiment, as the only source of O_2 was from the dissolved O_2 in the influent, resulting in a final pH of around 4.5. Consequently, the oxidized Fe^{3+} was rapidly hydrolyzed as ferric (hydr)oxides. Ferric (hydr)oxides can act as an adsorbent for Cu removal, so a higher amount of ferric (hydr)oxides in the column trial led to a higher Cu removal by CPWR. Nonetheless, further research is needed to confirm this explanation and elucidate the different processes in Cu removal by CPWR in the batch and column experiments.

3.4.4 Content and speciation of solid–phase Cu in the used CPWR

The total Cu and Fe contents in the CPWR particles sampled at different column heights after the breakthrough occurred are shown in Fig. 3.4a. After the breakthrough, Cu content increased with the column height; it was approximately 0.4% at the bottom of the column, while it was nearly 1.5% at the top. Meanwhile, Fe content in the used CPWR particles decreased from the top to the bottom column and was in the range from 42.43% to 47.8%. The reduced Fe was due to the release of Fe (in the range of 0.25-5.62%) into the solution during the oxidation of colloidal pyrite and dissolution of siderite in the CPWR.

Chemical sequential extraction was carried out to determine the solid–phase Cu species in the used CPWR samples. The fractions of the five different Cu species are shown in Fig. 3.4 b. The percentage of exchangeable Cu (S1), Cu bound to carbonates (S2), and Cu bound to sulfides (S4) were found to account for much less percentages than Cu bound to iron and manganese oxides (S3) and residual Cu (S5) in the CPWR samples. The low exchangeable Cu shows that Cu removal by surface complexation and ion exchange was negligible. Surface groups, such as surface Fe–hydroxyl groups (≡Fe–OH) and sulfhydryl functional groups (≡S–H) on the CPWR particles, which are generally considered as potential adsorption sites (Jeong et al., 2010c), were insignificant for Cu removal in this study. Moreover, the low percentages of Cu bound to carbonates and sulfides excluded the possibility of surface precipitation of $CuCO_3$ or CuS even though they have low solubility products. Fig. 3.4 b also shows that 35–46% Cu was present in the form of residual Cu (S5) which indicates that Cu existed within primary and secondary minerals' crystal structure (Tessier et al., 1979). 45–52% of Cu bound to iron and manganese oxides (S3) indicates that Fe (hydr)oxides formed by the oxidation of colloidal pyrite and dissolution of siderite in the CPWR served as major adsorbents for Cu^{2+} removal. To verify this, the contents of free iron (percentages of Fe^{3+}) in the used CPWR particles along the column height after the Cu breakthrough were measured.

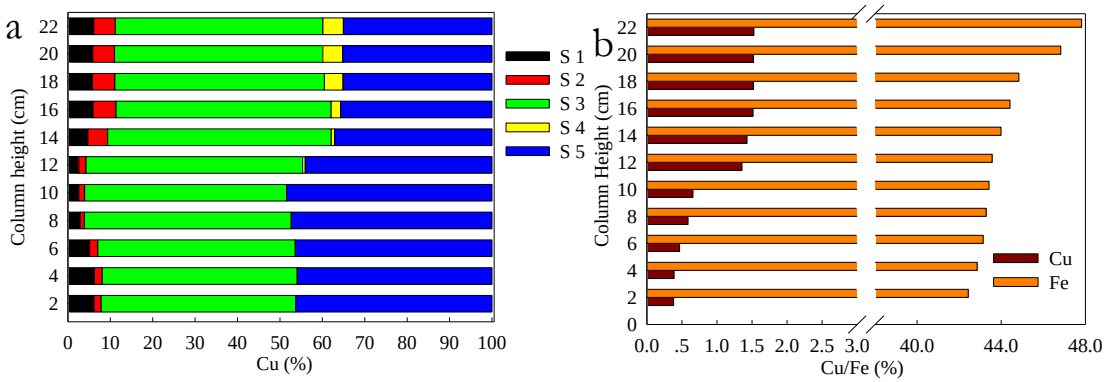

Figure 3.4: Variation of Cu and Fe contents, and the result of the Cu sequential extraction along the column height

(S1: exchangeable Cu; S2: Cu bound to carbonates; S3: Cu bound to iron and manganese oxides; S4: Cu bound to sulfides; S5: residual Cu)

3.4.5 Dissolution and oxidation of the used CPWR

Fig. 3.5 shows the contents of $FeCO_3$ and Fe^{3+} in the used CPWR particles along the column height when the breakthrough occurred. Siderite content in the used CPWR was less than that in fresh CPWR due to its dissolution in weakly acidic Cu solution. The amount of siderite dissolved during the study decreased with the increase in the column height and was 5.05% and 0.5% in the bottom and top of the CPWR column, respectively. The more dissolved siderite resulted in more production of CO_2 whose buffer capacity led to the higher oxidation rate of CPWR. A similar observation has been noted by Caldeira et al. (2010). The colour of the CPWR located in the top of the column turned from black into orange after the column was operated for two weeks. This was the obvious indication of the formation of Fe (hydr)oxides. The content of Fe^{3+} indicates that the free iron in CPWR increased with the column height, suggesting more Fe (hydr)oxides accumulated on the CPWR in the top of the column. More Fe (hydr)oxides formed in the top of the column can be explained by the rate of hydrolytic precipitation of Fe^{3+} (Eq. 3-4) which was slower than the flow rate, thus more Fe^{3+} was transported from bottom to top with the up–flow Cu wastewater under weakly acidic

condition. The amorphous Fe (hydr)oxides can effectively adsorb Cu due to their high SSA (Raven et al., 1998; Wilkie & Hering, 1996), explaining more Cu was immobilized on the top.

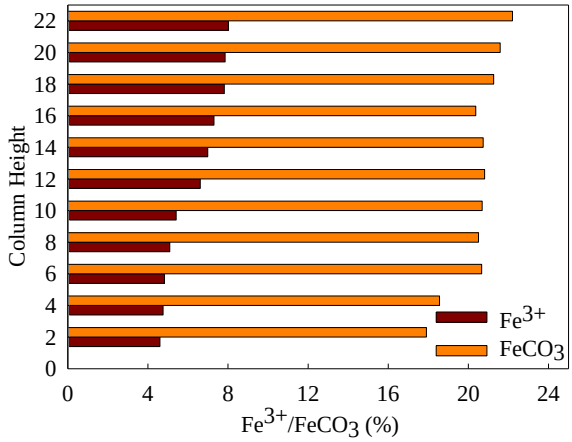

Figure 3.5: Variations of the Fe^{3+} and siderite contents in the CPWR with column height

Fig. 3.6 shows SEM micrograph and corresponding EDX mapping for elements of O, S, Fe, and Cu on the used CPWR particles collected from the top column after Cu breakthrough occurred. The CPWR's surface and cracks were covered with an accumulation of tremella–like substances which were probably ferric (hydr)oxides loosely nested on the CPWR particles' surface, drastically increasing the SSA and adsorption sites, and therefore enhancing adsorption capacity (Guo et al., 2013). Iron was evenly distributed on the surface of CPWR particles according to the Fe–EDX map (Fig. 3.6e). Combining O–EDX (Fig. 3.6c) with S–EDX (Fig. 3.6d), O–concentrated areas were found to be vacancies of S, indicating that the colloidal pyrite and the siderite in CPWR existed at two independent phases and were not structurally related to each other. In addition, the O–EDX map indicates oxidant attacks on CPWR surfaces related to the grain defects, cleavages and fractures, which were significant for Cu adsorption. As to Cu–EDX map, Cu was homogeneously distributed in the inner edge and more concentrated areas were found at the edges of CPWR particles, in agreement with the distribution of iron hydroxides. When CPWR's surface was completely overlaid by iron

(hydr)oxide coatings, leading to the termination of solution–phase dissolution and oxidation of CPWR, CPWR lost its capacity for Cu removal.

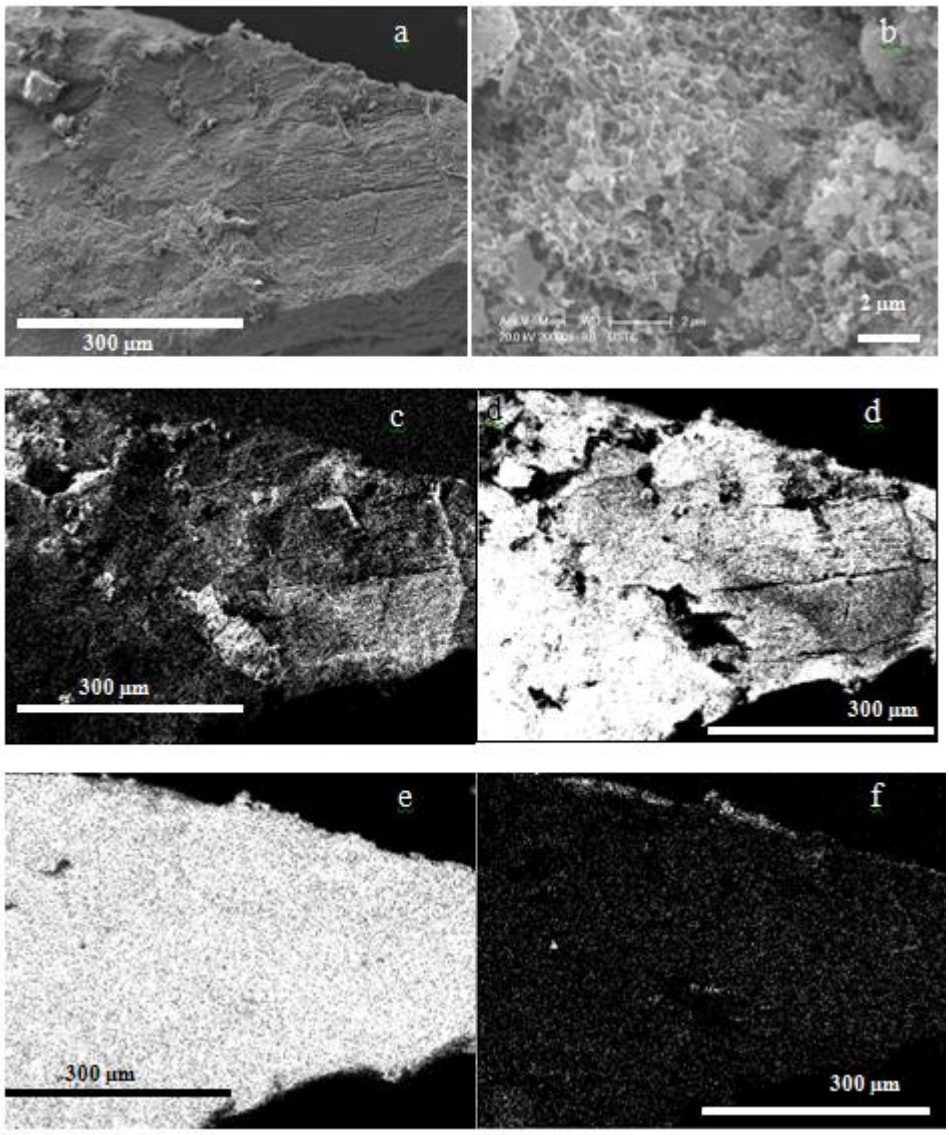

Figure 3.6: SEM micrographs (a and b) and SEM–energy dispersive X–ray (EDX) maps of oxygen (c), sulfur (d), iron (e), and copper (f) for the used CPWR particles after Cu breakthrough

A schematic diagram illustrating the proposed model for Cu removal by CPWR in weakly acidic solution is shown in Fig. 3.7. This process consists of three main steps. In the first step, the oxidation of pyrite by O_2 releases an electron into the solid from anodic site to cathodic site and then to the solution, and one or two hydrogen ions to the solution, resulting from the oxygen atom of a water molecule interacts with a sulfur atom to create a sulfoxy species (Eq. 2.5). The second step is the dissolution of siderite which is driven by the generated hydrogen ions, the produced CO_2 has the buffering effect and increases the oxidation rate of Fe^{2+} to the Fe^{3+} and ferric (hydr)oxides (Eqs. 3.3 and 3.4). In the third step, the formed ferric (hydr)oxides act as adsorbent for Cu.

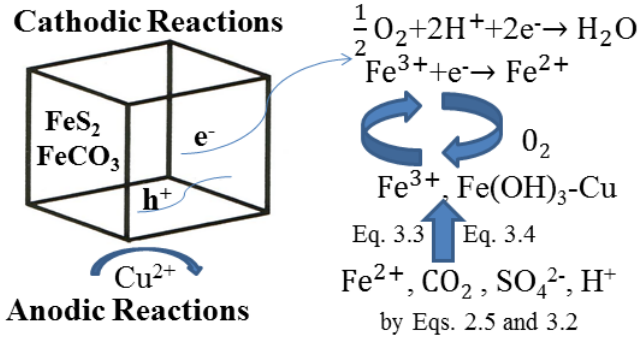

Figure 3.7: Schematic representation of the mechanism of Cu removal by CPWR.

3.5 Summary

This study shows that the natural CPWR were efficient in the removal of Cu from low–concentration (10 mg·L^{-1}) Cu solution. The breakthrough capacity was 14.0 mg Cu·g^{-1} CPWR. Sequential extraction of Cu, analysis of free Fe, and SEM–EDX analysis indicate that Cu^{2+} was removed from the aqueous solution due to the adsorption of Cu on iron hydroxides formed via the dissolution and oxidation of the CPWR. In order to increase the removal capacity for Cu, NPyr was developed. The metal removal efficiencies of NPyr were invesigated in Chapter 4 with both single metal and multi–metal solutions by fixed–bed sorption columns.

Chapter 4

Removal and Recovery of Cu and Pb from Single and Cu–Pb–Cd–Zn Multi-metal Solutions by Nanostructured Pyrrhotite

4.1 Overview

This Chapter presents the efficiency of synthesized nanostructured pyrrhotite (NPyr) for removal and recovery of Cu, Pb, Cd, and Zn from single and multi–metal aqueous solutions.

4.2 Introduction

Currently, the US Environmental Protection Agency regulates eight metals as primary contaminants in drinking water, including divalent heavy metals Cu, Pb, and Cd (EPA, 2016), which are widely found in e–waste and other sources. Unregulated heavy metals like Zn, might be monitored in the future due to their comparable detrimental health effects (WHO, 2005). Divalent toxic metals always co–exist in wastewaters like acid mine drainage (AMD), which have a tendency to interact with each other (primary cations) in the removal of metals from wastewater, particularly when using the sorption process. This has emphasized the importance of understanding the mechanisms involved in metal removal from wastewater, and the need for studying the effects of the competitive ions on the removal efficiency. To date, very few multi–metal sorption systems have been investigated; for instance, the removal of Pb, Cd, Cu, and Zn from Cu–Pb–Cd–Zn solution by hematite nanoparticles, montmorillonitic and calcareous clays (Sdiri et al., 2011; Shipley et al., 2013), the removal of Pb, Cd, and Cr from Pb–Cd–Cr solution by crab shell (Kim, 2003), and the removal of Cu and Pb from Cu–Pb–Cd solution by magnetic Ni/α–$Ni(OH)_2$ (Cao et al., 2013). Most of these multi–metal sorption studies were conducted in batch experiments rather than continuous–flow column systems which are much closer to the practical application. Besides, a growing interest in the reuse, recovery, and recycle of materials has posed a challenge for these methods which only target removal of metals rather than recovery.

In this research, the synthesized nanostructured pyrrhotite (NPyr), composed of nanocrystalline grains with porous structures, was used as the sorbent for Cu, Pb, Cd, and Zn

removal and recovery from both single metal and multi–metal solutions by fixed–bed sorption columns. The sorption capacities and the sorption mechanisms between the NPyr and the metals were investigated.

4.3 Materials and Methods

4.3.1 Materials

Pyrite minerals used in this study were collected from Xinqiao Mine of Tongling City in Anhui Province, China. After collection, they were finely crushed and sieved to 0.45–0.90 mm using a laboratory mill. The preparation of NPyr sorbents followed the method as follows: a certain amount of pyrite was calcined in a N_2 atmosphere at the temperature of 600 °C for 1 h (Shi et al., 2010). The obtained NPyr particles were then stored in a vacuum dessicator until use.

The influent concentrations of metals (Cu, Pb, Cd, and Zn) were 100 $mg \cdot L^{-1}$ in each single metal solution and were 30 $mg \cdot L^{-1}$ in the multi–metal solution containing Cu, Pb, Cd and Zn. The influent solutions were prepared by dissolving chloride salts of Cu, Pb, Cd, and Zn in tap water. All the chemicals used were of analytical grade. The pH values of the influent solutions were adjusted to 5 using 1 M of HCl solution to avoid the hydrolysis of the metals.

4.3.2 Column experiments

Sorption of Cu, Pb, Cd, and Zn on NPyr particles from the single metal solutions was carried out using four fixed–bed columns (i.e., single–metal sorption system: the Cu column, the Pb column, the Cd column, and the Zn column). Sorption of Cu, Pb, Cd, and Zn on NPyr particles from the Cu–Pb–Cd–Zn multi–metal solution was carried out with the fifth fixed–bed column (i.e., multi–metal sorption system, the Cu–Pb–Cd–Zn column). The five bench–scale columns were made of 50–cm–high transparent glass columns, with an internal diameter

of 10 mm. Each column was packed to a depth of 32 cm with a column packing density of 1.99 g NPyr·mL^{-1} working volume. The porosity (%) of the NPyr was measured to be 60%. A 10 cm thick layer of crushed glass was placed at either end of the column so as to prevent the sorbent particles from flushing out.

Each column was firstly washed with 1% HCl solution for 48 h to remove any trace amounts of carbonate and iron oxides films formed on the surface of NPyr particles. It was then rinsed with tap water until the pH of the leachate was close to 7. Then, the influent solutions were continuously pumped to each column from the bottom using peristaltic pumps (BQ50–1J, Lange, China) at a flow rate of 21 mL·h^{-1}. The hydraulic retention time was calculated as 0.58 h according to Eq. 3.1. The breakthrough of the single–metal columns occurred when the metal concentrations in the effluents were above the Chinese wastewater discharge standards (0.5 mg·L^{-1} for Cu, 1 mg·L^{-1} for Pb, 0.1 mg·L^{-1} for Cd, and 2 mg·L^{-1} for Zn). For research purposes, the breakthrough for the multi–metal column was defined as when the concentrations of the four metals in the effluent were all above their corresponding standards.

4.3.3 Analyses

Effluent solutions of the five fix–bed columns were collected and immediately filtered through 0.45 μm filter paper at regular time. pH values were monitored using a pH meter (pHS–3C, China). Concentrations of metals (including Cu, Pb, Cd, and Zn) in the filtrates were determined with an atomic absorption spectrophotometer (WYS2200, China) using the flame atomization technique. Specific surface area (SSA) of the natural pyrite and the NPyr were measured using the BET–N_2 adsorption method (Quantachrome NOVA 3000e, America).

After the breakthrough occurred, the columns were first rinsed with ultrapure water for 5 hours to remove non–sorbed metals from the NPyr particles' surface. Then, the columns were

sealed and placed in a freezer until they were completely frozen. The glass columns were gently hit with a hammer, and the glass was broken into pieces while the NPyr particles were intact. Finally, the particles were segmented into 16 sections from bottom to top along each column in every 2 cm by a knife. The 16 samples of each column were dried at 30 °C with N_2 and then analyzed using a number of techniques: X ray fluorescence (XRF) (Shimadzu–1800, Japan) for the contents of Fe and the corresponding metal(s) (i.e., Cu, Pb, Cd, and Zn), X–ray diffraction (XRD) (Dandong Haoyuan DX–2700, China) for mineral composition, field emission scanning electron microscopy (FE–SEM) (Sirion–200, America) coupled with energy dispersive X–ray spectroscopy (EDX) for morphology and elemental composition, and high resolution–transmission electron microscopy (HR–TEM) with energy dispersive X–ray (EDX), and (JEOL–2100F, Japan) for structure analysis and elemental composition. In addition, the species of sorbed metals in the used NPyr particles was analyzed by sequential extraction and different species of metals are introduced in Chapter 3.

4.4 Results and Discussion

4.4.1 Characterization of the natural pyrite and the NPyr

Chemical composition of the natural pyrite and the NPyr is presented in Table 4.1. Elemental analysis indicates a S: Fe atomic ratio of 2.07 (nearly 2) and 1.21 in the natural pyrite and the NPyr, respectively. The major source of impurity of the natural pyrite was due to quartz by considering the Si content (Table 4.1). XRD analysis of pyrite (data not shown) shows weak peaks of quartz, indicating the low content of quartz in the natural pyrite. Moreover, XRD characterization confirmed pyrrhotite was the primary product in the NPyr, and no other phases were detected.

SEM was utilized to examine the morphology and size distribution of the natural pyrite (Fig. 2.1, Chapter 2) and the NPyr (Fig. 1.1, Chapter 1). The SSA of the natural pyrite was 0.79 $m^2 \cdot g^-$

[1], and the NPyr had a nanometer–sized porous texture with a SSA of 6.86–10 $m^2 \cdot g^{-1}$ (Chen et al., 2014b).

Table 4.1: Chemical composition of the natural pyrite and the NPyr (wt %)

Sample	Fe	S	Si	Al	Cu	Ca	Mn	As	Mg
Pyrite	43.13	51.16	1.82	0.18	0.37	0.67	0.15	0.02	0.37
NPyr	56.02	38.73	1.72	0.22	0.47	0.55	0.08	0.00	0.20

4.4.2 Metal removal from the single and the multi–metal solutions

During the column experiments, the presence of DO in the influent wastewater can influence the removal of metals, oxidizing NPyr by formation of ferric (hydr)oxides on the surface of NPyr particles which are generally less reactive to metals than NPyr (as described in Eqs 2.6 and 2.8, Chapter 2) (Belzile et al., 2004). The effluent pH values of the five columns were a bit lower than the influent pH and fluctuated between 4.0 and 4.5, and this was caused by weak oxidation of NPyr by DO. Concentrations of SO_4^{2-} in the effluent formed due to the oxidation of S^{2-} by DO were as low as around 0.15 mM. The small pH change and low concentrations of SO_4^{2-} in each column suggest that oxidation of NPyr by DO should be insignificant under our experimental conditions.

Fig. 4.1 represents the ratio between the concentrations of metals in the column outlet to its concentrations in the column inlet (C/C_0) as a function of the volume of treated water (number of bed volumes, BV). The results show that NPyr had a high affinity to Cu, and the breakthrough occurred when the throughput volumes were up to 1540 BV and 2093 BV in the single Cu sorption system and the multi–metal sorption system, respectively. As for Pb, the removal efficiencies in the single Pb and the multi–metal sorption systems were quite different.

The Pb breakthrough volume was up to 1494 BV in the single Pb system and was only 698.7 BV in the multi–metal system. These findings show that the BV of Pb significantly decreased when the total metal loading in influent increased from 0.48 mM in the single Pb solution to 1.34 mM in the multi–metal solution (i.e., 0.14 mM for Pb, 0.47 mM for Cu, 0.46 mM for Zn, and 0.27 mM for Cd). A previous study has shown Cu was removed from wastewater by calcined colloidal pyrite due to the precipitation of covellite (CuS) on the calcined colloidal pyrite's surface(Chen et al., 2014a). As the same calcination product (monoclinic pyrrhotite) can be obtained from the calcination of pyrite and colloidal pyrite under their optimal thermal treatment conditions, it is reasonable to hypothesize that Cu, Pb, Cd, and Zn would also be removed by NPyr via precipitation of corresponding metal sulfides on NPyr's surface. Cu can easily precipitate as copper sulfide in comparison with Pb which precipitates as lead sulfide due to lower solubility products of CuS, and Cu would compete with Pb for limited sulfide (S^{2-}) dissolved from NPyr. In addition, it is noteworthy that the studied NPyr samples had lower removal efficiencies for Cd and Zn than Cu and Pb in both single and multi–metal sorption columns. The result of the Cu–Pb–Cd–Zn column shows that the metals were removed by NPyr with the sequence of Cu > Pb > Cd > Zn. This removal pattern is associated with the trend in solubility products (Ksp) of the respective metal sulfides, with Ksp of CuS, PbS, CdS, and ZnS equal to 1.2×10^{-36}, 3.4×10^{-28}, 3.6×10^{-29}, and 1.2×10^{-23}, respectively, which are much lower than that of FeS, 1.5×10^{-19} (Ni, 1998). The converse order of Pb and Cd would be explained by the precipitation of $PbSO_4$ (Ksp= 1.82×10^{-8}), which can also be found during Pb removal from wastewater by pyrite (Ozverdi & Erdem, 2006).

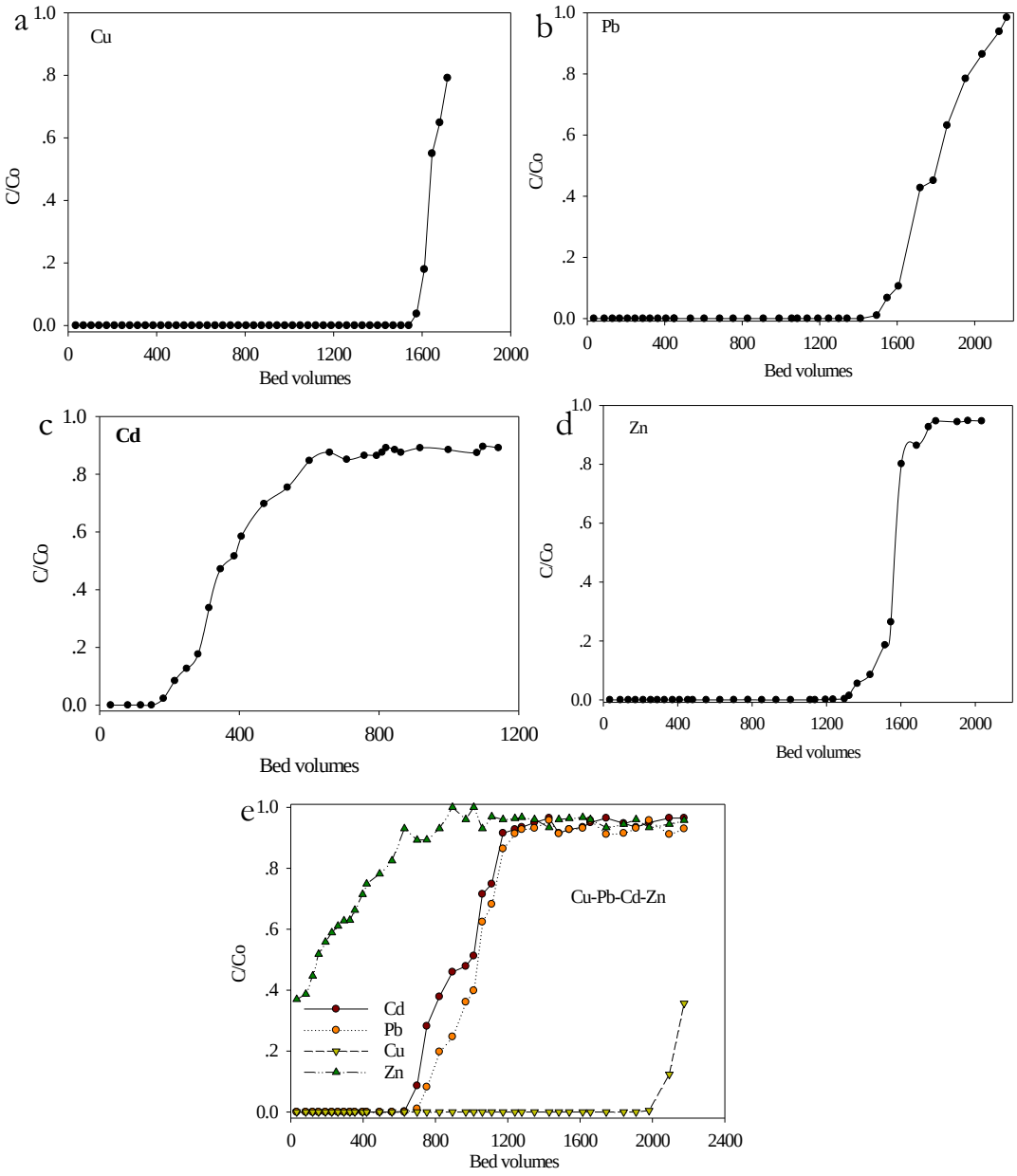

Figure 4.1: Breakthrough curves for Cu, Pb, Cd, and Zn in the single and multi–metal sorption columns (a: Cu column; b: Pb column; c: Cd column; d: Zn column; e: Cu–Pb–Cd–Zn column).

According to Eq. 3.6 (Chapter 3), the breakthrough capacities of the four single columns added with NPyr particles were calculated to be 77.42, 73.68, 8.42, and 58.74 $mg \cdot g^{-1}$ for Cu, Pb, Cd, and Zn, respectively. While in the Cu–Pb–Cd–Zn system, the breakthrough capacities of Cu, Pb, Cd, and Zn were 30.79, 10.86, 9.78, and 0 $mg \cdot g^{-1}$, respectively. The NPyr samples demonstrated larger removal capacities for Cu and Pb than Cd and Zn in both single–metal and multi–metal sorption systems. Moreover, the results indicate that the removed amounts of Cu, Pb, and Zn decreased and that of Cd didn't show big difference in the multi–metal sorption column when compared with the single–metal columns. This was expected due to the presence of the competitive metals for sulfide. Comparing the data obtained for Cu, Pb, Cd, and Zn in the multi–metal column, there was a strong relationship between metal removal efficiencies and their solubility products of metal sulfides. In this regard, metals with lower solubility products are easily sorbed to a greater extent (Vidal et al., 2009).

4.4.3 Contents and speciation of metals in the used NPyr

After sorption breakthrough occurred, the corresponding metal(s) and Fe contents in the NPyr particles sampled from different column depths are shown in Fig. 4.2. The contents of metals increased with the increase in the column depth for the four single–metal sorption columns, confirming metal sorption on NPyr particles. After the breakthrough in the four single columns occurred, the contents of Cu, Pb, Cd, and Zn in the used NPyr particles were up to 17.41%, 15.37%, 3.97%, and 8.9% at the bottom of columns, respectively. They were only 1.36%, 2.01%, 0.65%, and 1.81% at the top of columns, respectively. For the multi–metal sorption column (Fig. 4.2 e), the maximum Cu and Pb contents in the used NPyr sorbent were up to 6.80% and 2.50%, respectively. The common grades of natural Cu ore, Pb ore, Cd ore, Cd ore, and Zn ore are just 0.3–0.6% (Northey et al., 2014), 2.8–9% (Ayres, 1997), 0.5–1.5% (Safarzadeh et al., 2007), and 6.2–20%, respectively (Ayres, 1997; Zhao & Stanforth, 2000). The low contents of Zn and Cd in used NPyr particles are in agreement with low Zn and Cd removal efficiencies, which lead to uneconomical extraction of Zn and Cd from the used NPyr particles. However, the much higher Cu contents in the used NPyr particles from both the

single and multi–metal sorption systems than the grades of natural Cu ore, and higher Pb grades in the used NPyr sorbent in the single–metal sorption systems than the common Pb grade in Pb ore make the recovery of Cu and Pb from the used NPyr particles become feasible by using direct metallurgical extraction technologies which are common practice for recovery of metals (Cui & Zhang, 2008; Tuncuk et al., 2012). Hence, the NPyr sorbent can not only efficiently remove Cu and Pb from wastewater, but also effectively recover them.

As Cu and Pb can be more efficiently removed by NPyr than Cd and Zn in single and multi–metal sorption systems (Figs. 4.1 and 4.2), chemical sequential extractions were carried out to determine the solid–phase speciation of Cu and Pb in the used NPyr particles collected from different depths of the single Cu sorption column, the single Pb sorption column, and the Cu–Pb–Zn–Cd column. The contents of the five different species of Cu and Pb are shown in Fig. 4.3. The contents of exchangeable metals (S1), metals bound to carbonates (S2), bound to iron and manganese oxides (S3), and residual metals (S5) were found to be negligible in the total extractable metals. While, Cu and Pb bound to sulfides (S4) accounted for nearly 99% of the total extractable Cu and Pb, similar to our previous study of Cu sorption on calcined colloidal pyrite (Chen et al., 2014a). The results of sequential extraction reveal that metal sulfides were the dominant products for the Cu and Pb sorption by NPyr in both the single and multi–metal columns.

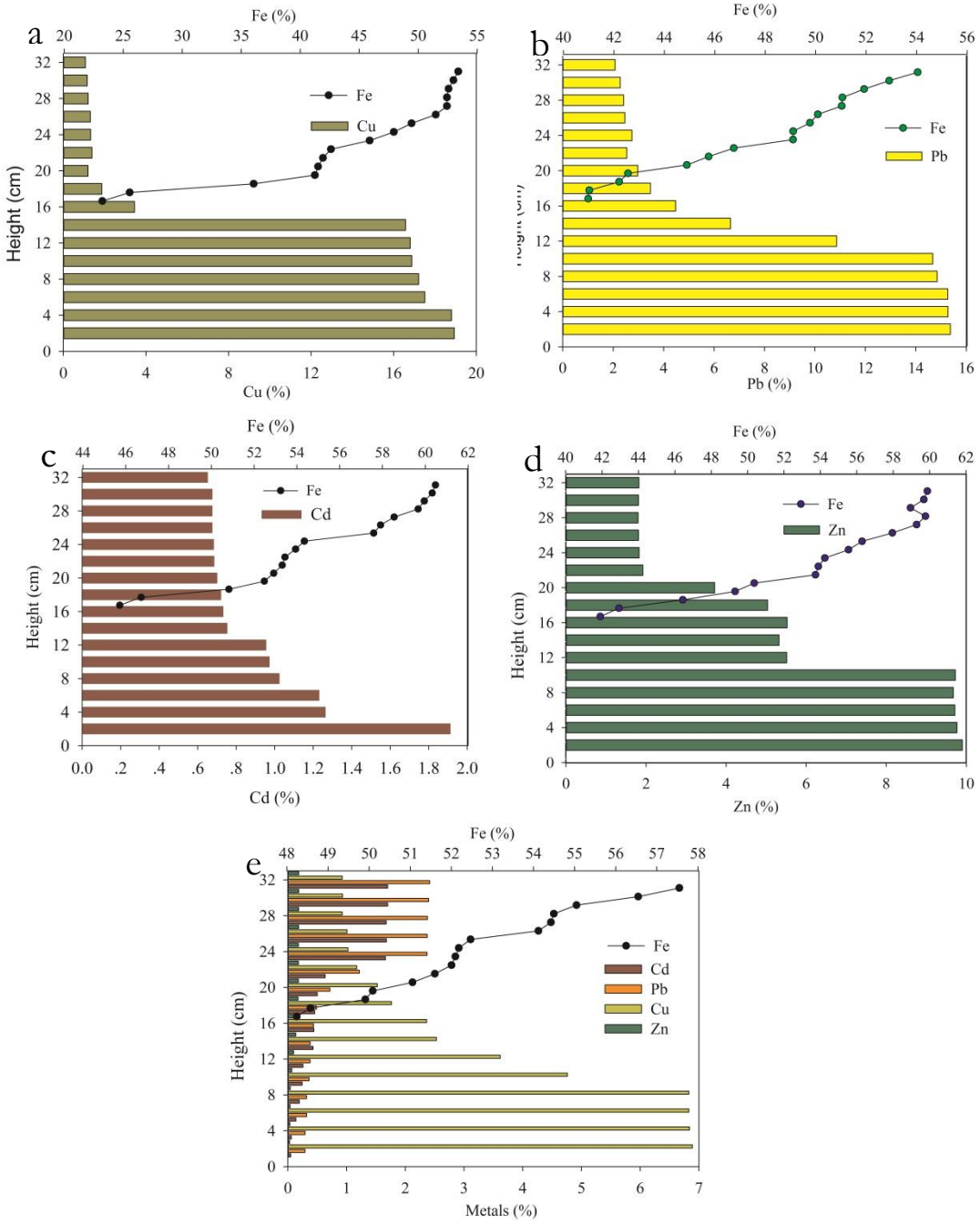

Figure 4.2: Cu, Pb, Cd, and Zn content profiles with the corresponding NPyr column depth (a: Cu column; b: Pb column; c: Cd column; d: Zn column; e: Cu–Pb–Cd–Zn column).

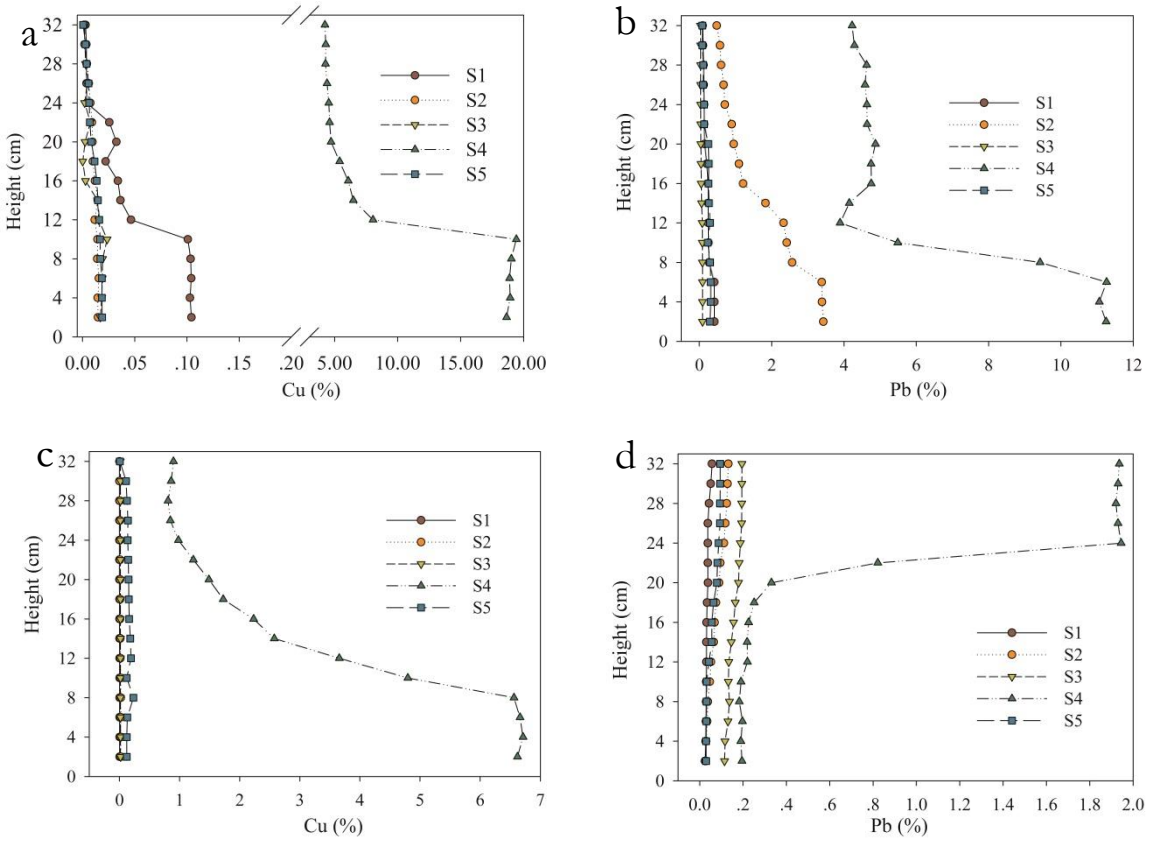

Figure 4.3: Distribution of Cu and Pb species in the used NPyr particles along the column depth

(a: Cu column; b: Pb column; c: Cu–Pb–Cd–Zn column; d: Cu–Pb–Cd–Zn column; S1: exchangeable metal; S2: metal bound to carbonates; S3: metal bound to iron and manganese oxides; S4: metal bound to sulfides; S5: residual metal)

4.4.4 XRD and SEM analyses

XRD and SEM analyses were conducted to determine the major mineralogical composition and the surface morphology of used NPyr paticles sampled from the bottom of single Cu (Fig. 4.4 a–b), and Pb (Fig. 4.4 c–d) columns. Fig. 4.4 a shows that pyrrhotite (JCPDF No. 29–723) and covellite (CuS, JCPDF No. 78–877) were the major phases after the Cu breakthrough

occurred, indicating that secondary covellite crystals were formed. Fig. 4.4 b shows the secondary covellite had a round morphology with average particle sizes of 0.3–0.6 μm. Therefore, it is reasonable to conclude that the dominant copper sulfide in Cu removal by NPyr was in the form of covellite. Fig. 4.4 c shows that pyrrhotite (JCPDF No. 29–723) and galena (PbS, JCPDF No. 78–1055) were the major phases in the used NPyr particles after the breakthrough occurred, indicating that secondary galena crystals were formed. Fig. 4.4 d shows the secondary plates were of submicro–size with irregular morphology, with the average width ranging 0.2–0.5 μm and length 0.3–0.6 μm. Pb was removed from solutions through forming lead sulfide in the form of galena. XRD results reveal that crystals of covellite and galena were formed (Figs. 4.4 a and b). Therefore, it is reasonably concluded that the predominant mechanism of Cu and Pb removal using the NPyr particles was the precipitation of covellite and galena and the dissolution of NPyr (Eqs. 4. 1-2, in which Me represents Cu and Pb).

$$\mathbf{Fe_{1-x}S_{(S)} \leftrightarrow (1-3x)\,Fe^{2+} + S^{2-} + 2x\,Fe^{3+}} \qquad \textbf{(4.1)}$$

$$\text{Ksp of FeS} = [Fe^{2+}]\,[S^{2-}] = 1.59\times10^{-19}$$

$$\mathbf{Me^{2+} + S^{2-} \leftrightarrow MeS} \qquad \textbf{(4.2)}$$

$$\text{Ksp of CuS} = [Cu^{2+}]\,[S^{2-}] = 1.27\times10^{-36}$$

$$\text{Ksp of PbS} = [Pb^{2+}]\,[S^{2-}] = 3.4\times10^{-28}$$

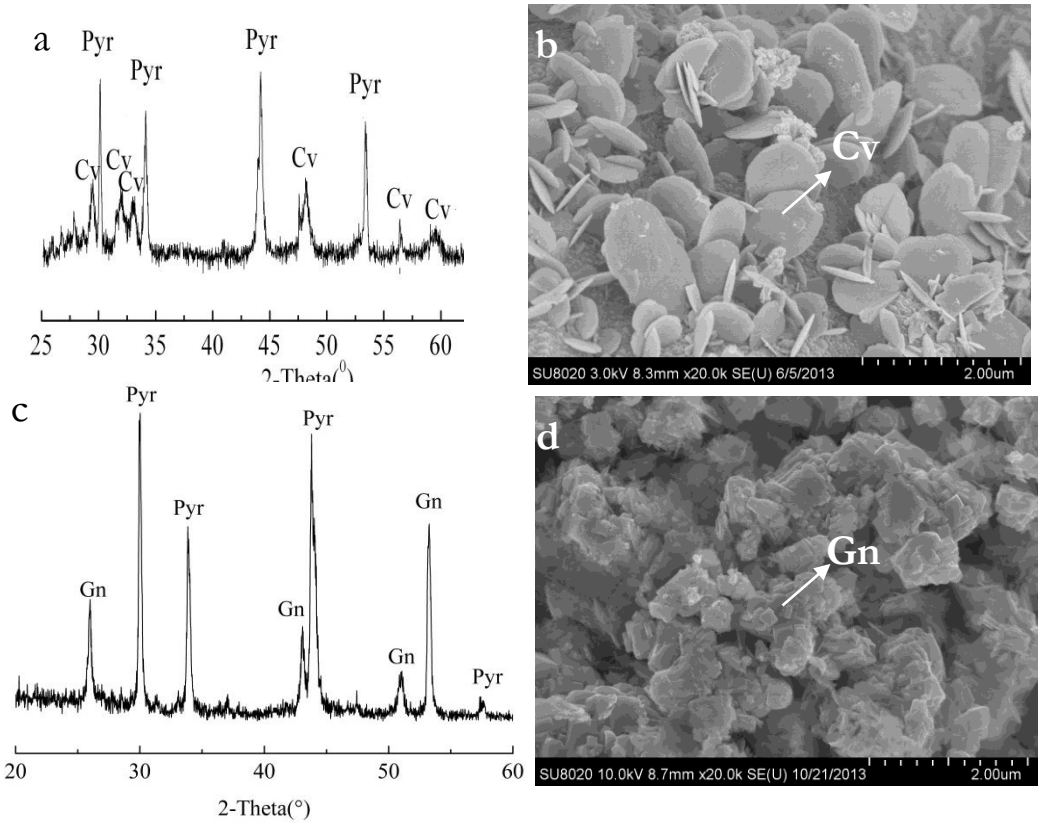

Figure 4.4: XRD (a and c) and SEM (b and d) characterization of the used NPyr particles collected from the bottom of columns after the Cu and Pb breakthrough occurred (a–b: Cu column; c–d: Pb column; Cv: collevite; Gn: galena).

However ZnS and CdS peaks are not presented in XRD spectra of used NPyr particles taken from the single Zn and Cd sorption columns (data not shown), which could be due to insufficient detection limits for Cd (0.8% Cd in NPyr, and 5.8% Zn in NPyr), or no formation of ZnS and CdS crystals probably because their aggregation is not directional under the experimental condition. SEM–EDX analysis was carried out to characterize the surface morphology and elemental composition of the used NPyr sampled from the bottom of single Zn (Fig. 4.5 a) and Cd (Fig. 4.5 b) columns. SEM revealed a large number of nano–meter sized spherical particles formed on the NPyr particles' surface in the Zn column (Fig. 4.5 a). Thus,

it's reasonable to conject that Zn was immobilized from the solution due to the formation of the round nanoparticles on the surface of the used NPyr particles. The obvious peaks of Zn in the EDX confirmed the assumption. Fig. 4.5 b shows little micron–sized cluster was formed on the surface of the used NPyr particles in the Cd column, which corresponded to the low Cd removal efficiency. The EDS of the cluster indicated the removed Cd was immobilized by the cluster, which could be iron (hydr)oxides generated by the oxidation of NPyr or be a cluster of nanoparticles formed due to surface precipitation. The small amounts removed for Zn and Cd are probably due to a combination of precipitation with sorption on the iron oxide/hydroxide surfaces.

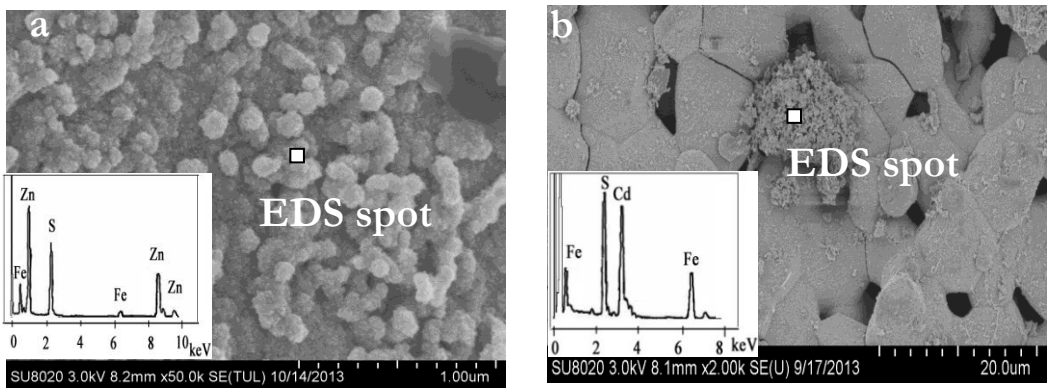

Figure 4.5: SEM–EDS characterization of the used NPyr particles collected from the bottom of columns after the Zn and Cd breakthrough occurred (a: Zn column; b: Cd column).

4.4.5 TEM analyses

Fig. 4.6 shows a TEM image with EDX maps for the used NPyr collected from the multi–metal sorption column. In the Cu–EDX map, the Cu–concentrated areas are characterized by extensive spheroid–shaped particles, suggesting formation of a discrete Cu phase. As later evidenced by the HR–TEM image, this phase was covellite. Meanwhile, in the Pb–EDX map, Pb–concentrated areas are characterized by spheroid–shaped particles with 20–50 nm in diameter, suggesting formation of a discrete Pb phase. The less Pb–concentrated areas than

Cu–concentrated areas were in agreement with the less Pb removal amount than that of Cu. Besides, the areas with lower Zn and Cd densities were homogeneously distributed on the NPyr's surface, indicating the accumulation of Zn and Cd on the NPyr–water interface. The Zn and Cd surface complexes, which were formed at low surface coverages, did not produce sufficient signals to be detected by EDX.

In Fig. 4.7 a, a HR–TEM image exhibits the lattice fringe structures of collevite (CuS), relatively weak modulations with the spacing of ~1.89 Å corresponding to (110) lattice fringes of collevite. In Fig. 4.7 b, the HR–TEM image exhibits the lattice fringe structures of galena (PbS), relatively weak modulations with the spacing of ~2.96 Å corresponding to (200) lattice fringes of galena.

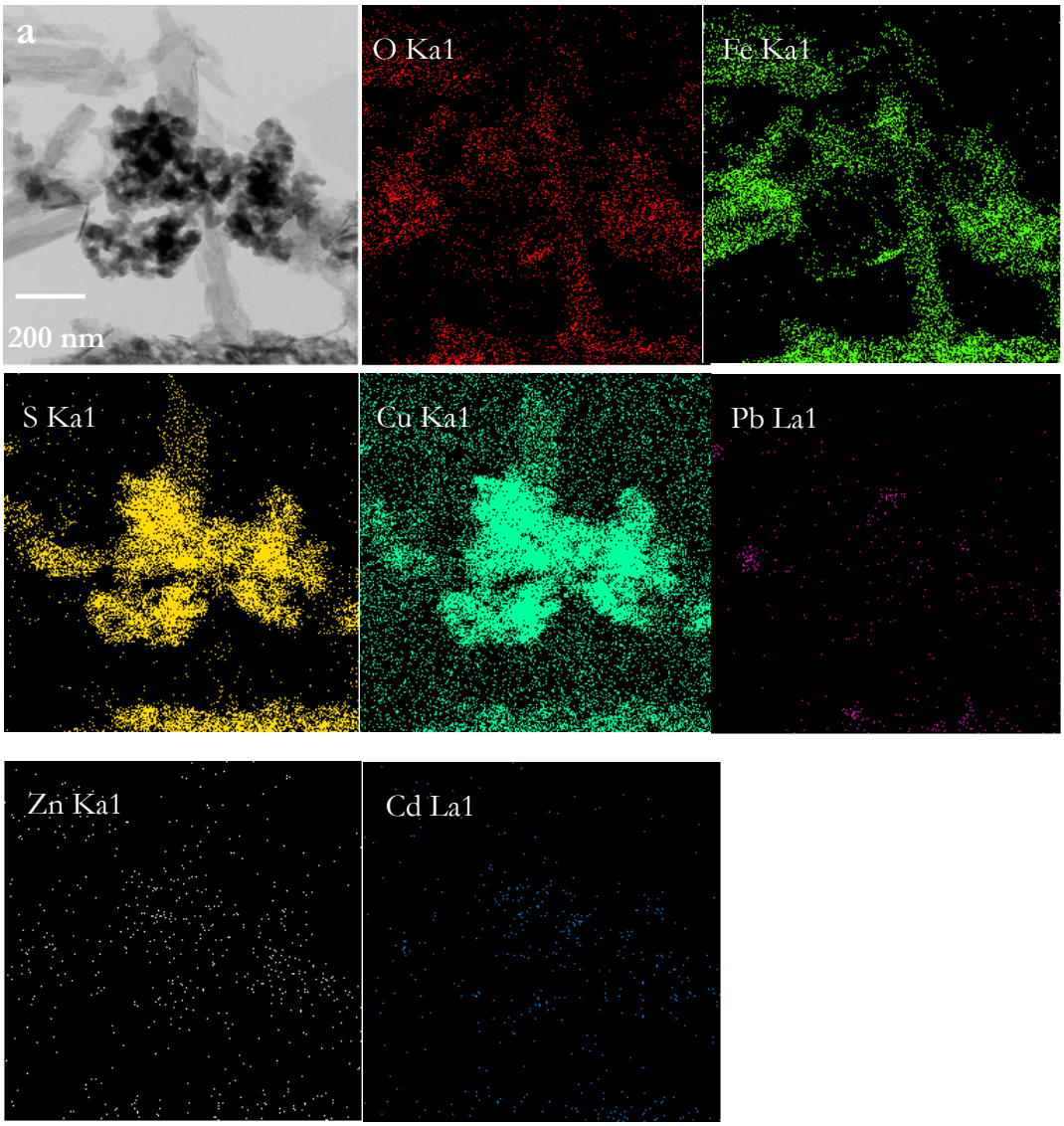

Figure 4.6: TEM micrograph (a) with energy dispersive X–ray (EDX) mapping for different elements (O, Fe, S, Cu, Pb, Zn, and Cd) on the used NPyr collected from the bottom of the Cu–Pb–Cd–Zn column after the breakthrough occurred.

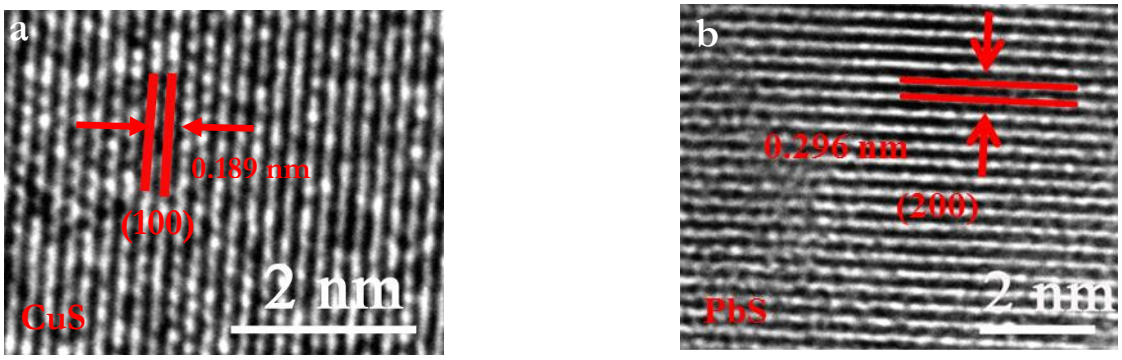

Figure 4.7: HR–TEM micrographs for the Cu–concentrated areas (a) and Pb–concentrated areas (b) of the Cu–Pb–Cd–Zn column after the breakthrough occurred.

The sequential extraction of Cu and Pb, XRD, FE–SEM, and TEM–EDX characterization of the used NPyr particles, and HR–TEM analysis of the secondary crystals indicated that a large amount of covellite and galena were formed on the surface or inner of the NPyr particles. Hence, it is concluded that Cu and Pb were removed from the aqueous solutions mainly due to the formation of covellite and galena, respectively, which were driven by the difference in the solubility products of metal sulfides and $Fe_{1-x}S$ (the dominant product of NPyr). This result is in agreement with the mechanism of Cu removal by calcined colloidal pyrite (Chen et al., 2014a).

4.5 Summary

This study showed that efficient Cu and Pb removal were achieved under the operating conditions with influent concentrations of 100 $mg{\cdot}L^{-1}$ for the single Cu and Pb solutions and 30 $mg{\cdot}L^{-1}$ for the multi–metal solution. The formation of surface precipitates with covellite for Cu and galena for Pb played a dominant role in the Cu and Pb removal by the NPyr particles. Considering the high stability of covellite and galena, their formation would be a significant means of attenuating the hazards posed by Cu and Pb in wastewater. The high Cu and Pb contents in the used NPyr particles sampled from the single and the multi–metal sorption

columns indicate that it is feasible to use NPyr to recover Cu and Pb from wastewater by direct metallurgical extraction following sorption. In Chapter 5, the efficiency of NPyr for metal removal and recovery was further investigated using real AMD wastewater.

Chapter 5

Copper Removal in Real Acid Mine Drainage by Nanostructured Pyrrhotite

5.1 Overview

This Chapter presents the ability of nanostructured pyrrhotite (NPyr) for metal (i.e Cu) removal and recovery from simulated and actual AMD using both batch and column experiments.

5.2 Introduction

As described in previous chapters, acid mine drainage (AMD) is a serious and persistent environmental problem which contaminates soil and surface water. To date, the research for effective methods for AMD treatment has received lots of attention. The main methods are active chemical precipitation by the addition of basic chemical reagents, and passive bioremediation using aerobic wetlands or compost based systems (Maree et al., 2013; Sahoo et al., 2013; Tabak et al., 2003). Both approaches fail to recover potentially valuable metals, such as Cu. It is difficult to recover Cu from AMD by a traditional method with the addition of alkaline reagents to form the precipitates of metal hydroxides compared with the addition of sulfides to form the precipitates of metal sulfides (Macingova & Luptakova, 2012). Because a large amount of Fe in AMD would precipitate as ferric hydroxides, which can act as an adsorbent for Cu and immobilize part of Cu from solution, thus reducing Cu recovery efficiency form AMD. To achieve high efficiency of Cu removal and recovery, we proposed to use nanostructured pyrrhotite (NPyr, $Fe_{1-x}S$) which can immobilize Cu in aqueous solutions onto its surface.

In this research, batch experiments were conducted to elucidate Cu sorption performace on NPyr under varying conditions. A column experiment was carried out to evaluate the efficiency of using NPyr for Cu^{2+} removal and recovery from real AMD.

5.3 Materials and Methods

5.3.1 Materials

The synthesis of NPyr from natural pyrite minerals has been described in Chapter 4.

For the column experiment, limestone was collected from a Cu mine in Yueshan of Anqing City, Anhui Province, China. X-ray diffraction (XRD) analysis of the limestone indicated that calcite was the only carbonate present. The AMD wastewater samples were collected from a pond of Xiangshan Mine located in Ma'an Shan, Anhui, China. Ma'an Shan, one of the top ten steel producing areas in China, abounds in mining resources (Zhang et al., 2006). Farmland and rivers in Ma'an Shan mine area have been highly contaminated by AMD, resulting from the development of the mining industry. After the collection, the AMD samples were stored in polyethylene buckets, which were stored in a dark room at room temperature. The samples were analysed in triplicate, and the characteristics of AMD samples are presented in Table 5.1. Since Cu was the key contaminant of metals in the AMD with 43.16 $mg \cdot L^{-1}$, it's the major focus in this study.

Table 5.1: Chemical composition of acid mine drainage ($mg \cdot L^{-1}$)

pH	NO_3^-	Fe^{3+}	Fe^{2+}	SO_4^{2-}	Ca	Cu	Cd	Zn	As	Pb
2.8	6.8	54.5	16.1	21000	47.5	43.1	0.1	11.3	0.1	0.2

5.3.2 Batch sorption experiments

NPyr is thermodynamically unstable in the presence of O_2, resulting in the formation of iron (hydr)oxides which can act as an adsorbent for metals (Courtin-Nomade et al., 2003). To maintain anoxic conditions, all solutions were flushed with N_2 (g) to drive off any dissolved O_2

(g) prior to reaction, and experiments were conducted in an anaerobic chamber with atmospheric composition of 5% H_2 in N_2. Cu sorption experiments were performed in triplicate using 50 mL polypropylene centrifuge tubes. A control without NPyr was run to account for possible losses resulting from Cu sorption on tubes. HCl and NaOH solutions were added to adjust the initial solution pH between 2 and 6. pH values below 6 were chosen to avoid precipitation of Cu (hydr)oxides. 10 $g{\cdot}L^{-1}$ of NPyr particles and a certain amount of $CuCl_2$ stock solutions were added into the centrifuge tubes to obtain initial Cu concentrations of 10–150 $mg{\cdot}L^{-1}$ (0.16–2.34 mM). The reaction time for batch experiments were 90 h, which was sufficient for Cu sorption (Chen et al., 2013b). The tubes were placed on a rotator with a speed of 40 rpm to ensure complete mixing.

5.3.3 Two-column reactor design

The two-column reactor (A and B, Fig. 5.1) was continually pumped with AMD, which contained Cu of 43.16 $mg{\cdot}L^{-1}$ at a pH of 2.8 (Table 5.1). Each column was made of 50–cm–long transparent glass with an internal diameter of 1 cm. A 10 cm thick layer of crushed glass was placed at both ends so as to prevent NPyr particles from flushing out of the column. 32 cm of crushed limestone was added to Column A, and Column B was packed with the NPyr to a height of 32 cm with a packing density of 1.99 g NPyr· mL^{-1} working volume. The porosity (%) was measured to be 60% for the NPyr. Column A was designed to neutralize AMD and Column B was to evaluate the removal and recovery performance of Cu from real AMD. The AMD was continuously introduced to the bottom of the two-column reactor using a peristaltic pump (BQ50–1J, Lange, China) at a flow rate of approximately 17 $mL{\cdot}h^{-1}$. The hydraulic retention time of Column B was calculated as 0.89 h in consideration of the filling volume of NPyr, the porosity of NPyr, and the flow rate. In Column A, limestone dissolution occurred, resulting in an increase in the pH value and dissolved Ca^{2+} in AMD. Upon exiting Column A, the outflow was directed into the bottom of Column B. When the Cu^{2+} concentration in the effluent of Column B was above 0.5 $mg{\cdot}L^{-1}$, which is the first class

discharge standard for Cu in wastewater in China (GB 8978-1996, China), the breakthrough of the columns occurred.

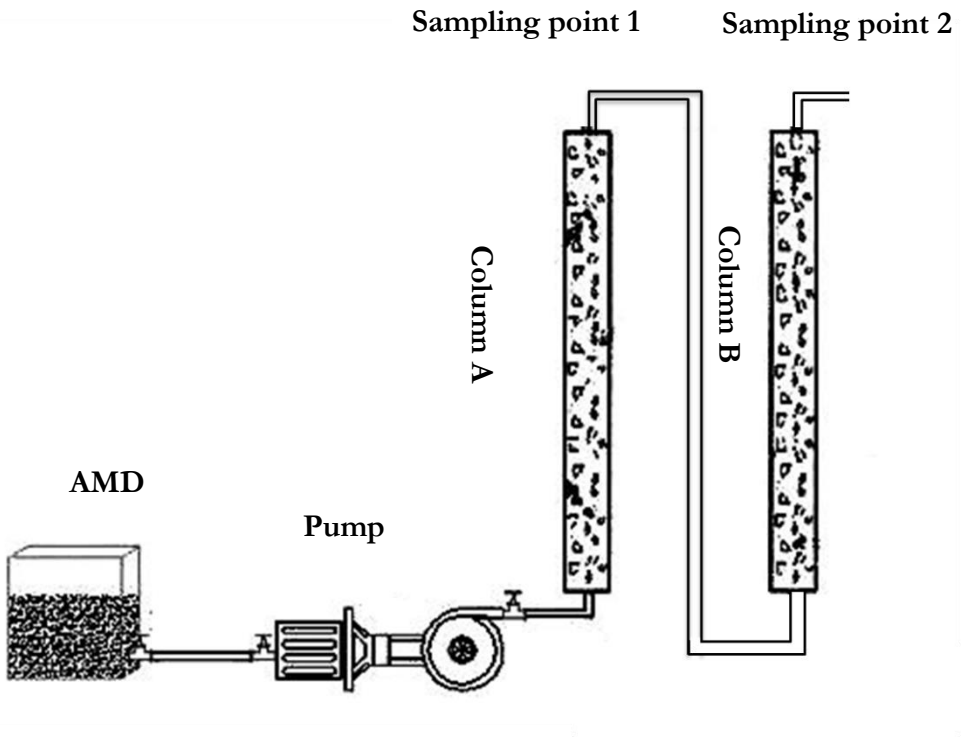

Figure 5.1: Schematic diagram of the two-column reactor

(Column A: limestone; Column B: Nanostructured pyrrhotite)

5.3.4 Analysis methods

The supernatants of the batch sorption experiments and the effluent solutions which were collected from the top of the each column were immediately filtered through 0.45−μm filter paper. Solution pH was monitored using a pH meter (pHS−3C, China). Concentrations of metals, such as Cu, Zn, Cd, and Pb in the filtrates were analysed by an atomic absorption spectrophotometer (WYS2200, China) using the flame atomization technique. Total Fe and Fe^{2+} concentrations in each filtrate were determined by the Ferrozine method (Stookey, 1970).

The method to break down NPyr column after its breakthrough has been introduced in Chapters 3 and 4. Total contents of Cu in the 16 used NPyr samples which were collected from different depths of Column B, were determined by X-ray fluorescence (XRF) (Shimadzu–1800, Japan). High resolution–transmission electron microscopy (HR–TEM) with energy dispersive X–ray (EDX), and (JEOL–2100F, Japan) was used to detect elemental distribution in the used NPyr particles. Furthermore, some of the used limestone samples collected from top, middle, and bottom parts of Column A were analysed by XRD (Dandong Haoyuan-DX-2700, China) to identify crystalline products during the neutralization process.

5.4 Results and Discussion

5.4.1 Sorption experiments

As shown in Fig. 5.2, the Cu removal efficiency was high at the initial pH of 2, was the lowest at initial pH up to 3, and then increased again in the pH range of 4-6, which is in agreement with Ozverdi et al.'s study (2006). At the initial pH of 2, the high Cu removal can be attributed to the generation of H_2S (Eq. 2.1, Chapter 2) and consequently, precipitation of Cu as metal sulfide in solutions according to Eq. 5.1:

$$\mathbf{Cu^{2+} + H_2S \rightarrow CuS + 2H^{+}} \qquad \textbf{(5.1)}$$

Thermodynamically, the concentration of total sulfide is greatest when pH is below 3, and HS^- becomes a significant species of sulfur when pH is in the range of 3-8. When pH increases above the isoelectric point, which lies at pH of 2.7 for NPyr with pyrrhotite as the main component, the surface charge of NPyr becomes more negative (Widler & Seward, 2002). It is easier for positively charged Cu^{2+} to diffuse into the negative surfaces of NPyr. Previously,

precipitation of CuS(s) following dissolution of NPyr was found to be the principal sorption mechanism for Cu sorption on NPyr by fixed-bed columns (Chapter 4). Therefore, it is reasonable to hypothesize that Cu^{2+} on the negative surfaces of NPyr then reacted with soluble sulfide (S^{2-}) arising from NPyr's dissolution to form surface precipitation of CuS. As indicated by Eq. 5.2, the formation of CuS(s) was expected to be accompanied by a release of structural Fe^{2+} in NPyr. To quantify the extent of Fe^{2+} release, dissolved Fe^{2+} was also measured as a function of pH. For comparison, the Fe^{2+} resulting from the dissolution of NPyr without Cu addition under different pH values was also measured, which is indicated by the yellow triangle in Fig. 5.2. The amount of Fe^{2+} released was strongly correlated with the final pH values in Fig. 5.2. At final pH<3, released Fe was higher than the removed Cu, which indicates that a low pH favoured a higher degree of NPyr's dissolution. Then the released Fe was slightly lower than the removed Cu when the final pH was over 3, and there was bigger difference at high pH values. This was attributed to the formation of Fe hydroxy complexes that occurred at pH around 4, and Fe^{2+} became more hydrolyzed as pH increased over the pH range of 4-6.

$$\mathbf{Fe_{1-x}S + Cu^{2+} \rightarrow CuS + (1-3x)Fe^{2+} + 2xFe^{3+}} \qquad \mathbf{(5.2)}$$

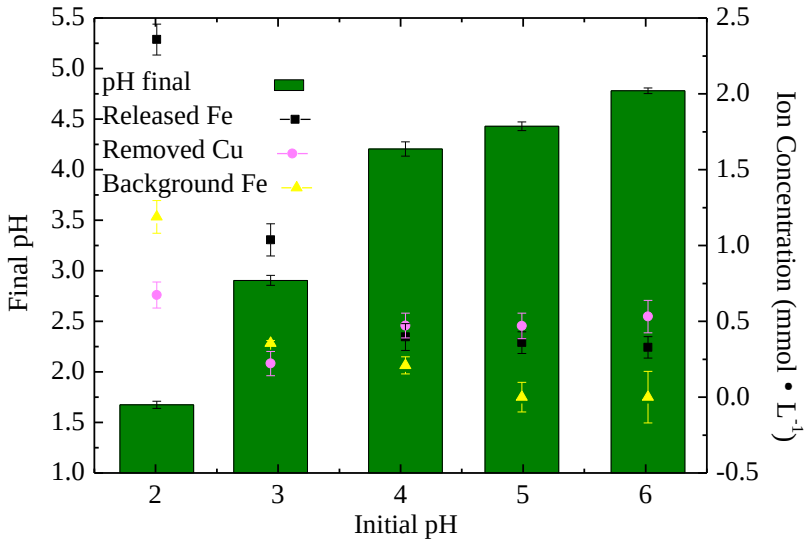

Figure 5.2: Released Fe and removed Cu concentrations as a function of pH in 10 g·L^{-1} NPyr batch experiments

Fig. 5.3 a shows the Cu removal capacity increase with initial Cu concentrations in the range of 10–150 mg·L^{-1}, by considering that the range of Cu concentrations in actual AMD are 2–50 mg·L^{-1}(Motsi et al., 2009; Romero et al., 2011; Sahinkaya et al., 2011b). Cu removal efficiency was 100% when an initial concentration of Cu was 10–20 mg·L^{-1}, and it decreased significantly and then kept stable at 60% when initial concentrations of Cu were 50-150 mg·L^{-1}.

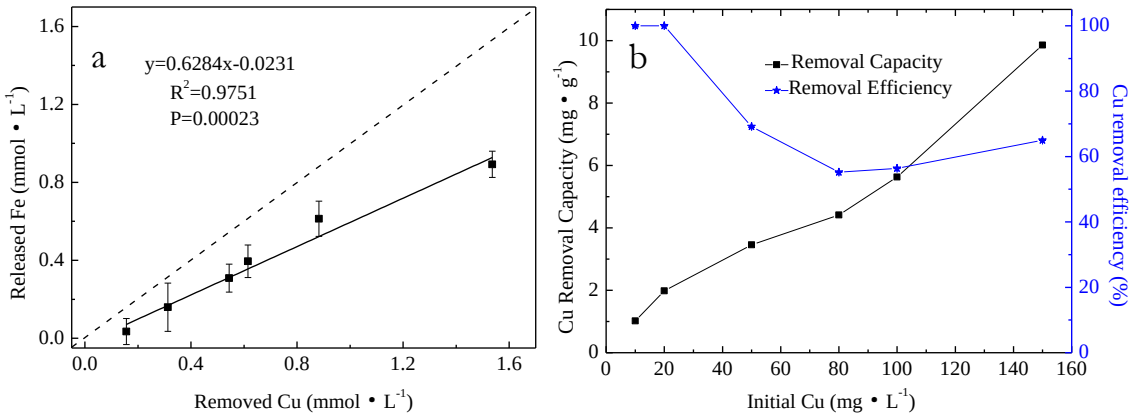

Figure 5.3: Cu removal capacity and efficiency (a) and released Fe (b) versus removed Cu concentration at a pH of 5.0 in 10 g·L^{-1} NPyr batch experiments.

Fig. 5−3 b shows the relationship between the removed Cu and released Fe under different initial Cu concentrations at an initial pH of 5.0. A positive relationship existed between the removed Cu^{2+} (x, mmol ·L^{-1}) and the released Fe^{2+} (y, mmol·L^{-1}). More Fe was released when more Cu^{2+} was removed, and it followed the relationship as y=0.6284x-0.0231 (R^2=0.9751, P=0.0023). If CuS(s) precipitation was the sole sorption reaction for Cu^{2+} removal, the released Fe should be equal to the removed Cu^{2+}, which is represented by the dashed line in Fig. 5.3 b. However, the released Fe is below the dashed line in all cases, implying that adsorption in addition to CuS (s) precipitation were responsible for Cu^{2+} uptake. Fe^{2+} release was approximately 0.63 mol Fe^{2+} per mol Cu^{2+} removed, suggesting that 63% of the removed Cu^{2+} was via precipitation and 37% of the removed Cu^{2+} was by adsorption under these conditions. Similar results have been observed in Hg sorption by synthetic nanocrystalline mackinawite, where the amount of the released Fe^{2+} was below that of the sorbed Hg^{2+} (Jeong et al., 2007).

5.4.2 Fixed-bed column experiment

The above batch study has shown NPyr had a poor removal efficiency for Cu at an initial pH around 3. Considering that the initial pH of the real AMD was 2.8 which was around 3 (Table

5.1), and Cu^{2+} removal efficiency was high in the pH range of 4-6, limestone particles were used as neutralizers to reduce the acidity of AMD in Column A to get a better Cu removal performance in NPyr column. During the column experiment, the pH of the AMD increased to around 4 after the neutralization by limestone in Column A, and it remained nearly constant in Column B during the trial (Table 5.2). Therefore, Cu^{2+} removal by means of hydroxide precipitation was ruled out due to the low pH values in the two-column reactor.

During the experiment, yellow coatings (mainly Fe oxyhydroxides, evidenced by the HR–TEM image in Fig. 5.5) were easily observed on the surface of limestone and NPyr particles in Columns A and B. The Fe oxyhydroxides resulted from the precipitation of dissolved ferric iron in the AMD, which can easily hydrolyze at pH above 3. However, no Fe mineral phases were identified by XRD characterization of the used limestone probably due to the poorly crystalline phases of Fe oxyhydroxides (Bigham, 1994). Fe hydroxide coatings have an ability to remove trace metals from solutions by sorption and co-precipitation (Burgos et al., 2012; Sánchez et al., 2006). However, concentrations of other metals (Cd, Zn, and Pb) showed no measurable reduction while the AMD passed through Column A (Table 5.2), indicating that the adsorption of metals on Fe oxyhydroxides in Column A was insignificant in this study. Furthermore, except for Cu, there was also no significant reduction in the concentrations of Cd, Zn, and Pb in the AMD in NPyr column throughout the running period (Table 5.2). This was likely due to higher solubility products (Ksp) of Cd, Zn, and Pb sulfides compared to that of Cu sulfide, which are in the order of ZnS >PbS> CdS> CuS (Wei & Qi, 2002). Metal sulfides with the lower Ksps would precipitate and those with larger Ksps remain in solution when the concentration of soluble sulfide (S^{2-}) is limited. Therefore, Cu which has the lowest Ksps of CuS in the above metals, had the priority to precipitate as copper sulfide.

Table 5.2: Effluent metal concentrations of the two-column reactor (Column A limestone and Column B NPyr) after passage of various bed volumes (BVs)

Column	BVs	pH	Zn ($mg \cdot L^{-1}$)	Pb ($mg \cdot L^{-1}$)	Cd ($mg \cdot L^{-1}$)	Ca ($mg \cdot L^{-1}$)
A	1	4	11.28	0.22	0.16	83.70
B	1	3.9	10.55	0.18	0.13	66.13
A	170	4	11.25	0.22	0.13	87.39
B	170	4	11.12	0.19	0.14	69.87
A	855	4	11.26	0.22	0.16	82.69
B	855	4.1	11.08	0.2	0.14	67.79
A	1540	4	11.27	0.22	0.17	81.42
B	1540	4	11.32	0.22	0.15	65.48

The Cu breakthrough curve which was plotted giving the ratio of effluent and influent concentrations (C/Co) to bed volumes (BV) is presented in Fig. 5.4 a. Breakthrough of NPyr column occurred until the throughput volume was up to 1000 BV. The breakthrough capacity was calculated to be 21.93 mg $Cu \cdot g^{-1}$ NPyr according to the method described in Chapter 3. It was 77.42 mg $Cu \cdot g^{-1}$ NPyr in single Cu solution (Chapter 4), which is much (3.5 times) higher than that of this study. This indicates the column had a capacity to remove Cu until the throughput volume was up to 3500 BV. The lower breakthrough capacity in this study might be explained by the precipitation of Fe oxyhydroxides (discussed above) and gypsum ($CaSO_4$, as later evidenced by the HR–TEM image in Fig. 5.5) on NPyr's surface. The dissolution of limestone and precipitation of $CaSO_4$ can be expressed by Eq. 5.3, which led to the development of a compact material on NPyr particles (Sahoo et al., 2013). The iron oxyhydroxide coatings and gypsum were easy to form on the NPyr's surface, which passivated the sulfide by restricting infiltration of S^{2-} and made it less accessible to Cu in solution.

$$CaCO_3 + SO_4^{2-} + 2H^+ + H_2O \rightarrow CaSO_4 \cdot 2H_2O + CO_2 \qquad (5.3)$$

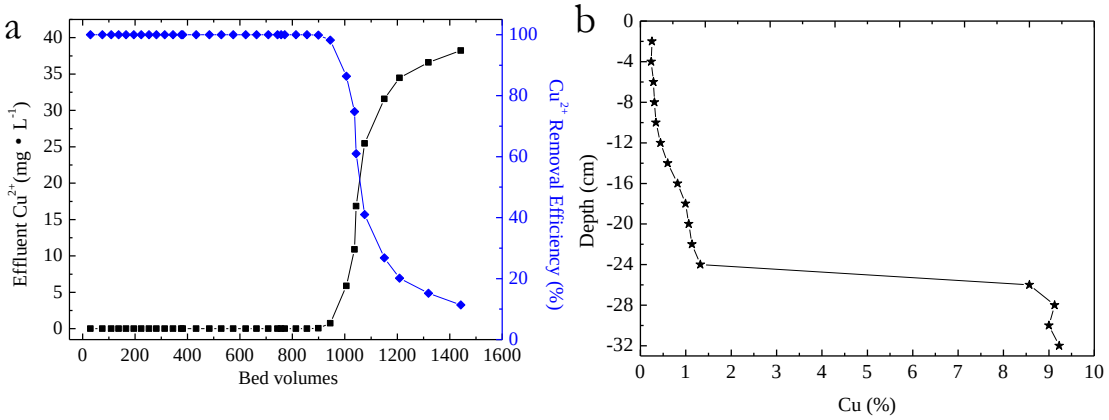

Figure 5.4: Cu^{2+} concentrations in the effluent from Column B (a) and Cu^{2+} contents in the used NPyr particles along the depths of Column B (b)

Even though the inactivation of iron-oxyhydroxides and gypsum, NPyr still had a considerable removal capacity for Cu from real AMD as compared with the removal capacities of other sorbents for metals which were obtained using batch sorption experiments, such as dried digested sewage sludge with 5.3 $mg \cdot g^{-1}$ (Hughes et al., 2013), non-viable activated sludge with 5.9 $mg \cdot g^{-1}$ dry biomass (Utgikara et al., 2000), and natural zeolite with 3.37 $mg \cdot g^{-1}$ (Motsi et al., 2009). The results indicate that NPyr is a promising reactive material for the in situ Cu removal from Cu contaminated AMD.

The Cu contents in the used NPyr particles sampled from different depths of Column B after Cu breakthrough are shown in Fig. 5.4 b. After the sorption breakthrough, elevated Cu contents in the NPyr particles were observed with nearly 9.23% at the bottom and approximately 0.25% at the top of the column. The average Cu content in NPyr particles of Column B was found to be 2.37%. The value is a bit higher than the average Cu contents calculated from the breakthrough capacity with 21.93 mg $Cu \cdot g^{-1}$ NPyr. This could be well

explained by the phenomenon that Cu concentration in the outlet flow was slightly lower than in the inflow even after Cu breakthrough occurred, confirming Cu removal still existed in Column B. Maximum Cu contents of 9.23% in the used NPyr particles would make direct metallurgical extraction of Cu from NPyr particles feasible. From this perspective, the used NPyr particles can be considered as 'Cu ores', and serve as secondary raw materials to meet the persistent growing demand for primary Cu sources. Therefore, desorption of Cu from the used NPyr was not considered here.

Fig. 5.5 shows a TEM micrograph with energy dispersive X–ray (EDX) maps for the used NPyr after the treatment of AMD. In the Cu– and S– EDX maps, Cu–concentrated areas are found to be S–concentrated areas, indicating the formation of CuS on NPyr's surface. Meanwhile, the Ca–concentrated areas relating to O– and S–concentrated areas indicate the formation of gypsum. In addition, the area enrichs in Fe and O, indicating the formation of iron oxyhydroxides. When the NPyr particles' surfaces were progressively coated by copper sulfide, gypsum, and iron oxyhydroxides, it lost its capacity for Cu removal (Fig. 5.6).

Our method offers several important advantages over the traditional method for metal removal from AMD which is by the addition of precipitant to form hydroxide precipitates. No costly chemicals, and complex operations are required. The treatment process was a simple addition of NPyr mineral into reactors to treat the wastewater. Cu was precipitated out as CuS (s) and removed completely from Cu-bearing AMD liquid phase. Furthermore, the solid residue of NPyr particles which contain a certain amount of Cu could be high enough for economic Cu recovery. As a result, the quantity of the solid waste generated by this method was much smaller than that produced by other chemical precipitation methods. The problem which usually associated with the traditional method with the production of large quantities of secondary hazardous wastes was avoided.

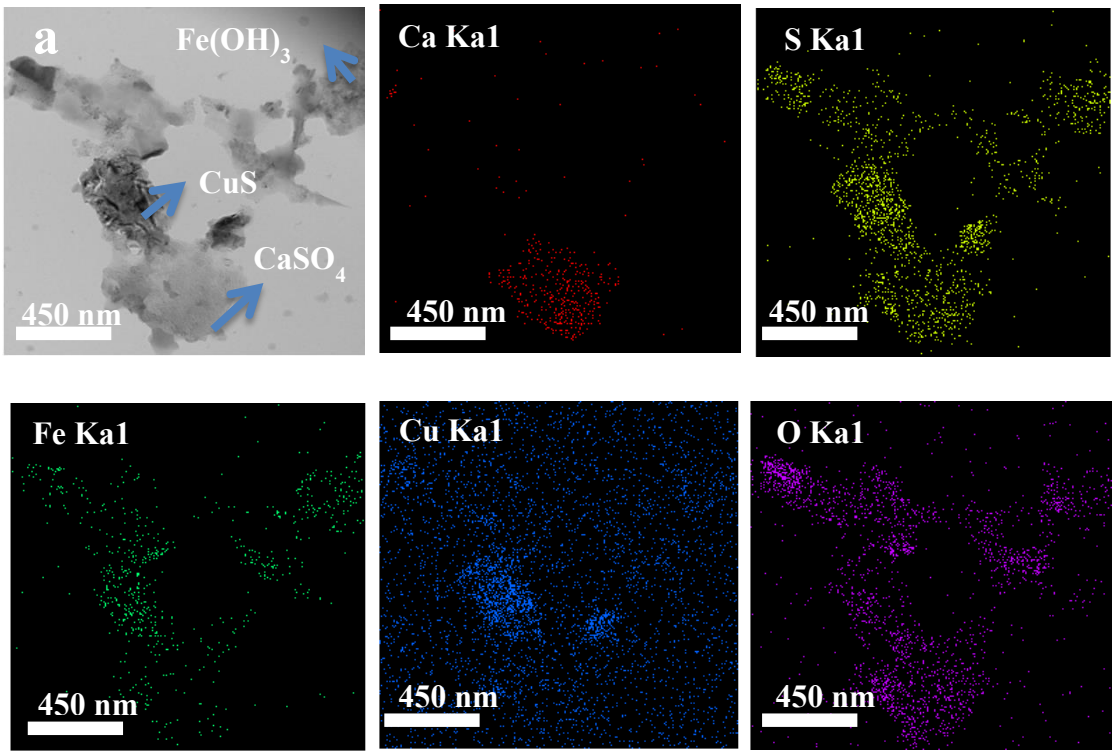

Figure 5.5: TEM–EDX maps for different elements (calcium, sulfur, iron, copper, and oxygen) for the used NPyr collected from the bottom of NPyr column

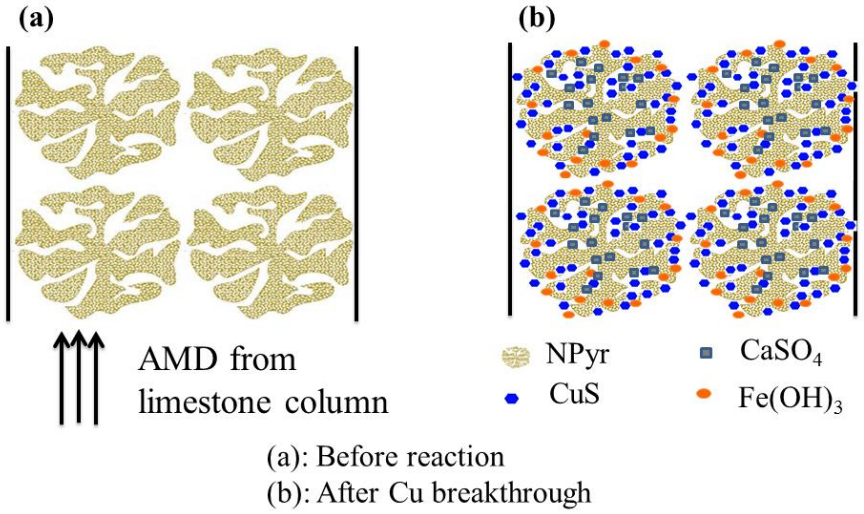

Figure 5.6 Schematic diagram of Cu removal from AMD using NPyr

5.5 Summary

This study reveals that the maximum Cu content was up to 9.23% in the used NPyr particles, which makes direct metallurgical extraction of Cu from the used NPyr feasible. From this perspective, the used NPyr particles can be considered as 'Cu ore', and can serve as a secondary raw material in the context of a growing demand for primary Cu sources. We are developing this remediation strategy using NPyr that allow metals to be removed from mine waters, producing 'clean' precipitates that can be recovered and recycled.

Moreover, the reduced S and Fe species in NPyr can be used as energy sources for autotrophic denitrifiers to reduce NO_3^- to N_2 gas and be used for PO_4^{3-} removal, respectively. The efficiency and mechanisms of nutrient removal from wastewater using NPyr were assessed in Chapters 6 and 7.

Chapter 6

Enrichment and Characterization of Sulfur-based Autotrophic Denitrifiers from Anaerobic Sludge

6.1 Overview

This Chapter presents an efficient and cost-effective method to enrich sulfur-based autotrophic denitrifiers from anaerobic sludge collected from a municipal wastewater treatment plant.

6.2 Introduction

Sulfur-based autotrophic denitrification has been successfully employed to remove nitrate from groundwater, drinking water, and secondary effluent wastewater for over 35 years (Sahinkaya et al., 2014; Shao et al., 2010). As a specialized microbial consortium is required for the process, it is necessary to have simple, time-saving, cost-effective and reliable method to enrich sulfur-based autotrophic denitrifiers. Previous studies have successfully enriched sulfur-based autotrophic denitrifying biomass from anaerobic sludge as seed inoculum for nitrate removal in wastewater (Li et al., 2013b; Moon et al., 2006; Oh et al., 1998; Pu et al., 2014; Sierra-Alvarez et al., 2007). However, the main focus of these studies was on the efficiency of nitrate removal. There was no detailed characterization of the enriched microbial community structure.

In this study, sulfur-based autotrophic denitrifiers were enriched from anaerobic sludge separately using thiosulfate ($Na_2S_2O_3 \cdot 5H_2O$) and natural pyrite (FeS_2) as substrates. These enrichments will be provided to the following lab research (Chapter 7). 16S rRNA-based techniques including terminal restriction fragment length polymorphism (TRFLP) and Illumina sequencing were applied to detect the community development over time and to determine the composition of the bacterial community of the final enrichment culture.

6.3 Materials and Methods

6.3.1 Enrichment of sulfur-based autotrophic denitrifiers

Anaerobic sludge taken from Mutton Island Waste Water Treatment Plant in Galway, Ireland, was used as the inoculum to enrich autotrophic denitrifiers. Total solids (TS) concentration of the sludge was 25 $g{\cdot}L^{-1}$, which was determined using the Standard Methods (APHA et al., 1998). Two separate enrichment cultures were prepared using either pyrite (diameter, 250-450 μm) or thiosulfate, as the electron donors. Natural pyrite minerals were collected from Xinqiao Mine of Tongling City, Anhui Province, China. The medium for the thiosulfate enrichment was prepared using deionized water containing ($g{\cdot}L^{-1}$): $Na_2S_2O_3{\cdot}5H_2O$, 5; K_2HPO_4, 2; KNO_3, 2; $NaHCO_3$, 1; NH_4Cl, 0.5; $MgCl_2{\cdot}6H_2O$, 0.5; and $FeSO_4{\cdot}7H_2O$, 0.01 (Koenig & Liu, 2001). $NaHCO_3$ and $FeSO_4{\cdot}7H_2O$ were filter-sterilized and were added after autoclaving due to their instability during autoclaving. $Na_2S_2O_3{\cdot}5H_2O$ and $FeSO_4{\cdot}7H_2O$ were replaced by pyrite (2.5 $g{\cdot}L^{-1}$) and NaCl (0.01 $g{\cdot}L^{-1}$) in the medium for pyrite fed enrichments. The autotrophic denitrification processes for thiosulfate (Eq. 6.1) and pyrite (Eq. 6.2) occur according to the following equations (Cardoso et al., 2006; Torrentó et al., 2011; Zou et al., 2016):

$$\mathbf{S_2O_3^{2-} + 1.6\ NO_3^- + 0.2\ H_2O \rightarrow 2SO_4^{2-} + 0.8\ N_2 + 0.4\ H^+} \qquad \textbf{(6.1)}$$

$$\mathbf{5FeS_2 + 14\ NO_3^- + 2\ H_2O \rightarrow 10SO_4^{2-} + 7\ N_2 + 4OH^- + 5Fe^{2+}} \qquad \textbf{(6.2)}$$

Enrichment cultures were started with 50 mL anaerobic sludge, and 500 mL culture medium. Cultures were flushed with N_2 for 20 min, sealed with rubber stoppers, and incubated at 30°C. Each stopper had an outlet connected to a syringe to collect gas during denitrification. Enrichment cultures were subcultured when approximately 110 mL of gas was produced, based on the maximum possible gas production from 2 $g{\cdot}L^{-1}$ KNO_3 in the medium, calculated using Eq. 6.1. Seven subcultures (S1–S7) were performed over the course of the 49 d

enrichment based on the enrichment time from previous studies (Li et al., 2013b; Pu et al., 2014).

6.3.2 Microbial community analysis

6.3.2.1 DNA extraction and Illumina sequencing

Biomass from the anaerobic seed sludge, and from S1-S7 (immediately prior to subculturing), were collected for DNA extraction. Samples were flash-frozen in liquid nitrogen, then stored at -80°C until required. Samples (6 mL) were defrosted at room temperature and centrifuged at 4,000 g for 2 min to concentrate biomass. DNA was extracted from resulting pellets using a Maxwell 16 Tissue DNA Purification Kit and a Maxwell 16 Research Instrument System (Promega). All DNA extractions were visualized on 1% (w/v) agarose gels containing SYBR Safe under UV light (Thermo Scientific, UK). Extracted DNA was quantified using the Broad-Range Qubit Assay (Life Technologies). The V4 region of the 16S rRNA genes was polymerase chain reaction (PCR)-amplified using Golay barcoded primers (Caporaso et al., 2012) and the KAPA HiFi HotStart PCR Kit. The F515 and R806 primers (Caporaso et al., 2012) were used with the following conditions: initial denaturation at 95°C for 5 min; with 25 cycles of 98°C for 20 s, 60°C for 15 s and 72°C for 40 s; followed by final extension at 72°C for 1 min. PCR products were gel-purified and quantified using the High-Sensitivity Qubit Assay (Life Technologies). The pooled multiplexed library normalized to 5 $ng \cdot ul^{-1}$ DNA was sequenced using the Illumina Miseq bench-top sequencer. Data were processed and quality assessed according to the Illumina Amplicons Processing Workflow (http://userweb.eng.gla.ac.uk/umer.ijaz#bioinformatics). The alpha diversity was expressed by Shannon. The Shannon diversity index H was calculated as follows: $H = -\sum (pi \ln(pi))$ where pi is the proportion of an individual taxonomic unit relative to all sequences analyzed (McArt et al., 2012).

6.3.2.2 TRFLP fingerprinting

Bacterial 16S rRNA genes from DNA recovered from S1–S7 were PCR amplified using primers: 63F (labeled with FAM 6-carboxyfluorescein) and 518R as follows: an aliquot of 2 µl DNA was added to respective PCR mixtures of 1 µl of each prime (10 µM), 35.5 µl DEPC H_2O, 10 µl PCR buffer (Bioline), and 0.5 µl My*Taq* polymerase (Bioline). The amplification protocol was: 1 min at 95°C, and 30 cycles of 15 sec at 95°C, 15 s at 55°C and 15 s at 72°C, followed by 10 min at 72°C. Amplicons were purified using a Wizard SV gel and PCR Clean-Up System (Progema), and quantified using a Qubit Fluorometer (Invitrogen). PCR amplicons were digested using Alu I enzyme (Promega) following the manufacturers instructions. Restriction digestates were typed using an applied biosystems capillary electrophoresis systems. TRFLP profiles were aligned using T-align programme (Smith et al., 2005) and statistical analyses was performed using Primer 6 (Clarke, 1994). A Bray–Curtis resemblance matrix of square root transformed abundance data was generated and a non-metric multidimensional scaling (NMDS) plot was used to visualize the differences in bacterial community structures between the samples.

6.3.3 Test of the specific denitrification rate

The specific autotrophic denitrification rate of S7 was examined in 60-mL serum vials at 30°C in triplicate. The vials contained 40 mL culture medium with varying concentrations of NO_3^--N (30 mg·L^{-1}, 50 mg·L^{-1}, and 80 mg·L^{-1}). In addition, two sets of negative controls, one without biomass and the other without NO_3^--N, were included to correct for NO_3^--N reduction not associated with autotrophic denitrification. The culture medium was also supplemented with resazurin (0.001 g·L^{-1}) as a redox indicator. The headspace (20 mL) in each vial was flushed with argon gas for 5 min and autoclaved. Filter-sterilized L-Cysteine was added to each vial to the concentration of 0.5 g·L^{-1} as an oxygen scavenger. Biomass concentration in the vials was 4.33 g VSS·L^{-1}. Temporal biogas production in all vials was

monitored using a pressure transducer (Model PSI-15, Ireland) (Campos et al., 2008). The gas was assumed to be $N_{2(g)}$ under nitrate limiting conditions when the $S_2O_3^{2-}$-S/NO_3^--N (m/m ratio) was higher than 3.85 as required stoichiometrically according to Eq. 6.1 (Campos et al., 2008). Denitrification rates were calculated from the slope of the cumulative volume of biogas production in the headspace over time and related to the biomass concentration in the vials. In assays with an initial NO_3^--N concentration of 30 $mg{\cdot}L^{-1}$, NO_3^--N, NO_2^--N and SO_4^{2-} concentrations were determined by ion chromatography. Dissolved nitrous oxide (N_2O) was analyzed continuously by a N_2O microsensor (Unisense, Denmark), and the method of quantifying N_2O emission and generation is detailed by Quan et al. (2012).

6.4 Results and Discussion

6.4.1 Bacterial community succession with the enrichment

With thiosulfate as the substrate, for each subculture, the maximum accumulation of gas resulting from autotrophic denitrification was reached after seven days. However, there was no observed gas production when pyrite was used as the substrate. Therefore, pyrite was determined to be a poor electron donor for sulfur-based autotrophic denitrification compared with thiosulfate during the enrichment. This can be attributed to limited mass transfer due to low solubility and low specific surface area of natural pyrite, which deem it not favorable for the microbial growth (Cardoso et al., 2006). As pyrite was an unsuitable substrate for the enrichment of autotrophic denitrifiers. Thus, analyses below were with the samples collected from thiosulfate fed enrichments.

Bacterial community succession of each subculture along the enrichment is shown in Fig. 6.1. The community developed significantly from S1-S3, but the S4-S7 communities were more similar to each other. There was an increase in similarity with the increase in the times of subculturing. The high level of similarity in the microbial community after S4 is in agreement

with Li et. al's study (2013b), indicating that successful enrichment of autotrophic denitrifiers was achieved after four subcultures over 28 d when using thiosulfate as the substrate. Therefore, we suggest that four subcultures can sufficiently enrich an autotrophic denitrifying community from anaerobic sludge.

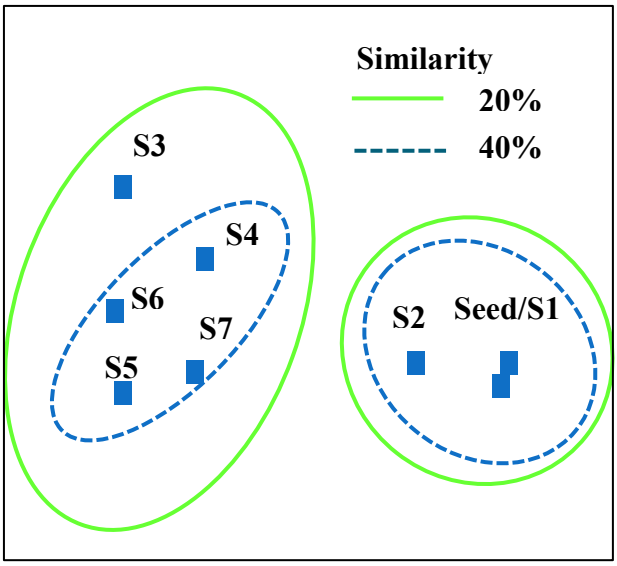

Figure 6.1: 2-D NMDS plots illustrating community succession of TRFLP patterns of each subculture along the enrichment

6.4.2 Bacterial community structure of the enriched culture

The diversity of the community converged from seed sludge to the final enrichment as demonstrated by 16S rRNA sequence analysis (Fig. 6.2). Diversity indices by Shannon were 4.89 for the seed sludge and 0.49 for S7, indicating a temporal reduction of the bacterial diversity. The autotrophic denitrifying bacteria *Thiobacillus* was the relatively dominant group. *Thiobacillus* was the major autotrophic denitrifier reported in most sulfur-based autotrophic biofilters (Shao et al., 2010; Wang et al., 2015). Therefore, the high relative abundance of *Thiobacillus* (55%) in S7 indicated the successful enrichment of the sulfur-based autotrophic

denitrifying community from the anaerobic sludge. Besides a significant enrichment of *Thiobacillus* in S7, the culture also contained *Flavobacteriales*, *Alcaligenaceae, Comamonas*, *Castellaniella*, *Aquamicrobium,* and *Rhizobiales*, presumably indicating heterotrophic metabolism of residual and organic products alongside the predominant autotrophic denitrification. Equally, however, some isolates from the family *Comamonadaceae* which are capable of heterotrophic denitrification were present (3.1%) in S7 (Zhang et al., 2012). Furthermore, in some bacteria from chemolithoautotrophic *Alcaligenaceae* and *Castellaniella* (found 6.2% in S7, Fig. 2), concomitantly oxidation of thiosulfate ($S_2O_3^{2-}$) to tetrathionate ($S_4O_6^{2-}$) can be utilized as an additional energy-yielding reaction by a poorly understood mechanism called the tetrathionate intermediate pathway (Ghosh et al., 2011; Sorokin et al., 2005). In addition, *Aquamicrobium* belonging to the family *Phyllobacteriaceae,* of the order *Rhizobiales,* accounted for 3.1% of S7 sequence, and some species of genus *Aquamicrobium* have been reported as facultatively sulfur-oxidizing chemolithoautotrophic α-Proteobacteria (Alam et al., 2012). Thus, such relatively less abundant populations could have also been contributing to autotrophic denitrification.

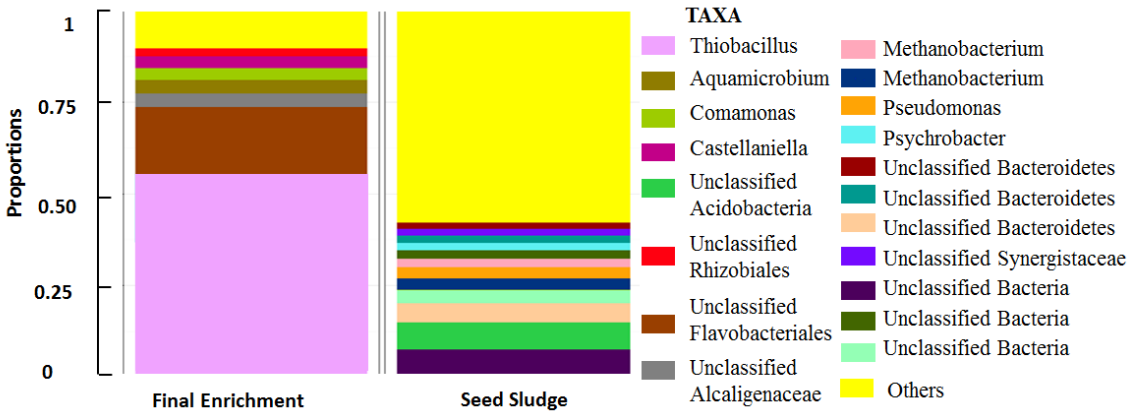

Figure 6.2: Bacterial community composition and relative abundance of the seed sludge and S7.

6.4.3 Denitrification rate of the final enrichment culture

The accumulated volume of gas generated was 0.94, 1.60 and 2.50 mL in assays with initial NO_3^--N concentrations of 30, 50, and 80 mg·L^{-1}, respectively. The volumes of gas generated in assays were close to the theoretically calculated N_2 volumes according to Eq. 6.1 (0.96, 1.6, and 2.56 mL, respectively). This indicates that NO_3^--N removal was through the expected pathway via NO_3^--N reduction to N_2. The specific autotrophic denitrification rate of S7 was calculated to be 21.17 ± 1.75, 19.38 ± 1.24, and 21.82 ± 2.70 mg N_2-N·(g·VSS·d)$^{-1}$ at initial NO_3^--N concentrations of 30, 50, and 80 mg·L^{-1}, respectively, with an average of around 21 mg N_2-N·(g·VSS·d)$^{-1}$. The study of Sahinkaya et al. (2011a) also shows that the denitrification rate did not change significantly at varying initial NO_3^--N concentrations. Therefore, the initial NO_3^--N concentration of 30 mg·L^{-1} was further investigated as a representative for municipal wastewater in the subsequent assays.

Dissolved N_2O was not detectable (below 0.04 mg·L^{-1}) with an initial NO_3^--N concentration of 30 mg·L^{-1}. Thus, the emission of N_2O in thiosulfate system was negligible. Yang et al. (2015) also found that the maximum N_2O gas emission was only 0.405% of the N load when influent NO_3^--N was 70 mg·L^{-1} with H_2S as substrate in a granular sludge autotrophic denitrification reactor. N_2O emissions from sulfide-driven autotrophic denitrification were much lower than those associated with heterotrophic denitrification, which can reach 14.6% of the treated N load (Kampschreur et al., 2009). One reason for such a low N_2O production was the low concentrations of NO_2^--N during NO_3^--N reduction, below 0.5 mg·L^{-1} at all-time points. After the specific denitrification rate trials, there were negligible concentrations of NO_3^--N and dissolved N_2O in the thiosulfate system, indicating a complete utilization of NO_3^--N by S7.

A half-order reaction model based on Monod equations has been widely applied for sulfur-based autotrophic denitrification (Darbi and Viraraghavan 2003; Koenig and Liu 2001). In this

study, application of the half-order reaction model to describe the sulfur-based autotrophic denitrification by Eqs. 6. 3-4 appears to be an appropriate proposition.

$$\frac{dC_{NO_3^- -N}}{dt} = -k_1 C_{NO_3^- -N}^{1/2} \quad (6.3)$$

$$C_{NO_3^- -N,\ t}^{1/2} = C_{NO_3^- -N,\ i}^{1/2} - \frac{1}{2} k_1 t \quad (6.4)$$

where k_1 is the half-order reaction constant for NO_3^--N, $mg^{1/2}L^{1/2}h$; $C_{NO_3^- -N,\ t}$ is the concentrations of NO_3^--N at time t, $mg{\cdot}L^{-1}$; $C_{NO_3^- -N,\ o}$ is the initial concentration of NO_3^--N, $mg{\cdot}L^{-1}$.

The kinetics of autotrophic denitrification was well described by a half-order reaction with $C_{NO3-N}^{1/2} = -0.57\,t + 5.51$ (R^2=0.95, P=0.0002<0.5). The half-order reaction rate was calculated from the slope of the line as 1.14 $mg^{1/2}L^{1/2}h$. The specific utilization rate of NO_3^--N was 16.40 mg NO_3^--N $(g{\cdot}VSS{\cdot}d)^{-1}$ and NO_3^--N was reduced to 0.47 $mg{\cdot}L^{-1}$ in 8 h. This rate is in good agreement with the calculated specific denitrification rate based on gas production, proving the produced gas from denitrification was $N_{2(g)}$. Similarly, near stoichiometric conversion of thiosulfate to sulfate was observed, and the measured SO_4^{2-}/NO_3^--N ratio (Fig. 6.3 c) was 12.85 g/g, similar to the stoichiometric ratio of 11.58 g/g according to Eq. 6.1. The lower experimental SO_4^{2-} values than theoretical values were detected when the removed NO_3^--N was 19.06 and 20.67 $mg{\cdot}L^{-1}$. This might be explained by the formation of intermediate products (e.g. S, $S_4O_6^{2-}$, and SO_3^{2-}) during the oxidation of $S_2O_3^{2-}$ to SO_4^{2-} at this stage (Tong et al., 2016).

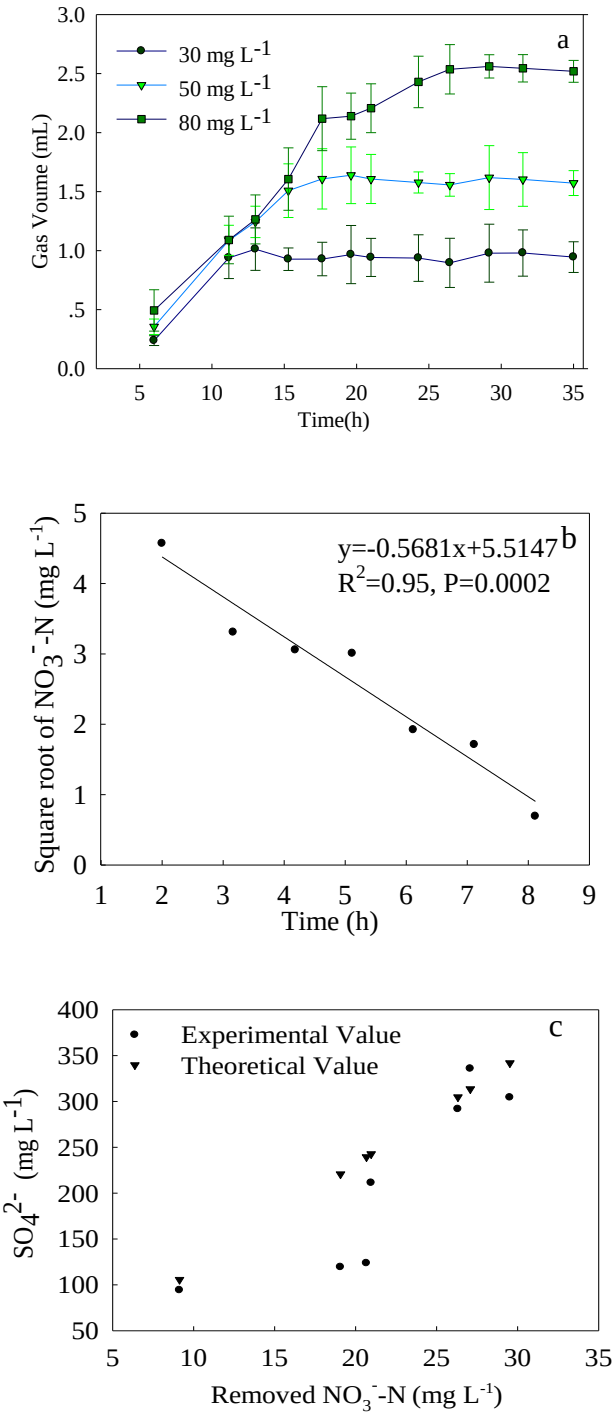

Figure 6.3: Accumulated gas volume at different initial NO_3^--N concentrations (a), square root of NO_3^--N concentration vs. time (b) and SO_4^{2-} production vs. NO_3^--N reduction (c) in the kinetic assay at an initial concentration of 30 mg NO_3^--N·L^{-1}.

6.5 Summary

Thiobacillus-dominating microbial communities which can carry out sulfur-oxidizing autotrophic denitrification were successfully enriched by a convenient, effective and reliable method from anaerobic sludge within 28 days. Illumina sequencing showed that genus *Thiobacillus* had a relative abundance of 55% in the final enrichment culture. The enriched autotrophic denitrifiers showed that a specific utilization rate of NO_3^--N was 16.40 mg NO_3^--N $(g{\cdot}VSS{\cdot}d)^{-1}$ with thiosulfate as the electron donor. The enriched autotrophic denitrifiers were seeded in NPyr-based biofilters. The feasibility and the denitrification capacity of the biofilters for simultaneous removal of NO_3^- and PO_4^{3-} from wastewater are detailed in Chapter 7.

Chapter 7

Nanostructured Pyrrhotite Supports Autotrophic Denitrification for Simultaneous Nitrogen and Phosphorus Removal from Wastewater

7.1 Overview

This Chapter assessed the efficiency of NPyr based autotrophic denitrification biofilters (PADBs) for simultaneous N and P removal from secondary treated wastewater at a variety of HRTs (0.6–7.2 h) using two identical laboratory-scale biofilters.

7.2 Introduction

To control eutrophication, some countries have drafted stringent effluent quality criteria. For example, in sensitive areas, such as South Central Great Plains lakes and Northern Great Plains rivers in the United States, TN must be <1.5 to 3 $mg{\cdot}L^{-1}$and TP <0.07 to 0.1 $mg{\cdot}L^{-1}$ (Oleszkiewicz & Barnard, 2006). To achieve such stringent criteria presents a challenge for tertiary treatment, and technological innovation for further removal of N and P from secondary treated wastewater which is typified by a low organic C/N ratio. As introduced in Chapter 2, PADBs, in which natural pyrrhotite ($Fe_{1-x}S$, $0<x<0.125$) mineral is used as the biofilm substratum for autotrophic denitrification for N and P removal, was developed to reduce N and P to low levels. However, long hydraulic retention times (HRTs), of up to 24 h, was required, which would constrain its application in mainstream wastewater treatment plants (WWTPs).

To make PADB technology applicable, NPyr was used as the substratum in nanostructured PADBs, replacing natural pyrrhotite. In this chapter, the mechanisms and efficiency of NPyr based autotrophic denitrification for simultaneous N and P removal from secondary treated wastewater at short HRTs (0.6–7.2 h) were studied in detail.

7.3 Materials and Methods

7.3.1 Synthesis of NPyr

The synthesis of NPyr from natural pyrite minerals have been detailed in Chapter 4.

7.3.2 Culturing of autotrophic denitrifiers

The method of enriching autotrophic denitrifiers from anaerobic sludge has been introduced in Chapter 6.

7.3.3 Wastewater tested

Synthetic wastewater (pH, 8.35) with 28 mg NO_3^-–N L^{-1} and 6 mg PO_4^{3-}–P L^{-1} was prepared with KNO_3 and KH_2PO_4 dissolved in tap water to simulate secondary effluent from municipal WWTPs.

Secondary effluent monthly taken from a local municipal WWTP, which operates as a conventional, nitrifying activated sludge process, was used as 'real' wastewater in this study. After arriving at the laboratory, it was filtered through 110 mm filter paper to remove the grown algae before being stored at a cold room where the temperature is controlled at 10 °C. During the storage, characteristics of the wastewater did not change much. The filtered wastewater was firstly flushed with N_2 for 15 min, then added in a bag, and eventually pumped to the biofilters from the inlets located at the bottom. The quality of the water in the bag was measured biweekly, and the results are given in Table 7.1, with total oxidized nitrogen (TON: NO_3^-–N + NO_2^-–N) of 13.81 ± 1.52 mg·L^{-1}, NO_2^-–N of 0 ± 0.01 mg·L^{-1}), NH_4^+–N of 0.50 ± 0.05 mg·L^{-1} and PO_4^{3-}–P of 2.44 ± 0.05 mg·L^{-1}.

Table 7.1: Characterization of the real secondary effluent ($mg \cdot L^{-1}$)

pH	TON	P	SO_4^{2-}	COD	Ca
7.34 ± 0.44	13.81 ± 1.52	2.44 ± 0.05	115.25 ± 0.15	22.50 ± 2.12	61.20 ± 8.55

TON: total oxidized nitrogen; COD: chemical oxygen demand

7.3.4 Inoculation and operation of the nanostructured PADBs

Two identical, glass upflow biofilters (diameter, 10 mm; height, 50 cm) were set up in the laboratory. NPyr particles (50 g) were added into each biofilter as biofilm substratum with an effective height of 34.5 cm and a porosity of 60%. The packing density of NPyr particles was 1.85 g/mL. Culturing medium (described in Chapter 6) containing the enriched autotrophic denitrifiers (10% v/v), was flushed with N_2 for 20 min and then continuously pumped into the biofilters at a flow rate of 2.26 $mL \cdot h^{-1}$. The method of inoculation of stable autotrophic denitrifying biofilms on the substratum in PADB has been described by Li et al.(2016). After the inoculation period, which lasted 40 days, the trial was commenced (noted as Day 1), and the synthetic secondary effluent was pumped into the nanostructured PADBs. The phases of the biofilter trial are listed in Table 7.2. The effects of the HRT (0.6–7.2 h) and of the quality of the influent (synthetic secondary treated wastewater during Phases 1–3; real secondary treated wastewater during Phases 4–9) on the performance of the nanostructured PADBs were studied over the 536-day trial. HRT was calculated considering the porosity in the biofilters with Eq. 3.1 (Chapter 3).

Table 7.2: Operational phases in the nanostructured PADB trial

Phase	Day (d)	N (mg/L)	P (mg/L)	HRT (h)	Hydraulic Loading Rate ($m^3 \cdot m^{-2} \cdot d^{-1}$)	Loading (mg NO_3^-–N / L·d)	Q (mL/h)
1	1–128	28	6	7.2	0.69	56	2.26
2	129–155	28	6	5.4	0.92	75	3.01
3	156–233	28	6	3.6	1.38	112	4.51
4	234–381	Real secondary treated effluent		3.6	1.38	55	4.51
5	382–409			3	1.66	66	5.42
6	410–420			2.4	2.07	83	6.77
7	421–440			1.8	2.76	110	9.02
8	441–465			1.2	4.14	166	13.54
9	466–536			0.6	8.28	332	27.08

7.3.5 Sample collection and analysis

Effluent samples were collected from the biofilters every two days, and samples were also taken from different heights of the biofilters after the performance was stable for five successive measurements in each phase. Three sampling points were located at heights of 2.75 cm (bottom), 12.75 cm (middle) and 34.5 cm (top) from the base of the biofilters. Samples were filtered through 0.45-μm syringe filters prior to the determination of TON, NO_3^-–N, NO_2^-–N, PO_4^{3-}–P and SO_4^{2-} using a nutrient analyzer (Konelab 20, Thermo, USA). Total organic carbon (TOC) was detected using a TOC/TP/TN analyser (Biotector, Ireland) and pH was measured using a portable meter (pH 3210, Germany). Samples were acidified by 1% nitric acid to determine metals using Inductively Coupled Plasma Mass Spectrometry (ICP–MS; ELAN DRCe, Perkin Elmer, Waltham, USA) (Ratcliff et al., 2016). Concentrations of Fe^{2+}, S^{2-}, TP, and chemical oxygen demand (COD) of fresh effluent samples were determined using respective HACH test kits (HACH DR 2010, USA). Dissolved N_2O was measured with a N_2O microsensor (Unisense, Denmark), using the method detailed by Quan et al.(2012).

At the conclusion of the nanostructured PADB trial, the used NPyr particles were collected from the three PADB sampling points, gold coated (Emitech K550), and the surface morphology was examined using scanning electron microscopy (SEM, Hitachi S–4700, Japan) (Morrison et al., 2009). The valence state of S on the used NPyr was determined using X–ray photoelectron spectroscopy (XPS, Thermo ESCALAB–250, USA). The used NPyr particles were suspended in ethanol followed by solid dispersion using sonication, and subsequently the suspension was dropped on a 400–mesh copper grid for examination of element distribution and composition using transmission electron microscopy (TEM, JEOL–2100F, Japan) (Han et al., 2012). NPyr particles sampled at different heights of the nanostructured PADBs were used for genomic DNA extraction and high-throughput sequencing of 16S rRNA genes.

7.3.6 DNA extraction and Miseq sequencing

DNA was extracted from 0.05 g of the used NPyr particles using an automated DNA extraction robot (Maxwell 16 Research Instrument System, Promega) according to the manufacturer's instructions and with the associated purification reagents (Maxwell 16 Tissue DNA Purification Kit, Promega). DNA extracts were purified using a Wizard®DNA Clean-Up System (Promega). Purified DNA was quantified using a spectrophotometer (Qubit system, and the Broad-Range Qubit Assay; Life Technologies). The preparation method of DNA for sequencing on an Illumina Miseq platform has been detailed in Chapter 6. Raw sequences were processed with a modified version of the Illumina MiSeq SOP pipeline(James J. Kozich, 2013) in Mother (http://www.mothur.org/wiki/MiSeq_SOP). Filtering of ambiguous base calls (maxambig = 0), amplicon size (maxlength= 300, minlength = 200), barcode mismatches (bdiffs = 0), primer mismatches (pdiffs = 2) and homopolymers (maxhomop = 8) was done following Weigel and Erwin (2016). Sequences were aligned with the Silva database and trimmed to the V4 region. The precluster(Huse et al., 2010) and UChime algorithms were run, and chimeras sequences were removed. OTUs (97%) were constructed after sequences were classified, and non-target reads were removed. Each dataset was subsampled to the lowest read

count (n = 24,312) and all analyses were based on the final subsampled data sets. A threshold of 1% was employed to define rare or abundant taxa, which resulted in a cut-off value of 24 sequences.

7.4 Results and Discussion

7.4.1 Nitrogen removal efficiency and kinetics

The concentrations of TON and NO_2^-–N in the nanostructured PADB effluent are shown in Fig. 7.1. A short adaptation period was observed when the HRT was reduced (except in Phases 3 and 9), and almost complete denitrification (effluent TON, 0.045 ± 0.011 $mg \cdot L^{-1}$; effluent NO_2^-–N, < 0.1 $mg \cdot L^{-1}$) was achieved at steady states during Phases 1–8, indicating that NPyr was an efficient electron donor for sulfur-based autotrophic denitrifiers. This is supported by high-throughput Illumina sequencing data indicating an abundance of chemolithotrophic *Thiobacillus* in the biofilters (65–87% relative abundance of the total bacterial 16S rRNA gene sequences, Fig. 7.2), which can use iron sulfides as electron donors with NO_3^-–N reduction (Bosch et al., 2012). During Phase 3, effluent NO_2^-–N was high (up to 8.96 $mg \cdot L^{-1}$) after the HRT was shortened from 5.4 h to 3.6 h on Day 156, but was undetectable by Day 197. NO_2^-–N accumulation was attributed to the fact that some of the biofilm detached due to the high shear force caused by increasing the influent flow rate from 3.01 $mL \cdot h^{-1}$ to 4.51 $mL \cdot h^{-1}$ (Table 7.2). By Phase 9, when the HRT was 0.6 h, effluent TON was 7.40 ± 1.18 $mg \cdot L^{-1}$, and the N removal efficiency was 46%. Two reasons accounted for elevated effluent TON: (i) a shorter HRT resulting in a higher NO_3^-–N loading rate of 332 $mg \cdot L^{-1} \cdot d^{-1}$ (Table 7.2); and (ii) a limited mass transfer rate of NO_3^-–N to denitrifiers due to precipitation of $FePO_4$ and $Fe(OH)_3$ on NPyr surface (discussed in Section 7.3.2).

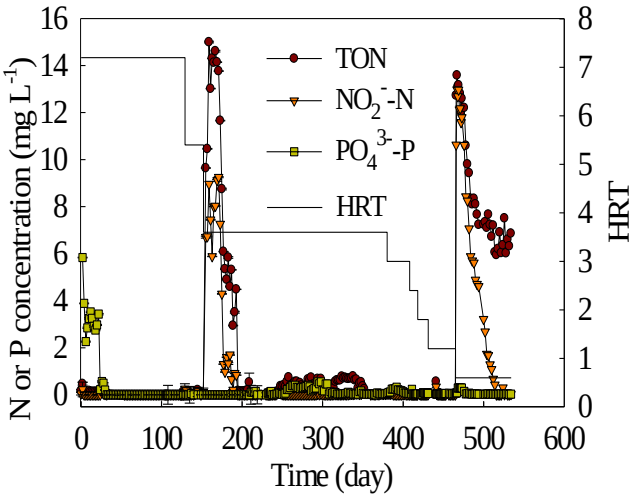

Figure 7.1: N and P concentrations of the effluent from nanostructured PADBs at different HRTs

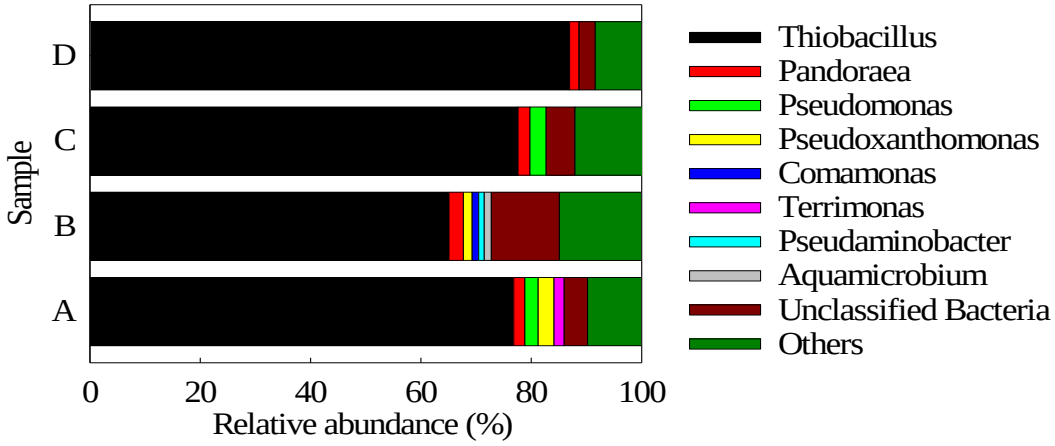

Figure 7.2 Bacterial community structures in the nanostructured PADBs

(A: Bottom of biofilters treating synthetic wastewater; B: Middle of biofilters treating synthetic wastewater; C: Bottom of biofilters treating real secondary wastewater; D: Middle of biofilters treated with real secondary wastewater; all genera present at a relative abundance >1% of total reads; the unclassified indicates the taxonomic information retrieved from Silva database contains missing information at this level).

NO_2^-–N accumulation was observed along the height of the biofilters. NO_2^-–N detected in the middle of the biofilters in Phases 1, 2, and 3 accounted for 25%, 27% and 39%,

respectively, of influent NO_3^-–N (28 mg·L^{-1}). Dissolved N_2O was undetectable along the biofilters. Therefore, a two-step autotrophic denitrification model was proposed, which comprises NO_3^-–N reduction to NO_2^-–N, and NO_2^-–N reduction to N_2, without accumulation of intermediate gaseous products. Sulfur-based autotrophic denitrification is believed to follow the Monod equation in the NPyr biofilm, and the denitrification kinetics can be expressed with zero-order, half-order or first-order models mainly depending on concentrations of NO_3^-–N (Darbi & Viraraghavan, 2003; Koenig & Liu, 2001). In the present study, half-order reaction kinetics best described the two-step NO_3^-–N denitrification of synthetic wastewater, which are expressed in Eqs. 7. 1–2.

$$\frac{dC_{NO_3^- - N}}{dt} = -k_1 C_{NO_3^- - N}^{1/2} \quad (7.1)$$

$$\frac{dC_{NO_2^- - N}}{dt} = k_1 C_{NO_3^- - N}^{1/2} - k_2 C_{NO_2^- - N}^{1/2} \quad (7.2)$$

where, k_1 and k_2 are the half-order reaction constants for NO_3^--N and NO_2^--N per unit volume of the biofilters ($mg^{1/2}L^{1/2}h$), respectively.

Eqs. 7. 3-4 were developed to calculate concentrations of NO_3^-–N and NO_2^-–N at different heights of the biofilters:

$$C_{NO_3^- - N,\ t}^{1/2} = C_{NO_3^- - N,\ i}^{1/2} - \frac{1}{2} k_1 t_h \quad (7.3)$$

$$C_{NO_2^- - N,\ t}^{1/2} = -\left(\frac{k_1}{k_2} C_{NO_3^- - N,\ i}^{\frac{1}{2}} + \frac{{k_1}^2}{{k_2}^2}\right) e^{-\frac{k_2 t_h}{2}} - \frac{{k_1}^2}{2k_2} t_h + \frac{k_1}{k_2} C_{NO_3^- - N,\ i}^{\frac{1}{2}} + \frac{{k_1}^2}{{k_2}^2} \quad (7.4)$$

where, $C_{NO_3^- - N,\ t}$ and $C_{NO_2^- - N,\ t}$ are the concentrations of NO_3^--N and NO_2^--N at different heights of the biofilters, respectively; $C_{NO_3^- - N,\ i}$ is the influent concentration of NO_3^-N; t_h is the empty bed residence time, which is calculated by $\frac{\text{Ahn}}{\text{Q}}$ (A: the cross-section area of biofilm substratum; H is the height from the bottom of the biofilters).

The half-order kinetic models developed were assessed by comparing the measured concentrations of NO_3^-–N and NO_2^-–N and modelled values along the nanostructured PADBs treating synthetic wastewater in Phases 1–3. The measured values fit the modelled values quite well (Fig. 7.3). The half-order reaction rate constants estimated are 1.31, 1.87, and 2.84 $mg^{1/2}L^{1/2}h$ for NO_3^--N (k_1) and 2.21, 2.60, and 3.57 $mg^{1/2}L^{1/2}h$ for NO_2^--N (k_2) at HRT of 7.2 h, 5.4 h and 3.6 h, respectively. These values are comparable to the reaction rates for NO_3^-–N obtained in element-sulfur-based autotrophic denitrification, which were in the range of 1.12–3.52 $mg^{1/2}L^{1/2}h$ (Darbi & Viraraghavan, 2003; Koenig & Liu, 1997; Koenig & Liu, 2001). The half-order reaction constants for NO_3^--N and NO_2^--N increased with the HRT reduction, suggesting faster denitrification kinetics at lower HRTs due to higher mass transfer rates in the biofilm at lower HRTs. In addition, higher reaction constants for NO_2^-–N, than for NO_3^-–N, at different HRTs are in agreement with the finding that significant NO_2^-–N accumulation was observed in the middle of the biofilters but no NO_2^-–N was detected in the effluent (Fig. 7.3).

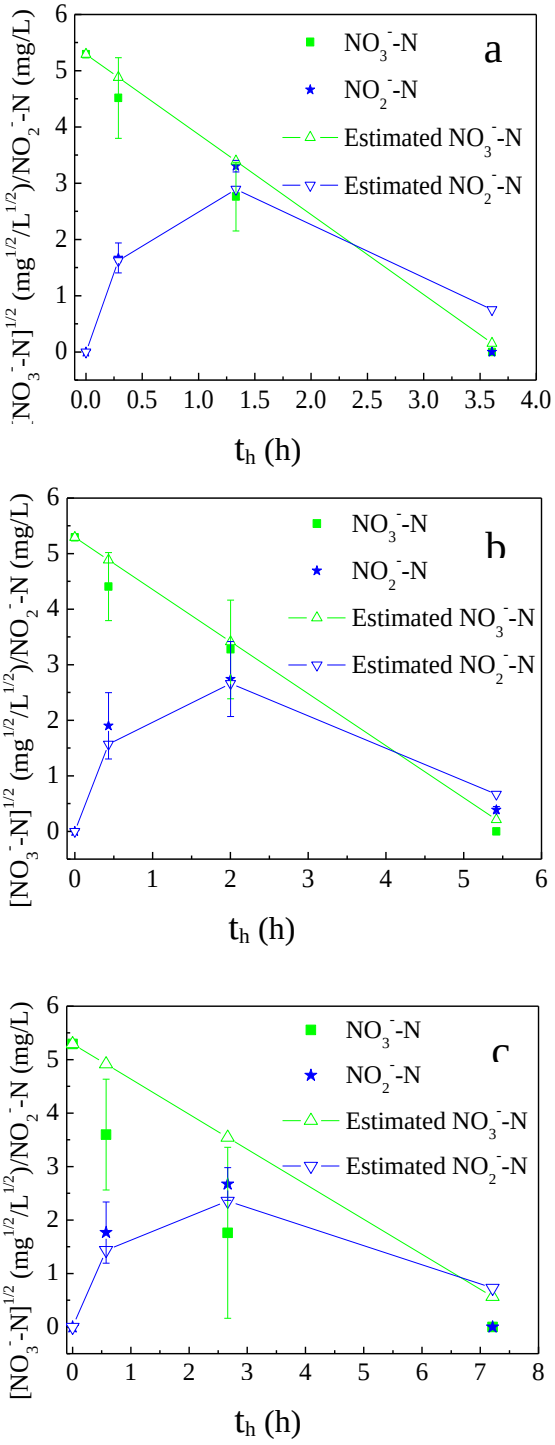

Figure 7.3: $[NO_3^-N]^{1/2}$ / NO_2^-N vs. empty bed residence time at HRTs of 7.2 h (a), 5.4 h (b), and 3.6 h (c) in the nanostructured PADBs.

Based on the determined half-order reaction constants, the NO_3^-–N and NO_2^-–N concentrations along the nanostructured PADBs could be estimated with Eqs. 7. (4–5). However, the models fail to describe NO_2^-–N accumulation along the biofilters treating real secondary effluent during Phases 4–9. This may be explained by the low influent concentration of NO_3^-–N, which was only 13.81 ± 1.52 $mg \cdot L^{-1}$. Indeed, NO_3^-–N was mostly reduced in the lower part of the biofilters where the relative abundance of autotrophic denitrifying *Thiobacillus* was up to 87% in the bacterial community. Consequently, wastewater with low concentrations of N (average NO_3^-–N of 0.29 ± 0.07 $mg \cdot L^{-1}$ and NO_2^-–N of < 0.1 $mg \cdot L^{-1}$) passed through the middle of biofilters during Phases 4–6. During Phases 7–9, the reduction of NO_3^-–N followed first-order reaction kinetics in the biofilters, which is elucidated in Table 7.3. The low concentrations of NO_3^-–N can be explained by the increased mass transfer rates of NO_3^-–N at shorter HRTs.

Table 7.3: Reaction kinetics for NO_3^--N and NO_2^-–N at HRTs of 1.8 h, 1.2 h, 0.6 h in the nanostructured PADBs

Reaction kinetics	**First-order**		**Half-order reaction**	
Rate laws	$\frac{dC_{NO_3^--N}}{dt} = -k\, C_{NO_3^--N}$		$\frac{dC_{NO_2^--N}}{dt} = -k\, C_{NO_3^--N} - k_2 C_{NO_2^--N}^{1/2}$	
Equations	$C_{NO_3^--N,\ t} = C_{NO_3^--N,\ i}\ e^{-kt_h}$		$C_{NO_2^--N,\ t}^{1/2} = \frac{kC_{NO_3^--N,\ i}}{2k - k_2} e^{-\frac{k_2 t_h}{2}} + \frac{kC_{NO_3^--N,\ i}}{k_2 - 2k} e^{-kt_h}$	
Phase 7 (HRT: 1.8 h)	R^2	0.92		
	k	3.68	k_2	3.67
	p	0.04		
Phase 8 (HRT: 1.2 h)	R^2	0.97		
	k	7.37	k_2	7.95
	p	0.02		
Phase 9 (HRT: 0.6 h)	R^2	0.89		
	k	0.72	k_2	7.95
	p	0.05		

7.4.2 Phosphorus removal efficiency and mechanisms

Phosphorus removal efficiency of the nanostructured PADBs over the 536-day trial is presented in Fig. 7.1. The average effluent P concentration was as low as 0.02 $mg \cdot L^{-1}$ with almost 100% P removal at HRTs of 3.6–7.2 h (Fig. 7.1) when treating synthetic wastewater; the average effluent P concentration was as low as 0.03 $mg \cdot L^{-1}$ with an average P removal efficiency of 98% at a HRT of 0.6 h when treating real wastewater. The nanostructured PADB technology had significant advantages over sulfur–limestone autotrophic denitrification, which does not achieve P removal (Sahinkaya et al., 2014), as well as over conventional constructed wetlands (< 30% P removal) (Greenway, 2005), and other biological nutrient removal processes (71–97% P removal) (Liu et al., 2014b; Wu et al., 2014; Yin et al., 2015).

To test our hypothesis on the mechanisms of P removal, energy dispersive X–ray (EDX) mapping for element distribution (Fig. 7.4) and composition analysis (Table 7.4) was used to examine the secondary amorphous colloid formed on the surfaces of used NPyr particles. P element was abundant in the amorphous colloid (Fig. 7.4). Considering the low adsorption capacity of P on NPyr particles (0.17 $mg \cdot g^{-1}$ NPyr) (Chen et al., 2014b), the strong P signal observed confirms the hypothesis that P removal from wastewater was not achieved only by adsorption. Therefore, P adsorption on NPyr particles did not contribute significantly to the P removal achieved in the nanostructured PADBs. Oxygen and Fe were also found to be abundant in P–concentrated areas (Fig. 7.4). Iron would appear as Fe^{3+} resulting from microbial oxidation of NPyr by *Thiobacillus*, which can also use Fe^{2+} as an electron donor with NO_3^-–N reduction (Bosch et al., 2012). Low total Fe concentrations of 0.84 ± 0.67 $mg \cdot L^{-1}$ (Fe^{2+}< the detection limit of 0.02 $mg \cdot L^{-1}$) were detected in the effluent (Table 7.6), indicating that Fe^{3+} was precipitated in the biofilters. Fe^{3+} precipitation was due to formation of $FePO_4$ (s) and $Fe(OH)_3$ (s) in the secondary colloid. The atomic ratio of Fe:P:O in the secondary colloid was 1.39:1:4.83 (Table 7.4), which is close to 1:1:4. Based on the atomic percentage of P in the secondary colloid, and considering that P adsorption was negligible compared with P precipitation, the secondary colloid can be inferred to be primarily composed of $FePO_4$ (71

mol%). The excessive amount of Fe and O was due to the precipitation of $Fe(OH)_3$. On the basis of TEM-EDX data, our hypothesis that the precipitation of $FePO_4$ was the dominant mechanism for P removal in nanostructured PADB was confirmed. The $FePO_4$ precipitates on the NPyr particles' surface could result in clogging of the biofilters over a long-term operation. Therefore, downflow nanostructured PADBs are suggested to lessen the chance of clogging for practical biofilter operation: the secondary effluent to be treated is applied from the top of the biofilters and withdrawn at the bottom. Once the clogging occurred, the top NPyr particles can be replaced with fresh NPyr particles.

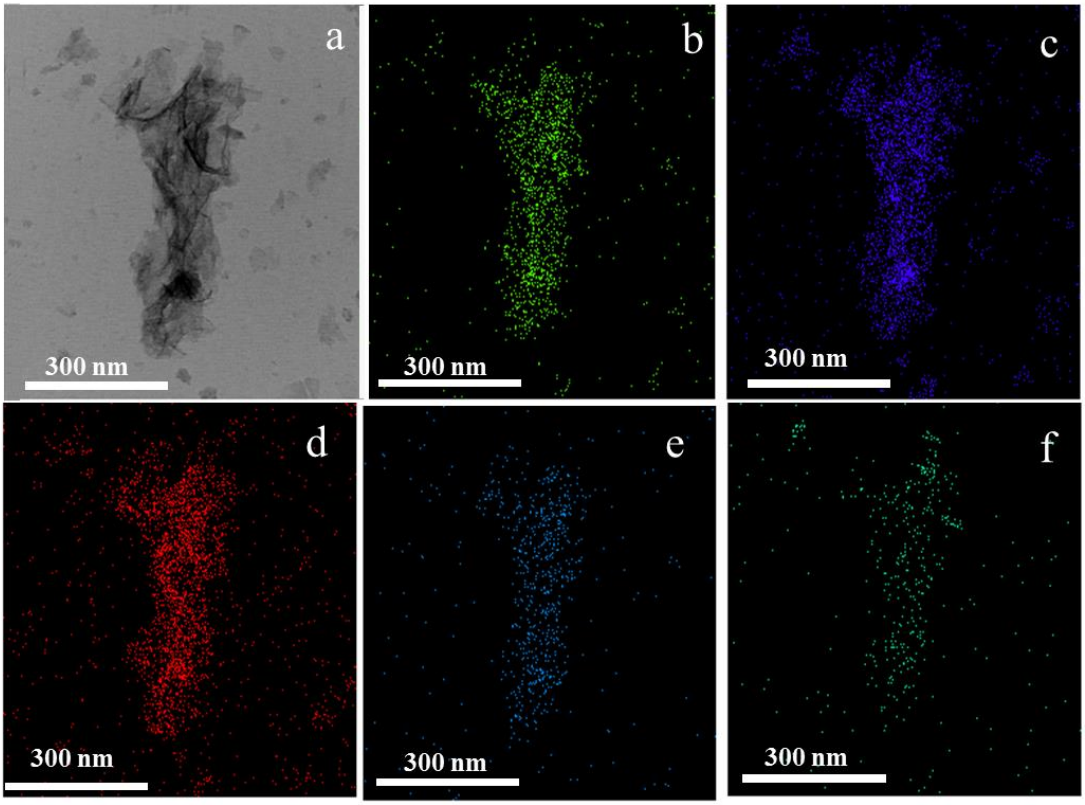

Figure 7.4: TEM micrograph (a) and energy dispersive X–ray (EDX) mapping for different elements: phosphorus (b), iron (c), oxygen (d), calcium (e), and sulfur (f) of the secondary colloid in the used NPyr particles.

Table 7.4: Atomic percentages (%) of elements in the secondary colloid formed on the used NPyr particles

Element	Fe	P	O	Ca	S	Si
Atomic (%)	17.28	12.43	60.07	5.93	2.03	1.69

7.4.3 Conversion of sulfur in PADBs

According to pyrrhotite based autotrophic denitrification, 3.84 mg of SO_4^{2-} is produced stoichiometrically when 1 mg NO_3^-–N is reduced to N_2. Thus, PADB effluent SO_4^{2-} concentrations should be higher than influent SO_4^{2-} concentrations. The difference between the concentrations of effluent SO_4^{2-} and influent SO_4^{2-}, $\Delta\ SO_4^{2-}$, is defined as follows:

$$\Delta\ SO_4^{2-} = SO_4^{2-}{}_{effluent} - SO_4^{2-}{}_{influent} \quad (7.5)$$

The $\Delta\ SO_4^{2-}$ values during the nine operational phases of the trial are shown in Table 7.6. During Phases 1–3 when the biofilters were used to treat the synthetic wastewater containing 28 mg NO_3^-–N·L^{-1}, $\Delta\ SO_4^{2-}$ was 135.10 ± 33.10 mg·L^{-1}, which was higher than the $\Delta\ SO_4^{2-}$ value of 106.7 mg·L^{-1} calculated theoretically. The difference – 28.4 mg·L^{-1} (135.10 - 106.7 mg·L^{-1}) – was due to NPyr oxidation by the small amount of oxygen inevitably introduced with the influent (Annachhatre & Suktrakoolvait, 2001; Bosch et al., 2012). Nonetheless, the effluent SO_4^{2-} was < 250 mg·L^{-1}, which is the maximum level set by the US EPA for Secondary Drinking Water Standards (Sahinkaya et al., 2011a).

An interesting phenomenon was observed in the nanostructured PADB treating real secondary effluent at low HRTs of 0.6–3.6 h during Phases 4–9: Δ SO_4^{2-} was mostly negative with up to -21.77 mg·L^{-1}, which is considerably lower than the theoretical value of 52.61 ± 0.34 mg·L^{-1} (Table 7.5) i.e. the effluent SO_4^{2-} concentrations were lower than the influent SO_4^{2-} concentration. SO_4^{2-} concentrations along the biofilters are shown in Fig. 7.5. SO_4^{2-} accumulation (Δ SO_4^{2-} of near 52.61 mg·L^{-1}) observed in the middle of the biofilters, confirmed that autotrophic denitrification oxidizing S^{2-} in NPyr to SO_4^{2-} was a dominant process in the lower part of the biofilters. The consumption of 56.07, 58.01, 50.09 and 32.50 mg SO_4^{2-}·L^{-1} (the difference between SO_4^{2-} concentrations at the middle and top sampling points) in the upper section of the biofilters indicates that SO_4^{2-} reduction did occur.

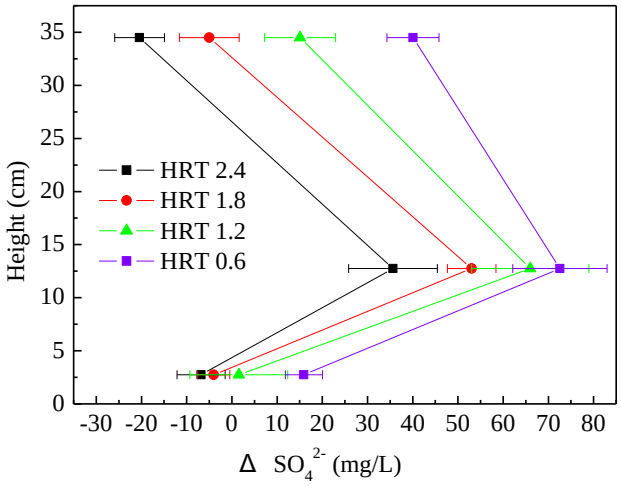

Figure 7.5: Δ SO_4^{2-} along the nanostructured PADBs.

XPS spectra of S determined that the intermediate S species between SO_4^{2-} and S^{2-} were on the used NPyr particles (Fig. 7.6). The dominant peaks in all S (2p) spectra (Fig. 7.5 a–c) are located at 161.2 ± 0.2 eV and 162.3 ± 0.2 eV, corresponding to the S(2p3/2) peak for monosulfide (S^{2-}) in iron sulfides (Mullet et al., 2002) and an approximate oxidation state of S^{-}

on $Fe_{1-x}S$ (Behra et al., 2001), respectively. Two extra peaks at higher binding energies were observed for the used NPyr particles taken from the bottom (Fig. 7.6 b) and middle (Fig. 7.6 c) of the biofilters: peaks at 168.3 eV correspond to binding energies for SO_4^{2-} species (Renock et al., 2009), one end-product of NPyr-based denitrification; peaks at 163.4 ± 0.1 eV correspond to polysulfides (S_n^{2-}, n=2, 3, ……, 9) (Mullet et al., 2002; Renock et al., 2009), which may be intermediate products of SO_4^{2-} reduction (Eq. 7.6). SO_4^{2-} reduction can result in different S species, such as thiosulfate ($S_2O_3^{2-}$), polysulfides (S_n^{2-}), and elemental sulfur (S). Only S_n^{2-} was detected by XPS in this study. Sulfate-reducing bacteria (SRB, i.e. *Desulfosporosinus sp.*, *Desulfobulbus sp.*, and *Desulfitobacterium sp.)* were accounted for 0.12% of the relative abundance of 16S rRNA gene sequences from the samples collected from the middle part of biofilters when treating real secondary effluent. Other researchers have also found that SRB are very active bacteria and are able to perform significant SO_4^{2-} reduction at a range of 1.5-16.7 $mg \cdot L^{-1}_{peat\ soil} \cdot day^{-1}$ at a low genome abundance of less than 0.1% (Hausmann et al., 2016). Hence, when treating the real wastewater, the presence of SRB probably contributed to SO_4^{2-} reduction, which is as described by Eq. 7.7

$$\mathbf{S_{SO4}^{6+} \rightarrow S_{SO3}^{4+} \rightarrow S_{S3O6}^{3.3+} \rightarrow S_{S4O6}^{2.5+} \rightarrow S_{S2O3}^{2+} \rightarrow S^{0} \rightarrow S_{n}^{2-}} \quad \textbf{(7.6)}$$

$$\mathbf{CH_2O + SO_4^{2-} \rightarrow S_n^{2-} + HCO_3^-} \quad \textbf{(7.7)}$$

Organic matter (represented by CH_2O, Eq. 7.7) in the nanostructured PADBs included residual organic contaminants in the real secondary treated wastewater, in which the COD concentration was 22.5 ± 2.1 $mg \cdot L^{-1}$ (Table 7.1).

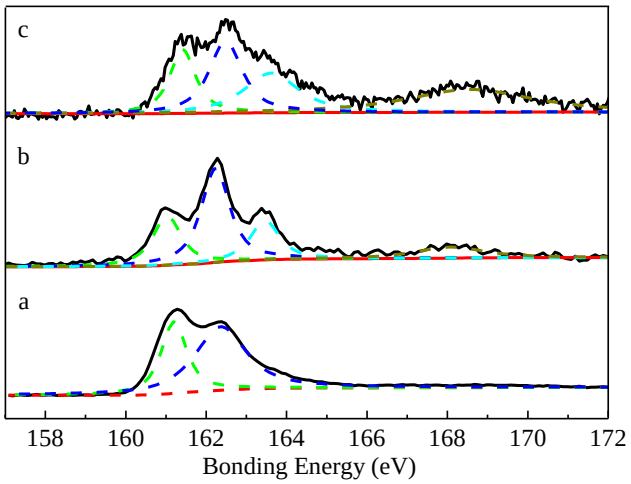

Figure 7.6: XPS spectra of S (2p) peak for NPyr

(a: original NPyr; b: the used NPyr collected from the bottom of the biofilters; c: the used NPyr collected from the middle of the biofilters; background (Red dash); Fe^{2+} –S^{2-} (green dash), S^{-} (blue dash), S_n^{2-} (cyan dash), SO_4^{2-} (Tan dash); the solid line represents the sum of the component peaks)

Hence, a reversible sulfur cycle is proposed for the nanostructured PADBs (Fig. 7.7): NPyr ($Fe_{1-x}S$) was utilised as the electron donor for autotrophic denitrifiers resulting in microbial oxidation of S^{2-} to SO_4^{2-} (blue box, Fig. 7.7); the produced SO_4^{2-} was then used as the electron acceptor by heterotrophic SRB leading to SO_4^{2-} reduction to S_n^{2-} (Eq. 7.7; green box, Fig. 7.7). S_n^{2-} in the biofilters can then be used as the electron donor for autotrophic denitrifiers to reduce NO_3^- again. This cycle underpins the potentially sustainable use of NPyr as a sulfur source for autotrophic denitrification in nanostructured PADB technology.

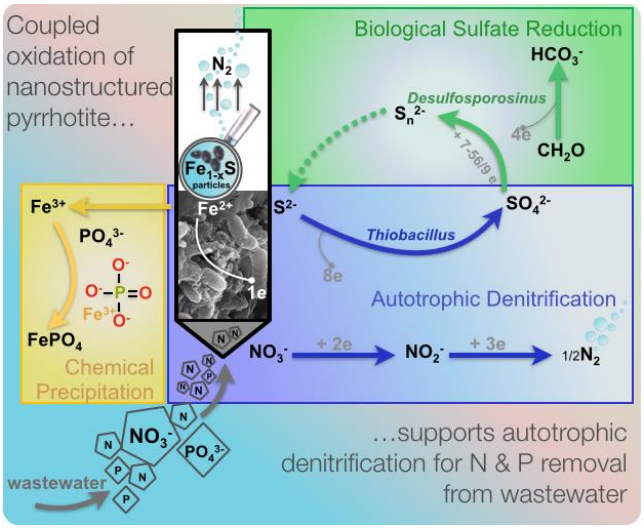

Figure 7.7: Proposed pathway for NPyr autotrophic denitrification coupled microbial oxidation for simultaneous N and P removal in the nanostructured PADBs.

Protons are also generated in the NPyr-based autotrophic denitrification process. According to the stoichiometric equation, 0.39 mg $CaCO_3$ alkalinity is consumed when 1.00 mg NO_3^-– N is reduced. The pH decreased from 8.30 ± 0.07 in the influent to 7.69 ± 0.37 in the effluent during Phases 1-3 in the nanostructured PADB treating synthetic wastewater (Table 7.5). However, the effluent pH increased slightly when the biofilters treating real secondary wastewater during Phases 4–8. This may be due to production of HCO_3^- during biological SO_4^{2-} reduction by SRB (Eq. 7.7). In general, variations in pH were insignificant in the nanostructured PADBs, particularly when compared with the H^+ production during elemental-sulfur-based autotrophic denitrification, which would consume 4.57 mg $CaCO_3$ alkalinity to reduce 1.00 mg NO_3^-–N (Sahinkaya et al., 2014). Hence, NPyr–based autotrophic denitrification is a pH-buffering process.

Table 7.5: Average pH and SO_4^{2-} concentrations in the effluent from the nanostructured PADBs

Phase	Influent pH	Influent SO_4^{2-} ($mg \cdot L^{-1}$)	Effluent pH	ΔSO_4^{2-} ($mg \cdot L^{-1}$)	Theoretical ΔSO_4^{2-} ($mg \cdot L^{-1}$)
1					
2	8.30±0.07	32.44±1.5	7.69 ± 0.37	135.10±33.10	106.68
3					
4			8.59 ± 0.11	-21.77 ± 29.22	
5			8.52± 0.13	-20.01 ± 22.96	
6			8.39 ± 0.27	-6.61 ± 15.23	
	7.34±0.44	115.25±0.15			52.61 ± 0.34
7			8.34 ± 0.05	-4.13 ± 8.14	
8			8.16 ± 0.01	14.87 ± 5.50	
9			8.10 ± 0.13	35.51 ± 4.57	

Therefore, the issues of SO_4^{2-} production and pH reduction that are usually associated with elemental-sulfur-based autotrophic denitrification were avoided (Table 7.6), confirming the advantages of NPyr as a sulfur source for autotrophic denitrification for wastewater treatment. In addition, the potential risks of metals leaching following iron sulfide oxidation were assessed during each of the operational phases (Table 7.6). The concentrations of trace metals, such as Cu, Zn, Pb, Cd, and As were negligible in the effluent, which were much lower than the Maximum Contaminant or Treatment Technique Level in drinking water (1300 $\mu g \cdot L^{-1}$ for

Cu, 15 $\mu g \cdot L^{-1}$ for Pb, 5 $\mu g \cdot L^{-1}$ for Cd, and 10 $\mu g \cdot L^{-1}$ for As, etc) (EPA, 2016). The results indicated that there was little leaching of priority metal pollutants from the nanostructured PADB, which is advantageous with respect to environmental protection.

Table 7.6: Average metal concentrations in the effluent from the nanostructured PADBs

Phase	Cu ($\mu g \cdot L^{-1}$)	Zn ($\mu g \cdot L^{-1}$)	Pb ($\mu g \cdot L^{-1}$)	Cd ($\mu g \cdot L^{-1}$)	As ($\mu g \cdot L^{-1}$)	Fe ($mg \cdot L^{-1}$)	Ca ($mg \cdot L^{-1}$)
1	8.86±7.03	5.95±5.01	0.06±0.12	0.03±0.10	0.41±0.46	1.02±0.68	43.91±14.76
2	1.07±0.01	3.04±1.17	0.01±0.01	0.02±0.01	0.16±0.02	0.80±0.55	40.87±1.28
3	2.59±1.73	2.89±2.28	0.02±0.01	0.02±0.01	0.23±0.025	0.27±0.31	40.04±12.45
4	6.47±1.59	1.51±1.20	0.03±0.01	0.04±0.04	1.16±0.84	0.06±0.02	38.49±7.72
5	9.27±1.09	1.54±0.05	0.03±0.01	0.02±0.01	1.20±0.31	0.12±0.12	44.08±1.64
5	14.49±1.09	1.51±0.05	0.03±0.01	0.01±0.01	0.98±0.31	0.22±0.12	45.25±1.64
7	10.03±0.07	1.11±0.11	0.05±0.01	0.02±0.01	1.75±0.01	1.51±0.99	68.04±1.76
8	11.46±0.19	0.98±0.14	0.05±0.01	0.02±0.01	1.08±0.01	2.19±0.08	64.0±1.28
9	9.78±0.06	1.35±0.14	0.03±0.01	0.01±0.01	1.5±0.01	0.02±0.14	51.63±1.86

7.5 Summary

This chapter evaluated the potential of using NPyr as the biofilm substratum in PADBs for autotrophic denitrification reducing NO_3^- to N_2. Meanwhile, P was mainly removed via chemical precipitation as iron phosphates. The experiment demonstrates that NPyr is an

efficient electron donor for *Thiobacillus* in nanostructured PADBs. A considerable amount of SO_4^{2-} was reduced in the upper section of the nanostructured PADBs. The closed loop of sulfur suggests the sustainability of NPyr as the sulfur source for autotrophic denitrifiers. Efficient denitrification and PO_4^{3-}–P removal were achieved in the 536-day trial, which demonstrated the durability and long-term capacity of nanostructured PADBs in reducing NO_3^- and removing PO_4^{3-}–P. High quality and low effluent concentrations of N (0.05 $mg \cdot L^{-1}$) and P (0.03 $mg \cdot L^{-1}$) were achieved at a short HRT of 1.2 h when treatment of real secondary effluent. The overall results indicate that the feasibility of applying nanostructured PADB as a potential tertiary treatment to meet stringent discharge standards.

Chapter 8

Conclusions

8.1 Overview

This Ph.D. research is to investigate the efficiencies and mechanisms of natural and synthesized nanostructured iron sulfides (i.e. nano-sized colloidal pyrite and nanostructured pyrrhotite–NPyr) for the removal of metals and nutrients from wastewater. As sorbents, nano-sized colloidal pyrite or NPyr were added in fixed-bed columns, and the capacities and mechanisms of Cu sorption from synthetic and real acid mine drainage (AMD) were tested. As biofilm substratum, NPyr was added in biofilters forming nanostructured pyrrhotite autotrophic denitrification biofilters (PADBs), and its efficiency in removal of N and P from synthetic and real secondary treated wastewater was assessed.

8.2 Main Conclusions

8.2.1 Immobilization of Cu using CPWR

1) CPWR were efficient in the removal of Cu from low–concentration (10 $mg \cdot L^{-1}$) Cu solution with a breakthrough capacity of 14.0 mg $Cu \cdot g^{-1}$ CPWR.

2) The contents of Cu and Fe in the used CPWR were up to 1.5% and 47.8%., respectively.

3) Sequential extraction of Cu, analysis of Fe oxides/hydroxides, and SEM–EDX analysis of the used CPWR indicate that 45–52% of Cu^{2+} was removed due to the adsorption of Cu on iron hydroxides formed via the oxidation of colloidal pyrite and dissolution of siderite in the CPWR.

8.2.2 Removal and recovery of metals by NPyr

1) The breakthrough capacities for the four single-metal (i.e. Cu, Pb, Cd, or Zn) solutions were 77.42 mg $Cu \cdot g^{-1}$, 73.68 mg $Pb \cdot g^{-1}$, 8.42 mg $Cd \cdot g^{-1}$, and 58.74 mg $Zn \cdot g^{-1}$, respectively.

After the breakthrough, the contents of Cu, Pb, Cd, and Zn in the used NPyr particles were up to 17.41%, 15.37%, 3.97%, and 8.9%, respectively.

2) The breakthrough capacities of Cu, Pb, Cd, and Zn for the multi-metal Cu–Pb–Cd–Zn solution were 30.79, 10.86, 9.78, and 0 $mg \cdot g^{-1}$, respectively. After the breakthrough, the maximum Cu and Pb contents in the used NPyr sorbent were up to 6.80% and 2.50%, respectively.
3) XRD analysis and sequential extractions of Cu and Pb in the used NPyr particles indicated that most Cu and Pb (nearly 99%) was removed by the precipitation of covellite and galena.

8.2.3 Cu removal in real AMD by NPyr

1) Batch experiments show that Cu removal efficiency was high at an initial pH of 2, was the lowest at an initial pH of 3, and then it was high again in the pH range of 4–6.
2) A two-column reactor system (Column A, with limestone added as neutralizer; Column B, with NPyr added as sorbent) had a breakthrough capacity of 21.93 mg $Cu \cdot g^{-1}$ NPyr when treating AMD containing 43.16 mg $Cu \cdot L^{-1}$ at a pH of 2.8.
3) The elevated Cu contents in the used NPyr particles were nearly 9.23% at the bottom, which mainly existed as CuS on NPyr's surface.
4) The dissolved Fe^{3+} and SO_4^{2-} in the AMD led to precipitation of iron oxyhydroxide coatings and gypsum on the NPyr's surface.

8.2.4 Enrichment of sulfur-based autotrophic denitrifiers

1) Successful enrichment of sulfur-based autotrophic denitrifiers from anaerobic sludge was achieved after 28 days at 30°C under anaerobic conditions.
2) TRFLP and high-throughput Illumina sequencing of 16S rRNA genes indicated a significant reduction in the bacterial diversity along the enrichment. Illumina sequencing

showed that *Thiobacillus* became the dominant genus with a relative abundance of 55% in the final enrichment culture.

3) The specific utilization rate of nitrate was 16.40 mg NO_3^--N·(g·VSS·d)$^{-1}$ for the final enrichment culture.

8.2.5 N and P removals by nanostructured PADBs

1) The experiment demonstrates the durability and long-term capacity of nanostructured PADBs to further reduce N and P to low levels to meet stringent effluent quality criteria. Low effluent concentrations of N (0.05 mg·L^{-1}) and P (0.03 mg·L^{-1}) at a short HRT of 1.2 h were achieved over the 536-day trial.
2) A two-step denitrification process ($NO_3^- \rightarrow NO_2^- \rightarrow N_2$) in nanostructured PADB was proposed to simulate the denitrification kinetics.
3) P was mainly removed by chemical precipitation as $FePO_4$.
4) The reduction of SO_4^{2-} to S_n^{2-} with 32.50–58.01 mg SO_4^{2-}·L^{-1} occurred in nanostructured PADBs when treating real secondary treated wastewater, highlighting the sustainability of NPyr as sulfur sources for autotrophic denitrifiers.

8.2.6 Summary

This study provides a better insight into the role of CPWR in the weathering and leaching processes and their function with metals in AMD. The availability of the natural CPWR at a low cost makes it a promising material for in situ remediation of Cu–contaminated AMD. However, the cubic crystal structure of colloidal pyrite limits its breakthrough capacity to be only 14.0 mg Cu·g^{-1} CPWR. Therefore, reactive NPyr was used in latter research. The breakthrough capacity was increased by almost six times to 77.42 mg Cu·g^{-1} when treating synthetic Cu wastewater in fixed-bed columns added with NPyr. Low effluent concentrations

of N (0.05 $mg \cdot L^{-1}$) and P (0.03 $mg \cdot L^{-1}$) at a short HRT of 1.2 h were achieved over the 536-day trial in nanostructured PADBs where NPyr used as biofilm substratum.

This research shows the potential of synthesized NPyr as i) a novel cost-effective sorbent for Cu removal and recovery from real AMD, and ii) biofilm substratum for autotrophic denitrification in nanostructured PADB technology as tertiary treatment for wastewater in lab-scale column reactors.

8.3 Recommendations for future research

It is suggested that the application of NPyr into metal and nutrient removals from wastewater should be "scaled-up" in the field to test against a set of wastewater quality parameters in real conditions.

The lab-scale two-column (Limestone Column and NPyr Column) study shows that 50 g of limestone/NPyr removed 1185 mg Cu from the AMD. Currently, the cost of raw pyrite is €60-180 per tonne (t) (Yang et al., 2016), the price of raw limestone €2-6/t (Rau et al., 2007), and the price of Cu is €4819-8433/t (Stephen et al., 2012). Therefore, recovery of Cu by this technology has both economical and environmental benefits. The average Cu content in the used NPyr particles was 2.37%, considerably higher than natural Cu ores (0.3–0.6%). However, it's expected that Cu recovery from the used NPyr particles with extractive metallurgy would be expensive. Downstream costs (treatment charge / refining charge) are 23% of the Cu price, on average (Barr et al., 2005). An onsite refinery, processing the copper concentrates to metal on site, would generate a ≈20% internal rate of return for a typical mid-sized mine (Barr et al., 2005). Therefore, an on-site refinery rather than selling the concentrate to remote smelters would have substantial advantages if the scale is reasonable.

As discussed in Chapter 7, the effluent TON and PO_4^{3-}-P concentrations were below 0.05 $mg{\cdot}L^{-1}$ and 0.03 $mg{\cdot}L^{-1}$, respectively when secondary effluent was treated by nanostructured PADBs at a HRT of 1.2 h. The nanostructured PADBs added with 50 g of NPyr particles had a theoretical NO_3^- reduction capacity of 286 g NO_3^-–N kg^{-1} NPyr based on Eq. 2.16. Therefore, for the treated secondary effluent containing 28 mg NO_3^-–N/L and 6 mg PO_4^{3-}–P/L, the nanostructured PADBs can treat 510 L of wastewater theoretically. However, only 97.2 L of wastewater was treated over the 536-day trial, indicating four fifths of the NPyr particles were still unused. This implies that the service time of the biofilters could be 7.3 years at this HRT. The reduction of SO_4^{2-} to reduced sulfur compounds would extend the service time of the biofilters by providing more sulfur to autotrophic denitrifiers. However, the service life of PADBs needs to be investigated with pilot-scale trials since P precipitation would adversely impact NO_3^- reduction performance and cause the clogging of the biofilters.

The electricity cost of manufacturing NPyr from pyrite (horizontal tube furnace, 4000 W; for 1 h) is € 2.23/t at an electricity price of € 0.56/KW·h, which is negligible compared with the pyrite cost. The cost of NPyr consumed to treat wastewater in the PADB is estimated to be less than € 0.017/m^3 wastewater. For conventional heterotrophic denitrification process, in order to efficiently remove NO_3^- from wastewater by adding external carbon sources, the cost of wastewater treated is about $ 0.19/m^3 (Li et al., 2016), needless to say additional cost of chemical precipitation for further P removal. Hence, the operation cost of nanostructured PADB technology should be much lower, and it is a simple, efficient and cost-effective method for simultaneous removal of N and P for WWTPs. Further pilot-scale research should be carried out to assess the costs in more details.

The average hydraulic loading rate in a treatment plant treating municipal wastewater varies, ranging from 150 to 250 L/PE/d (Tchobanoglous et al., 2004). 200 L/PE/d is selected to estimate the size of the PADB biofilters. Assume the treatment capacity is 10,000 PE (a small town), and the volume of the PADB can be calculated with Eq. 8.1

$$\mathbf{Q\ C_0\ t_H = V_3\ q} \qquad \textbf{(8.1)}$$

where Q is the daily flow of wastewater to be treated (m^3/h), 83.3 m^3/h (2,000,000 L/d);

C_0 is the influent concentration of nitrogen; 15 mg NO_3^-–N/L is used in the calculation based on the current EU Water Framework Directive regulations on a discharge limit for N in secondary effluent;

t_H is the desired hydraulic retention time, i.e. 1.2 h; q is the theoretical NO_3^- reduction capacity, i.e. NPyr, 286 g NO_3^-–N kg_{NPyr}^{-1}

The volume of NPyr added (V_3) is calculated to be 232.4 m^3 for the treatment of 2000 m^3/d secondary effluent.

As discussed in Chapters 4-5, the recovery of metals in the used NPyr by direct metallurgical extraction is feasible (the green arrows, Fig. 8.1). Otherwise, the used iron sulfides could be deposited of as wastes and lead to AMD which is described in Chapter 1 (the yellow arrows, Fig. 8.1).

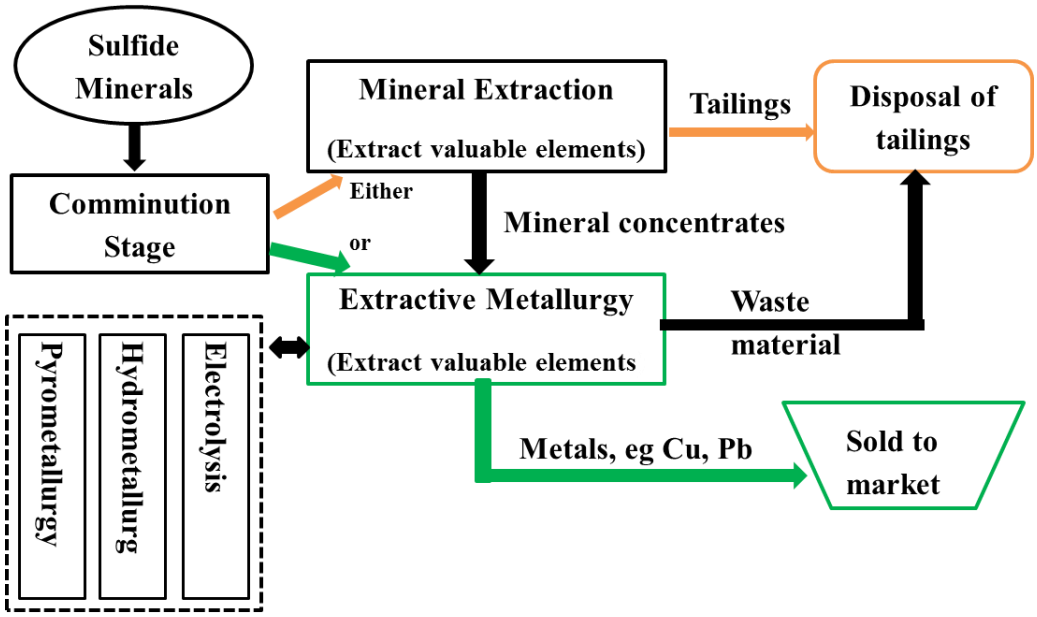

Figure 8.1: Flow sheet of the process for the disposal of iron sulfide minerals

The process used for metallurgical extraction can be hydrometallurgy, pyrometallurgy, or electrometallurgy. Hydrometallurgy is a classical process to recover metals, but it is easily inhibited in the presence of organic compounds and a pre-treatment step is required to remove organics; pyrometallurgy is able to recover metals with high controllability, but demands extremely high temperature (Barakat, 2011); electrometallurgy has the advantages of metal recovery without further sequential treatment, but has issues of intensive energy consumption and safe-handling of gas evolution (Chen et al., 2013a; Free et al., 2012). However, the detailed metallurgical extraction process to recover 17.41% of Cu/15.37% of Pb from the used NPyr particles (Chapter 4) needs more investigation. The recommended research contents include:

1) the extraction process and the conditions used to achieve high efficiency of metal recovery; for instance, extraction temperature if pyrometallurgy process is used;
2) the purity of the recovered metal either in its metallic state or as a chemical compound after extraction;

3) further studies on the applications of refined metals or their alloys.

During real AMD treated using the two-column reactor, the removal capacity was 21.93 mg $Cu \cdot g^{-1}$ NPyr (Chapter 5), and there is still a large scope for improvements. Following measures are recommended to improve:

1). increasing the hydraulic retention time, which would benefit crystallization of copper sulfide and a more complete reaction between metals and NPyr. Higher crystallization of metal sulfide (smaller crystal sizes) may preserve a large inter-space of crystals which precipitate on the outer layer of NPyr particles, thus increasing the diffusion rates of metal ions and S^{2-} when treating AMD by NPyr.

2). other alkaline neutralizers such as magnesium–aluminum oxide can be tested in Column A so as to avoid the precipitation of gypsum.

3). dissolved oxygen in the influent should be removed, such as adding Na_2SO_3 as deoxidizer, to avoid the precipitation of Fe oxyhydroxides which can immobilize Cu, leading to the incomplete separation of Cu and Fe.

For NPyr-based PADB technology, further studies can be conducted on i) model development, and evaluation of kinetic parameters of the biological autotrophic denitrification biofilm, ii) the emission of N_2O, and iii) pilot-scale demonstration. The recommended research contents include:

1). model development: Main processes and components with parameters for NPyr-based autotrophic denitrification process are to be established to describe the sulfide bio-oxidation and nitrite reduction processes.

2). evaluation of kinetic parameters (such as electron distribution coefficient of S^{2-} oxidation for NO_3^-–N which initially reduced to NO_2^-–N, and then reduced to N_2) on biological denitrification and sulfide oxidation.

3). as nanostructured PADB is a biofilm technology, the growth and detachment of biofilms and mass transfer kinetics need to be investigated.

4). dissolved N_2O was not detectable during NPyr-based autotrophic denitrification processes in nanostructured PADBs when treating NO_3^-–N concentrations of < 28 $mg \cdot L^{-1}$. However, the impact such as the concentration ratios of NO_3^-–N to $Fe_{1-x}S$ on N_2O emission should be further studied.

5). pertinent design for full-scale application of nanostructured PADBs is necessary to assay the long term stability in treatment efficiency and microbial community structure under various wastewater characteristics and temperature.

Bibliography

Alam, M., Roy, C., Pyne, P., Agarwal, A., George, A., Ghosh, W. 2012. Whole-genome shotgun sequence of the sulfur-oxidizing chemoautotroph Pseudaminobacter salicylatoxidans KCT001. *Journal of Bacteriology*, **194**, 4743-4744.

Ammar, S., Oturan, M.A., Labiadh, L., Guersalli, A., Abdelhedi, R., Oturan, N., Brillas, E. 2015. Degradation of tyrosol by a novel electro-Fenton process using pyrite as heterogeneous source of iron catalyst. *Water research*, **74**, 77-87.

Annachhatre, a.P., Suktrakoolvait, S. 2001. Biological sulfide oxidation in a fluidized bed reactor. *Environmental technology*, **22**, 661-672.

APHA, AWWA, WEF. 1998. Standard Methods for the Examination of Water and Wastewater. *Standard Methods for the Examination of Water and Wastewater*, 1496.

ATSDR. 2015. The Priority List of Hazardous Substances, The Agency for Toxic Substances and Disease Registry. United States, pp. The Priority List of Hazardous Substances.

Ayres, R.U. 1997. Metals recycling: economic and environmental implications. *Resources, Conservation and Recycling*, **21**, 145–173.

Bae, S., Kim, D., Lee, W. 2013. Degradation of diclofenac by pyrite catalyzed Fenton oxidation. *Applied Catalysis B: Environmental*, **134-135**, 93-102.

Baken, S., Salaets, P., Desmet, N., Seuntjens, P., Vanlierde, E., Smolders, E. 2015. Oxidation of Iron Causes Removal of Phosphorus and Arsenic from Streamwater in Groundwater-Fed Lowland Catchments. *Environmental Science & Technology*, **49**(5), 2886–2894.

Barakat, M.A. 2011. New trends in removing heavy metals from industrial wastewater. *Arabian Journal of Chemistry*, **4**(4), 361-377.

Barr, G., Defreyne, J., Jones, D., Mean, R. 2005. On-site processing vs. sale of copper concentrates CESL.

Bebie, J., Schoonen, M.A.A., Fuhrmann, M., Strongin, D.R. 1998. Surface charge development on transition metal sulfides: An electrokinetic study. *Geochimica Et Cosmochimica Acta*, **62**(4), 633-642.

Behra, P., Bonnissel-Gissinger, P., Alnot, M., Revel, R., Ehrhardt, J.J. 2001. XPS and XAS Study of the Sorption of Hg(II) onto Pyrite. *Langmuir*, **17**, 3970-3979.

Belzile, N., Chen, Y.-W., Cai, M.-F., Li, Y. 2004. A review on pyrrhotite oxidation. *Journal of Geochemical Exploration*, **84**, 65-76.

Bi, Y., Hayes, K.F. 2014. Nano-FeS Inhibits UO_2 Reoxidation under Varied Oxic Conditions. *Environmental science & technology*, **48**, 632-40.

Bigham, J.M. 1994. Mineralogy of ochre deposits formed by sulfide oxidation. in: *Short Course Handbook on Environmental Geochemistry of Sulfide Mine-Wastes*, (Ed.) J.L. Jambor, Blowes, D.W. , Vol. 22, Mineralogical Association of Canada. Canada, pp. 103-132.

Bissey, L.L., Smith, J.L., Watts, R.J. 2006. Soil organic matter-hydrogen peroxide dynamics in the treatment of contaminated soils and groundwater using catalyzed H_2O_2 propagations (modified Fenton's reagent). *Water Res*, **40**(13), 2477-84.

Bonnissel-Gissinger, P., Alnot, M., Esehrardt, J.J., Behra, P. 2001. Aqueous Geochemical and Surface Science Investigation of the Effect of Phosphate on Pyrite Oxidation. *Environ. Sci. Technol.*, **35**, 2252-2257.

Borah, D., Senapati, K. 2006. Adsorption of Cd(II) from aqueous solution onto pyrite. *Fuel*, **85**(12-13), 1929-1934.

Bosch, J., Lee, K.Y., Jordan, G., Kim, K.W., Meckenstock, R.U. 2012. Anaerobic, nitrate-dependent oxidation of pyrite nanoparticles by Thiobacillus denitrificans. *Environmental science & technology*, **46**, 2095-101.

Bostick, B.C., Fendorf, M., Fendorf, S. 2000. Disulfide disproportionation and CdS formation upon cadmium sorption on FeS_2. *Geochimica et Cosmochimica Acta*, **64**, 247-255.

Bostick, B.C., Fendorf, S. 2003. Arsenite sorption on troilite (FeS) and pyrite (FeS_2). *Geochimica et Cosmochimica Acta*, **67**, 909-921.

Boursiquot, S., Mullet, M., Ehrhardt, J.J. 2002. XPS study of the reaction of chromium (VI) with mackinawite (FeS). *Surface and Interface Analysis*, **34**, 293-297.

Bower, J., Savage, K.S., Weinman, B., Barnett, M.O., Hamilton, W.P., Harper, W.F. 2008. Immobilization of mercury by pyrite (FeS2). *Environ Pollut*, **156**, 504-514.

Breynaert, E., Bruggeman, C., Maes, a. 2008. XANES-EXAFS analysis of se solid-phase reaction products formed upon contacting Se(IV) with FeS_2 and FeS. *Environmental Science and Technology*, **42**, 3595-3601.

Brown, J.R., Bancroft, G.M., Fyfe, W.S., McLean, R.a.N. 1979. Mercury removal from water by iron sulfide minerals. An electron spectroscopy for chemical analysis (ESCA) study. *Environmental Science & Technology*, **13**, 1142-1144.

Bruggeman, C., Maes, A., Vancluysen, J., Vandemussele, P. 2005. Selenite reduction in Boom clay: Effect of FeS(2), clay minerals and dissolved organic matter. *Environmental pollution (Barking, Essex : 1987)*, **137**, 209-21.

Bulut, G., Yenial, Ü., Emiroğlu, E., Sirkeci, A.A. 2013. Arsenic removal from aqueous solution using pyrite. *Journal of Cleaner Production*, 1-7.

Burgos, W.D., Borch, T., Troyer, L.D., Luan, F., Larson, L.N., Brown, J.F., Lambson, J., Shimizu, M. 2012. Schwertmannite and Fe oxides formed by biological low-pH Fe(II) oxidation versus abiotic neutralization: Impact on trace metal sequestration. *Geochimica et Cosmochimica Acta*, **76**, 29-44.

Butler, E.C., Hayes, K.F. 1997. Effects of solution composition on the reductive dechlorination of hexachloroethane by iron sulfide. **37**, 113-115.

Butler, E.C., Hayes, K.F. 1999. Trichloroethylene and Tetrachloroethylene by Iron Sulfide. *Environmental Science & Technology*, 2021-2027.

Caldeira, C.L., Ciminelli, V.S.T., Osseo-Asare, K. 2010. The role of carbonate ions in pyrite oxidation in aqueous systems. *Geochimica et Cosmochimica Acta*, **74**(6), 1777-1789.

Campos, J.L., Carvalho, S., Portela, R., Mosquera-Corral, a., Méndez, R. 2008. Kinetics of denitrification using sulphur compounds: effects of S/N ratio, endogenous and exogenous compounds. *Bioresource technology*, **99**, 1293-9.

Cao, L., Ni, Y., Wang, M., Ma, X. 2013. Magnetic Ni/α-Ni(OH)$_2$ porous superstructures: synthesis, influencing factors and applications in the removal of heavy metals. *RSC Advances*, **3**(11), 3585-3591.

Caporaso, J.G., Lauber, C.L., Walters, W.a., Berg-Lyons, D., Huntley, J., Fierer, N., Owens, S.M., Betley, J., Fraser, L., Bauer, M., Gormley, N., Gilbert, J.a., Smith, G., Knight, R. 2012. Ultra-high-throughput microbial community analysis on the Illumina HiSeq and MiSeq platforms. *The ISME Journal*, **6**, 1621-1624.

Cardoso, R.B., Sierra-alvarez, R., Rowlette, P., Field, J.A., Flores, E.R., Go, J. 2006. Sulfide Oxidation Under Chemolithoautotrophic Denitrifying Conditions. *Biotechnology and Bioengineering* **95**(6), 1148–1157.

Cerón, J.C., Grande, J.A., Torre, M.L., Santisteban, M., Valente, T. 2013. Impact of AMD processes on the water dams of the Iberian Pyrite Belt: overall hydrochemical characterization (Huelva, SW Spain). *Water, Air, & Soil Pollution*, **224**(8), 1642-1652.

Chandra, A.P., Gerson, A.R. 2010. The mechanisms of pyrite oxidation and leaching: A fundamental perspective. *Surface Science Reports*, **65**, 293-315.

Chandra, A.P., Gerson, A.R. 2011. Redox potential (Eh) and anion effects of pyrite (FeS_2) leaching at pH 1. *Geochimica et Cosmochimica Acta*, **75**, 6893-6911.

Chandra, A.P., Puskar, L., Simpson, D.J., Gerson, A.R. 2012. Copper and xanthate adsorption onto pyrite surfaces: Implications for mineral separation through flotation. *International Journal of Mineral Processing*, **114-117**, 16-26.

Che, H., Bae, S., Lee, W. 2011. Degradation of trichloroethylene by Fenton reaction in pyrite suspension. *Journal of hazardous materials*, **185**, 1355-61.

Che, H., Lee, W. 2011. Selective redox degradation of chlorinated aliphatic compounds by Fenton reaction in pyrite suspension. *Chemosphere*, **82**, 1103-1108.

Chen, H., Zhang, Z., Yang, Z., Yang, Q., Li, B., Bai, Z. 2015. Heterogeneous fenton-like catalytic degradation of 2,4-dichlorophenoxyacetic acid in water with FeS. *Chemical Engineering Journal*, **273**, 481-489.

Chen, T.-C., Priambodo, R., Huang, R.-L., Huang, Y.-H. 2013a. The Effective Electrolytic Recovery of Dilute Copper from Industrial Wastewater. *Journal of Waste Management*, **2013**, 6.

Chen, T., Shi, Y., Liu, H., Chen, D., Li, P., Yang, Y., Zhu, X. 2016. A novel way to prepare pyrrhotite and its performance on removal of phosphate from aqueous solution. *Desalination and Water Treatment*, 1-9.

Chen, T., Yang, Y., Chen, D., Li, P., Shi, Y., Zhu, X. 2013b. Structural evolution of heat-treated colloidal pyrite under inert atmosphere and its application for the removal of Cu(II) ion from wastewater. *Environmental Engineering and Management Journal*, **12**, 1411-1416.

Chen, T., Yang, Y., Li, P., Liu, H., Xie, J., Xie, Q., Zhan, X. 2014a. Performance and characterization of calcined colloidal pyrite used for copper removal from aqueous solutions in a fixed bed column. *International Journal of Mineral Processing*, **130**, 82-87.

Chen, T.H., Wang, J.Z., Wang, J., Xie, J.J., Zhu, C.Z., Zhan, X.M. 2014b. Phosphorus removal from aqueous solutions containing low concentration of phosphate using pyrite calcinate sorbent. *International Journal of Environmental Science and Technology*, **12** (3), 885–892.

Chin, P.P., Ding, J., Yi, J.B., Liu, B.H. 2005. Synthesis of FeS_2 and FeS nanoparticles by high-energy mechanical milling and mechanochemical processing. *Journal of Alloys and Compounds*, **390**, 255-260.

Chiriţă, P., Descostes, M., Schlegel, M.L. 2008. Oxidation of FeS by oxygen-bearing acidic solutions. *Journal of colloid and interface science*, **321**, 84-95.

Chiriţă, P., Rimstidt, J.D. 2014. Pyrrhotite dissolution in acidic media. *Applied Geochemistry*, **41**, 1-10.

Chiriţă, P., Schlegel, M.L. 2015. Oxidative dissolution of iron monosulfide (FeS) in acidic conditions: The effect of solid pretreatment. *International Journal of Mineral Processing*, **135**, 57-64.

Choi, J., Choi, K., Lee, W. 2009. Effects of transition metal and sulfide on the reductive dechlorination of carbon tetrachloride and 1,1,1-trichloroethane by FeS. *Journal of hazardous materials*, **162**, 1151-8.

Choi, K., Bae, S., Lee, W. 2014a. Degradation of off-gas toluene in continuous pyrite Fenton system. *Journal of hazardous materials*, **280**, 31-7.

Choi, K., Bae, S., Lee, W. 2014b. Degradation of pyrene in cetylpyridinium chloride-aided soil washing wastewater by pyrite Fenton reaction. *Chemical Engineering Journal*, **249**, 34-41.

Clarke, K.R., R. M. Warwick. 1994. An Approach to statistical analysis and interpretation. *Change in marine communities*, **2**.

Courtin-Nomade, A., Bril, H., Neel, C., Lenain, J.-F. 2003. Arsenic in iron cements developed within tailings of a former metalliferous mine—Enguialès, Aveyron, France. *Applied Geochemistry* **18**(3), 395-408.

Couture, R.-M., Rose, J., Kumar, N., Mitchell, K., Wallschläger, D., Van Cappellen, P. 2013. Sorption of arsenite, arsenate, and thioarsenates to iron oxides and iron sulfides: a kinetic and spectroscopic investigation. *Environmental science & technology*, **47**, 5652-9.

Cui, J., Zhang, L. 2008. Metallurgical recovery of metals from electronic waste: a review. *J Hazard Mater*, **158**(2-3), 228-56.

Curti, E., Aimoz, L., Kitamura, A. 2013. Selenium uptake onto natural pyrite. *Journal of Radioanalytical and Nuclear Chemistry*, **295**, 1655-1665.

Darbi, A., Viraraghavan, T. 2003. A Kinetic Model for Autotrophic Denitrification using Sulphur:Limestone Reactors. *Water Quality Research Journal of Canada*, **38**(1), 183-192.

Demoisson, F., Mullet, M., Humbert, B. 2007. Investigation of pyrite oxidation by hexavalent chromium: solution species and surface chemistry. *J Colloid Interface Sci*, **316**, 531-540.

Descostes, M., Schlegel, M.L., Eglizaud, N., Descamps, F., Miserque, F., Simoni, E. 2010. Uptake of uranium and trace elements in pyrite (FeS_2) suspensions. *Geochimica et Cosmochimica Acta*, **74**, 1551-1562.

Donato, P.d., Mustin, C., Benoit, R., Erre, R. 1993. Spatial distribution of iron and sulphur species on the surface of pyrite. *Applied Surface Science*, **68**(1), 81-93.

Doyle, C.S., Kendelewicz, T., Bostick, B.C., Brown, G.E. 2004. Soft X-ray spectroscopic studies of the reaction of fractured pyrite surfaces with Cr(VI)-containing aqueous solutions. *Geochimica et Cosmochimica Acta*, **68**(21), 4287-4299.

Engates, K.E., Shipley, H.J. 2011. Adsorption of Pb, Cd, Cu, Zn, and Ni to titanium dioxide nanoparticles: effect of particle size, solid concentration, and exhaustion. *Environ Sci Pollut Res Int*, **18**(3), 386-95.

EPA, U. 2016. National primary drinking water regulations, (Ed.) E.P.A. US. Washington.

Equeenuddin, S.M. 2014. Occurrence of alpersite at Malanjkhand copper mine, India. *Environmental Earth Sciences*, **73**(7), 3849-3853.

Erdem, M., Ozverdi, A. 2006. Kinetics and thermodynamics of Cd(II) adsorption onto pyrite and synthetic iron sulphide. *Separation and Purification Technology*, **51**, 240-246.

Farquhar, M.L., Charnock, J.M., Livens, F.R., Vaughan, D.J. 2002. Mechanisms of arsenic uptake from aqueous solution by interaction with goethite, lepidocrocite, mackinawite, and pyrite: An X-ray absorption spectroscopy study. *Environmental Science and Technology*, **36**, 1757-1762.

Finck, N., Dardenne, K., Bosbach, D., Geckeis, H. 2012. Selenide retention by mackinawite. *Environmental science & technology*, **46**, 10004-11.

Free, M., Moats, M., Robinson, T., Neelameggham, N., Houlachi, G., Ginatta, M., Creber, D., Holywell, G. 2012. Electrometallurgy-Now and in the Future. *Electrometallurgy 2012-TMS 2012 Annual Meeting and Exhibition*.

Fu, F., Wang, Q. 2011. Removal of heavy metal ions from wastewaters: a review. *J Environ Manage*, **92**(3), 407-18.

Fujii, T., Yoshida, A., Tanaka, K., Marumo, F., Noda, Y. 1986. High pressure compressibilities of pyrite and cattierite. *Mineralogical Journal*, **13**, 202-211.

Futalan, C.M., Kan, C.-C., Dalida, M.L., Pascua, C., Wan, M.-W. 2011. Fixed-bed column studies on the removal of copper using chitosan immobilized on bentonite. *Carbohydrate Polymers*, **83**(2), 697-704.

Gallegos, T.J., Han, Y.-s., Hayes, K.F., Hayes, K.I.M.F. 2008. Model Predictions of Realgar Precipitation by Reaction of As (III) with Synthetic Mackinawite Under Anoxic

Conditions Model Predictions of Realgar Precipitation by Reaction of As (III) with Synthetic Mackinawite Under Anoxic Conditions. *Environmental Science & Technology*, **42**, 9338-9343.

Gallegos, T.J., Sung, P.H., Hayes, K.F. 2007. Spectroscopic investigation of the uptake of arsenite from solution by synthetic mackinawite. *Environmental Science and Technology*, **41**, 7781-7786.

Garrels, R., Thompson, M. 1960. Oxidation of pyrite by iron sulfate solutions. in: *American Journal of Science*, Vol. 258, pp. 57-67.

Ghosh, W., George, A., Agarwal, A., Raj, P., Alam, M., Pyne, P., Gupta, S.K.D. 2011. Whole-genome shotgun sequencing of the sulfur-oxidizing chemoautotroph Tetrathiobacter kashmirensis. *Journal of Bacteriology*, **193**, 5553-5554.

Gil-Lozano, C., Losa-Adams, E., Alfonso, F., Gago-Duport, L. 2014. Pyrite nanoparticles as a Fenton-like reagent for in situ remediation of organic pollutants. *Beilstein journal of nanotechnology*, **5**(1), 855-864.

Grande, J.A., Santisteban, M., de la Torre, M.L., Valente, T., Perez-Ostale, E. 2013. Characterisation of AMD pollution in the reservoirs of the Iberian Pyrite Belt. *Mine Water and the Environment*, **32**(4), 321-330.

Gray, N., Delaney, E. 2010. Measuring community response of bentic macroinvertebrates in an erosional river impacted by acid mine drainage by use of a simple model. *Ecological Indicators*, **10**(3), 668-675.

Gray, N.F., Delaney, E. 2008. Comparison of benthic macroinvertebrate indices for the assessment of the impact of acid mine drainage on an Irish river below an abandoned Cu-S mine. *Environ Pollut*, **155**(1), 31-40.

Greenway, M. 2005. The role of constructed wetlands in secondary effluent treatment and water reuse in subtropical and arid Australia. *Ecological Engineering*, **25**(5), 501-509.

Guo, H., Ren, Y., Liu, Q., Zhao, K., Li, Y. 2013. Enhancement of arsenic adsorption during mineral transformation from siderite to goethite: mechanism and application. *Environ Sci Technol*, **47**(2), 1009-16.

Ha, J.K., Cho, K.K., Kim, K.W., Kim, J.U., Kim, Y.Y. 2006. Structure and Electrochemical Properties of FeSx Nanoparticles Synthesized by Chemical Vapor Condensation Process. *Materials Science Forum*, **510-511**, 950-953.

Haaijer, S.C.M., Lamers, L.P.M., Smolders, A.J.P., Jetten, M.S.M., Camp, H.J.M.O.d. 2007. Iron sulfide and pyrite as potential electron donors for microbial nitrate reduction in freshwater wetlands. *Geomicrobiology Journal*, **24**(5), 391-401.

Han, D.S., Batchelor, B., Abdel-Wahab, A. 2012. Sorption of selenium(IV) and selenium(VI) onto synthetic pyrite (FeS2): spectroscopic and microscopic analyses. *J Colloid Interface Sci*, **368**(1), 496-504.

Han, D.S., Song, J.K., Batchelor, B., Abdel-Wahab, A. 2013. Removal of arsenite(As(III)) and arsenate(As(V)) by synthetic pyrite (FeS_2): synthesis, effect of contact time, and sorption/desorption envelopes. *Journal of colloid and interface science*, **392**, 311-8.

Han, R., Zou, W., Li, H., Li, Y., Shi, J. 2006. Copper(II) and lead(II) removal from aqueous solution in fixed-bed columns by manganese oxide coated zeolite. *J Hazard Mater*, **137**(2), 934-942.

Hausmann, B., Knorr, K.H., Schreck, K., Tringe, S.G., Glavina Del Rio, T., Loy, A., Pester, M. 2016. Consortia of low-abundance bacteria drive sulfate reduction-dependent degradation of fermentation products in peat soil microcosms. *ISME J*, **10**(10), 2365-75.

Hu, G., Dam-Johansen, K., Wedel, S., Hansen, J.P. 2006. Decomposition and oxidation of pyrite. *Progress in Energy and Combustion Science*, **32**(3), 295-314.

Hua, B., Deng, B. 2008. Reductive immobilization of uranium(VI) by amorphous iron sulfide. *Environmental Science and Technology*, **42**, 8703-8708.

Hughes, T.A., Gray, N.F., Sánchez Guillamón, O. 2013. Removal of Metals and Acidity from Acid Mine Drainage Using Liquid and Dried Digested Sewage Sludge and Cattle Slurry. *Mine Water and the Environment*, **32**(2), 108-120.

Huse, S.M., Welch, D.M., Morrison, H.G., Sogin, M.L. 2010. Ironing out the wrinkles in the rare biosphere through improved OTU clustering. *Environ Microbiol*, **12**(7), 1889-98.

Hyun, S.P., Davis, J.a., Sun, K., Hayes, K.F. 2012. Uranium(VI) reduction by iron(II) monosulfide mackinawite. *Environmental Science and Technology*, **46**, 3369-3376.

Jørgensen, C.J., Jacobsen, O.S., Elberling, B., Aamand, J. 2009. Microbial oxidation of pyrite coupled to nitrate reduction in anoxic groundwater sediment. *Environmental science & technology*, **43**, 4851-7.

James J. Kozich, S.L.W., Nielson T. Baxter, Sarah K. Highlander, Patrick D. Schlossa. 2013. Development of a Dual-Index Sequencing Strategy and Curation Pipeline for Analyzing Amplicon Sequence Data on the MiSeq Illumina Sequencing Platform. *Appl. Environ. Microbiol.*, **79**(17), 5112–5120.

Janzen, M.P., Nicholson, R.V., Scharer, J.M. 2000. Pyrrhotite reaction kinetics: Reaction rates for oxidation by oxygen, ferric iron, and for nonoxidative dissolution. *Geochimica et Cosmochimica Acta*, **64**, 1511-1522.

Jean, G.E., Bancroft, G.M. 1986. Heavy metal adsorption by sulphide mineral surfaces. **50**, 1455-1463.

Jeong, H.Y., Han, Y.-S., Park, S.W., Hayes, K.F. 2010a. Aerobic oxidation of mackinawite (FeS) and its environmental implication for arsenic mobilization. *Geochimica et Cosmochimica Acta*, **74**(11), 3182-3198.

Jeong, H.Y., Han, Y.S., Hayes, K. 2010b. X-ray absorption and X-ray photoelectron spectroscopic study of arsenic mobilization during mackinawite (FeS) oxidation. *Environmental Science and Technology*, **44**, 955-961.

Jeong, H.Y., Hayes, K.F. 2007. Reductive dechlorination of tetrachloroethylene and trichloroethylene by mackinawite (FeS) in the presence of metals: Reaction rates. *Environmental Science and Technology*, **41**, 6390-6396.

Jeong, H.Y., Klaue, B., Blum, J.D., Hayes, K.F. 2007. Sorption of mercuric ion by synthetic nanocrystalline mackinawite (FeS). *Environmental science & technology*, **41**, 7699-705.

Jeong, H.Y., Lee, J.H., Hayes, K.F. 2008. Characterization of synthetic nanocrystalline mackinawite: crystal structure, particle size, and specific surface area. *Geochimica et cosmochimica acta*, **72**, 493-505.

Jeong, H.Y., Sun, K., Hayes, K.F. 2010c. Microscopic and Spectroscopic Characterization of Hg(II) Immobilization by Mackinawite (FeS). *Environ. Sci. Technol.*, **44**, 7476-7483.

Kampschreur, M.J., Temmink, H., Kleerebezem, R., Jetten, M.S.M., van Loosdrecht, M.C.M. 2009. Nitrous oxide emission during wastewater treatment. *Water research*, **43**, 4093-103.

Kang, M., Chen, F., Wu, S., Yang, Y., Bruggeman, C., Charlet, L. 2011. Effect of pH on aqueous Se(IV) reduction by pyrite. *Environ Sci Technol*, **45**, 2704-2710.

Kantar, C., Ari, C., Keskin, S. 2015a. Comparison of different chelating agents to enhance reductive Cr(VI) removal by pyrite treatment procedure. *Water research*, **76**, 66-75.

Kantar, C., Ari, C., Keskin, S., Dogaroglu, Z.G., Karadeniz, A., Alten, A. 2015b. Cr(VI) removal from aqueous systems using pyrite as the reducing agent: batch, spectroscopic and column experiments. *Journal of contaminant hydrology*, **174**, 28-38.

Kelly, W.C., Turneaure, F.S. 1970. Mineralogy, paragenesis and geothermometry of the tin and tungsten deposits of the eastern Andes, Bolivia. *Economic Geology*, **65**(6), 609-680.

Kim, D.S. 2003. The removal by crab shell of mixed heavy metal ions in aqueous solution. *Bioresource Technology*, **87**, 355–357.

Kim, E.J., Murugesan, K., Kim, J.H., Tratnyek, P.G., Chang, Y.S. 2013. Remediation of Trichloroethylene by FeS-Coated Iron Nanoparticles in Simulated and Real Groundwater : E ff ects of Water Chemistry. *Ind. Eng. Chem. Res.*, **52**(27), 9343–9350.

Kirsch, R., Fellhauer, D., Altmaier, M., Neck, V., Rossberg, A., Fangh, T., Charlet, L., Scheinost, A.C. 2011. Oxidation State and Local Structure of Plutonium Reacted with Magnetite, Mackinawite, and Chukanovite. 7267-7274.

Koenig, A., Liu, L. 1997. Autotrophic denitrification of nitrified leachate in sulphur packed bed reactors. *Proceedings SARDINIA 1997 Sixth International Landfill Symposium S. Margherita di Pula*. Cagliari, Italy. pp. 283-292.

Koenig, A., Liu, L.H. 2001. Kinetic model of autotrophic denitrification in sulphur packed-bed reactors. *Water research*, **35**, 1969-78.

Labiadh, L., Oturan, M.A., Panizza, M., Hamadi, N.B., Ammar, S. 2015. Complete removal of AHPS synthetic dye from water using new electro-fenton oxidation catalyzed by natural pyrite as heterogeneous catalyst. *Journal of hazardous materials*, **297**, 34-41.

Lennie, a.R. 1995. Synthesis and Rietveld Crystal Structure Refinement of Mackinawite, Tetragonal FeS. *Mineralogical Magazine*, **59**, 677-683.

Li, J.P., Healy, M.G., Zhan, X.M., Rodgers, M. 2008. Nutrient removal from slaughterhouse wastewater in an intermittently aerated sequencing batch reactor. *Bioresource Technology*, **99**, 7644-7650.

Li, R., Hu, J.S., Sun, X.X., Zhang, X.M., Liu, Z., Zhan, X.M., Li, A.M. 2014a. Natural pyrrhotite biological filter and method for synchronously removing nitrate nitrogen and phosphorus out of water by using natural pyrrhotite biological filter. China.

Li, R., Kelly, C., Keegan, R., Xiao, L., Morrison, L., Zhan, X. 2013a. Phosphorus removal from wastewater using natural pyrrhotite. *Colloids and Surfaces A: Physicochemical and Engineering Aspects*, **427**, 13-18.

Li, R., Morrison, L., Collins, G., Li, A., Zhan, X. 2016. Simultaneous nitrate and phosphate removal from wastewater lacking organic matter through microbial oxidation of pyrrhotite coupled to nitrate reduction. *Water Research*, **96**, 32-41.

Li, R., Yuan, Y., Zhan, X., Liu, B. 2014b. Phosphorus removal in a sulfur-limestone autotrophic denitrification (SLAD) biofilter. *Environ Sci Pollut Res Int*, **21**(2), 972–978.

Li, R.H., Niu, J.M., Zhan, X.M., Liu, B. 2013b. Simultaneous removal of nitrogen and phosphorous from wastewater by means of FeS-based autotrophic denitrification. *Water Science and Technology*, **67** (12), 2761-2767.

Li, Y., Lu, A., Ding, H., Wang, X., Wang, C., Zeng, C., Yan, Y. 2010. Microbial fuel cells using natural pyrrhotite as the cathodic heterogeneous Fenton catalyst towards the degradation of biorefractory organics in landfill leachate. *Electrochemistry Communications*, **12**, 944-947.

Lin, Y.-T., Huang, C.-P. 2008. Reduction of chromium(VI) by pyrite in dilute aqueous solutions. *Separation and Purification Technology*, **63**, 191-199.

Liu, B., R.H., L., J.M., N., Yuan, Y.L. 2012. Nitrogen and phosphorus removal method by using pyrite as biochemical filling, Vol. CN101973629B. China.

Liu, H., Chen, T., Frost, R.L. 2014a. An overview of the role of goethite surfaces in the environment. *Chemosphere*, **103**, 1-11.

Liu, H., Zhu, M., Gao, S., Xia, S., Sun, L. 2014b. Enhancing denitrification phosphorus removal with a novel nutrient removal process: Role of configuration. *Chemical Engineering Journal*, **240**, 404-412.

Liu, J., Valsaraj, K.T., Devai, I., DeLaune, R.D. 2008. Immobilization of aqueous Hg(II) by mackinawite (FeS). *Journal of hazardous materials*, **157**, 432-40.

Liu, R., Yang, Z., He, Z., Wu, L., Hu, C., Wu, W., Qu, J. 2016. Treatment of strongly acidic wastewater with high arsenic concentrations by ferrous sulfide (FeS): Inhibitive effects of S(0)-enriched surfaces. *Chemical Engineering Journal*, **304**, 986-992.

Liu, Y., Mou, H., Chen, L., Mirza, Z.A., Liu, L. 2015. Cr(VI)-contaminated groundwater remediation with simulated permeable reactive barrier (PRB) filled with natural pyrite as reactive material: Environmental factors and effectiveness. *Journal of hazardous materials*, **298**, 83-90.

Livens, F.R., Jones, M.J., Hynes, A.J., Charnock, J.M., Mosselmans, J.F.W., Hennig, C., Steele, H., Collison, D., Vaughan, D.J., Pattrick, R.A.D., Reed, W.A., Moyes, L.N. 2004. X-ray absorption spectroscopy studies of reactions of technetium, uranium and neptunium with mackinawite. *Journal of environmental radioactivity*, **74**, 211-9.

Lu, A., Zhong, S., Chen, J., Shi, J., Tang, J., Lu, X. 2006. Removal of Cr(VI) and Cr(III) from Aqueous Solutions and Industrial Wastewaters by Natural Clino-pyrrhotite. *Environmental Science & Technology*, **40**, 3064-3069.

Lu, X.C., Wang, H.M. 2012. Microbial Oxidation of Sulfide Tailings and the Environmental Consequences. *Elements* **8**, 119-124.

Ma, B., Kang, M., Zheng, Z., Chen, F., Xie, J., Charlet, L., Liu, C. 2014. The reductive immobilization of aqueous Se(IV) by natural pyrrhotite. *Journal of hazardous materials*, **276**, 422-32.

Macingova, E., Luptakova, A. 2012. Recovery of Metals from Acid Mine Drainage. *CHEMICAL ENGINEERING TRANSACTIONS*, **28**, 109-114.

Malakooti, S.J., Tonkaboni, S.Z.S., Noaparast, M., Ardejani, F.D., Naseh, R. 2013. Characterisation of the Sarcheshmeh copper mine tailings, Kerman province, southeast of Iran. *Environmental Earth Sciences*, **71**(5), 2267-2291.

Maree, J.P., Mujuru, M., Bologo, V., Daniels, N., Mpholoane, D. 2013. Neutralisation treatment of AMD at affordable cost. *Water SA*, **39**.

Martínez, C.E., McBride, M.B. 1998. Solubility of Cd^{2+}, Cu^{2+}, Pb^{2+}, and Zn^{2+} in aged coprecipitates with amorphous iron hydroxides. *Environ. Sci. Technol.*, **32**, 743-748.

McArt, S.H., Cook-Patton, S.C., Thaler, J.S. 2012. Relationships between arthropod richness, evenness, and diversity are altered by complementarity among plant genotypes. *Oecologia*, **168**, 1013-1021.

Mehra, O.P., Jackson, M.L. 1960. Iron oxides removed from soils and clays by dithionote–citrate system buffered with sodium bicarbonate. *Clays and Clay Minerals*, **7**, 317–327.

Moon, H.S., Chang, S.W., Nam, K., Choe, J., Kim, J.Y. 2006. Effect of reactive media composition and co-contaminants on sulfur-based autotrophic denitrification. *Environmental pollution (Barking, Essex : 1987)*, **144**, 802-7.

Morrison, L., Feely, M., Stengel, D.B., Blamey, N., Dockery, P., Sherlock, A., Timmins, E. 2009. Seaweed attachment to bedrock: biophysical evidence for a new geophycology paradigm. *Geobiology*, **7**(4), 477-87.

Morse, J.W., Rickard, D. 2004. Peer Reviewed: Chemical Dynamics of Sedimentary Acid Volatile Sulfide. *Environmental Science & Technology*, **38**, 131A-136A.

Moses, C.O., Herman, J.S. 1991. Pyrite oxidation at circumneutral pH. *Geochimica et Cosmochimica Acta*, **55**(2), 471-482.

Moses, C.O., Kirk Nordstrom, D., Herman, J.S., Mills, A.L. 1987. Aqueous pyrite oxidation by dissolved oxygen and by ferric iron. *Geochimica et Cosmochimica Acta*, **51**(6), 1561-1571.

Motsi, T., Rowson, N.A., Simmons, M.J.H. 2009. Adsorption of heavy metals from acid mine drainage by natural zeolite. *International Journal of Mineral Processing*, **92**(1-2), 42-48.

Moyes, L.N., Jones, M.J., Reed, W.a., Livens, F.R., Charnock, J.M., Mosselmans, J.F.W., Hennig, C., Vaughan, D.J., Pattrick, R.a.D. 2002. An X-ray absorption spectroscopy, study of neptunium(V) reactions with mackinawite (FeS). *Environmental Science and Technology*, **36**, 179-183.

Moyes, L.N., Parkman, R.H., Charnock, J.M., Vaughan, D.J., Livens, F.R., Hughes, C.R., Braithwaite, A. 2000. Uranium uptake from aqueous solution by interaction with

goethite, lepidocrocite, muscovite, and Mackinawite: An x-ray absorption spectroscopy study. *Environmental Science and Technology*, **34**, 1062-1068.

Mullet, M., Boursiquot, S., Abdelmoula, M., Genin, J.M., Ehrhardt, J.J. 2002. Surface chemistry and structural properties of mackinawite prepared by reaction of sulfide ions with metallic iron. *Geochimica Et Cosmochimica Acta*, **66**(5), 829-836.

Mullet, M., Boursiquot, S., Ehrhardt, J.-J. 2004. Removal of hexavalent chromium from solutions by mackinawite, tetragonal FeS. *Colloids and Surfaces A: Physicochemical and Engineering Aspects*, **244**, 77-85.

Naveau, A., Monteil-Rivera, F., Guillon, E., Dumonceau, J. 2007. Interactions of aqueous selenium (-II) and (IV) with metallic sulfide surfaces. *Environmental Science and Technology*, **41**, 5376-5382.

Ni, J.A. 1998. *Inorganic and analytical chemistry*. Chemical Industry Press, China.

Nicholson, R.V., Scharer, J.M. 1994. Laboratory studies of pyrrhotite oxidation kinetics. *ACS Symposium Series*. Washington, DC: American Chemical Society,[1974]-. pp. 14-30.

Nicol, M., Miki, H., Basson, P. 2013. The effects of sulphate ions and temperature on the leaching of pyrite. 2. Dissolution rates. *Hydrometallurgy*, **133**, 182-187.

Northey, S., Mohr, S., Mudd, G.M., Weng, Z., Giurco, D. 2014. Modelling future copper ore grade decline based on a detailed assessment of copper resources and mining. *Resources, Conservation and Recycling*, **83**, 190-201.

Oasmaa, a., Elliott, D.C., Mu, S. 2009. XPS Analysis of Sorption of Selenium(IV) and Selenium(VI) to Mackinawite (FeS). *Environmental Progress*, **28**, 404-409.

Oh, S., Kim, K., Choi, H., Cho, J., Kim, I.S. 1998. Kinetics and physiological characteristics of autotrophic dentrification by denitrifying sulfur bacteria. **42**(3-4), 59-68.

Oleszkiewicz, J.A., Barnard, J.L. 2006. Nutrient removal technology in North America and the European Union: a review. *Water quality research journal of Canada*, **41**(4), 449-462.

Ozverdi, A., Erdem, M. 2006. Cu^{2+}, Cd^{2+} and Pb^{2+} adsorption from aqueous solutions by pyrite and synthetic iron sulphide. *J Hazard Mater*, **137**(1), 626-632.

Patterson, R.R., Fendorf, S., Fendorf, M. 1997. Reduction of hexavalent chromium by amorphous iron sulfide. *Environmental Science and Technology*, **31**, 2039-2044.

Pierre Louis, A.-M., Yu, H., Shumlas, S.L., Van Aken, B., Schoonen, M.a.a., Strongin, D.R. 2015. Effect of Phospholipid on Pyrite Oxidation and Microbial Communities under Simulated Acid Mine Drainage (AMD) Conditions. *Environmental Science & Technology*, **49**(13), 7701–7708.

Pu, J., Feng, C., Liu, Y., Li, R., Kong, Z., Chen, N., Tong, S., Hao, C., Liu, Y. 2014. Pyrite-based autotrophic denitrification for remediation of nitrate contaminated groundwater. *Bioresource technology*, **173**, 117-23.

Quan, X., Zhang, M., Lawlor, P.G., Yang, Z., Zhan, X. 2012. Nitrous oxide emission and nutrient removal in aerobic granular sludge sequencing batch reactors. *Water research*, **46**, 4981-90.

Rapln F., T.A., Campbell P. G. C. , Carlgnan R. 1988. Potential Artifacts in the Determination of Metal Partitioning in Sediments by a Sequential Extraction Procedure. *Envlron. Sci. Technol.*, **lS86**(20), 836-840.

Ratcliff, J.J., Wan, A.H.L., Edwards, M.D., Soler-Vila, A., Johnson, M.P., Abreu, M.H., Morrison, L. 2016. Metal content of kelp (Laminaria digitata) co-cultivated with Atlantic salmon in an Integrated Multi-Trophic Aquaculture system. *Aquaculture*, **450**, 234-243.

Rau, G.H., Knauss, K.G., Langer, W.H., Caldeira, K. 2007. Reducing energy-related CO_2 emissions using accelerated weathering of limestone. *Energy*, **32**(8), 1471-1477.

Raven, K.P., Jain, A., Loeppert, R.H. 1998. Arsenite and arsenate adsorption on ferrihydrite: kinetics, equilibrium, and adsorption envelopes. *Environment Science Technology*, **32**(3), 344-349.

Renock, D., Gallegos, T., Utsunomiya, S., Hayes, K., Ewing, R.C., Becker, U. 2009. Chemical and structural characterization of As immobilization by nanoparticles of mackinawite (FeSm). *Chemical Geology*, **268**, 116-125.

Rickard, D., Luther, G.W. 2007. Chemistry of iron sulfides. *Chemical reviews*, **107**, 514-62.

Rimstidt, J.D., Vaughan, D.J. 2003. Pyrite oxidation: a state-of-the-art assessment of the reaction mechanism. *Geochimica et Cosmochimica Acta*, **67**, 873-880.

Romero, F.M., Nunez, L., Gutierrez, M.E., Armienta, M.A., Ceniceros-Gomez, A.E. 2011. Evaluation of the potential of indigenous calcareous shale for neutralization and removal of arsenic and heavy metals from acid mine drainage in the Taxco mining area, Mexico. *Arch Environ Contam Toxicol*, **60**(2), 191-203.

Sánchez, E.J., López, P.E., Santofimia, P.E., Reyes, A.J., Martín, R.J.A. 2006. The Removal of Dissolved Metals by Hydroxysulphate Precipitates during Oxidation and Neutralization of Acid Mine Waters, Iberian Pyrite Belt. *Aquatic Geochemistry*, **12**(3), 269-298.

Safarzadeh, M.S., Bafghi, M.S., Moradkhani, D., Ojaghi Ilkhchi, M. 2007. A review on hydrometallurgical extraction and recovery of cadmium from various resources. *Minerals Engineering*, **20**(3), 211-220.

Sahinkaya, E., Dursun, N., Kilic, A., Demirel, S., Uyanik, S., Cinar, O. 2011a. Simultaneous heterotrophic and sulfur-oxidizing autotrophic denitrification process for drinking water treatment: control of sulfate production. *Water research*, **45**, 6661-7.

Sahinkaya, E., Gunes, F.M., Ucar, D., Kaksonen, A.H. 2011b. Sulfidogenic fluidized bed treatment of real acid mine drainage water. *Bioresource technology*, **102**, 683-9.

Sahinkaya, E., Kilic, A., Duygulu, B. 2014. Pilot and full scale applications of sulfur-based autotrophic denitrification process for nitrate removal from activated sludge process effluent. *Water Research*, **60** 210–217.

Sahoo, P.K., Tripathy, S., Panigrahi, M.K., Equeenuddin, S.M. 2013. Inhibition of Acid Mine Drainage from a Pyrite-rich Mining Waste Using Industrial By-products: Role of Neo-formed Phases. *Water, Air, & Soil Pollution*, **224**.

Sainz, A., Ruiz, F. 2006. Influence of the very polluted inputs of the Tinto–Odiel system on the adjacent littoral sediments of southwestern spain: A statistical approach. *Chemosphere*, **62**(10), 1612-1622.

Scheinost, A.C., Charlet, L. 2008. Selenite Reduction by Mackinawite, Magnetite and Siderite: XAS Characterization of Nanosized Redox Products. *Environmental Science & Technology*, **42**(6), 1984-1989.

Schippers, A., Jørgensen, B.B. 2002. Biogeochemistry of pyrite and iron sulfide oxidation in marine sediments. *Geochimica et Cosmochimica Acta*, **66**(1), 85-92.

Scott, T.B., Riba Tort, O., Allen, G.C. 2007. Aqueous uptake of uranium onto pyrite surfaces; reactivity of fresh versus weathered material. *Geochimica et Cosmochimica Acta*, **71**, 5044-5053.

Sdiri, A., Higashi, T., Chaabouni, R., Jamoussi, F. 2011. Competitive Removal of Heavy Metals from Aqueous Solutions by Montmorillonitic and Calcareous Clays. *Water, Air, & Soil Pollution*, **223**(3), 1191-1204.

Shao, M.F., Zhang, T., Fang, H.H.P. 2010. Sulfur-driven autotrophic denitrification: diversity, biochemistry, and engineering applications. *Applied microbiology and biotechnology*, **88**, 1027-42.

Shi, X., Sun, K., Balogh, L.P., Baker Jr, J.R. 2006. Synthesis, characterization, and manipulation of dendrimer-stabilized iron sulfide nanoparticles. *Nanotechnology*, **17**, 4554-4560.

Shi, Y.D., Chen, T.H., Wang, Y.M., Wang, J. 2010. The evolution of crystal structure and arsenic content of pyrite calcined under N2 atmosphere. *Acta Mineralogica Sinica*, **S1**, 231-231.

Shipley, H.J., Engates, K.E., Grover, V.A. 2013. Removal of Pb(II), Cd(II), Cu(II), and Zn(II) by hematite nanoparticles: effect of sorbent concentration, pH, temperature, and exhaustion. *Environ Sci Pollut Res Int*, **20**(3), 1727-36.

Shokri, B.J., Ramazi, H., Ardejani, F.D., Moradzadeh, A. 2013. A statistical model to relate pyrite oxidation and oxygen transport within a coal waste pile: case study, Alborz Sharghi, northeast of Iran. *Environmental Earth Sciences*, **71**(11), 4693-4702.

Sierra-Alvarez, R., Beristain-Cardoso, R., Salazar, M., Gómez, J., Razo-Flores, E., Field, J.A. 2007. Chemolithotrophic denitrification with elemental sulfur for groundwater treatment. *Water research*, **41**, 1253-62.

Smith, B.A., Teel, A.L., Watts, R.J. 2004. Identification of the Reactive Oxygen Species Responsible for Carbon Tetrachloride Degradation in Modified Fenton's Systems. *Environmental Science & Technology*, **38**, 5465-5469.

Smith, C.J., Danilowicz, B.S., Clear, A.K., Costello, F.J., Wilson, B., Meijer, W.G. 2005. T-Align, a web-based tool for comparison of multiple terminal restriction fragment length polymorphism profiles. *FEMS Microbiology Ecology*, **54**, 375-380.

Snowball, I., Torri, M. 1999. Incidence and significance of magnetic iron sulphides. in: *Quaternary Climates , Environments and Magnetism.*, pp. 199-230.

Sorokin, D.Y., Tourova, T.P., Muyzer, G. 2005. Oxidation of thiosulfate to tetrathionate by an haloarchaeon isolated from hypersaline habitat. *Extremophiles*, **9**(6), 501-4.

Steger, H.F. 1982. Oxidation of sulfide minerals: VII. Effect of temperature and relative humidity on the oxidation of pyrrhotite. *Chemical Geology*, **35**(3-4), 281-295.

Stephen, Y., Rainford, H., Jha, A. 2012. A novel low-energy route for the extraction of copper and cobalt metals/alloys from the Zambian sulphide concentrates.

Stookey, L.L. 1970. Ferrozine—a new spectrophotometric reagent for iron. *Analytical Chemistry*, **42**(7), 779-781.

Sun, H., Chen, M., Zou, L., Shu, R., Ruan, R. 2015. Study of the kinetics of pyrite oxidation under controlled redox potential. *Hydrometallurgy*, **155**, 13-19.

Tabak, H.H., Burckle, J., Kawahara, F.K., Govind, R., Scharp, R. 2003. Advances in biotreatment of acid mine drainage and biorecovery of metals: 1. Metal precipitation for recovery and recycle *Biodegradation*, **14**, 423-436.

Tchobanoglous, G., Burton, F.L., Stensel, H.D. 2004. *Wastewater Engineering –Treatment and reuse.* Metcalf and Eddy, Inc. McGraw-Hill, New York, USA.

Teel, A.L., Watts, R.J. 2002. Degradation of carbon tetrachloride by modified Fenton's reagent. *Journal of Hazardous Materials*, **94**, 179-189.

Tessier, A., Campbell, P.G.C., Bisson, M. 1979. Sequential extraction procedure for the speciation of particulate trace metals. *Analytical Chemistry*, **51**(7), 844-851.

Tetsuro, K., Shuzo, T. 2012. Biological Removal and Recovery of Toxic Heavy Metals in Water Environment. *Critical Reviews in Environmental Science and Technology*, **42**(10), 1007-1057.

Thomas, J.E., Smart, R.S.C., Skinner, W.M. 2000. Kinetic factors for oxidative and non-oxidative dissolution of iron sulfides. *Minerals Engineering*, **13**(10–11), 1149-1159.

Todd, E.C., Sherman, D.M., Purton, J.A. 2003a. Surface oxidation of pyrite under ambient atmospheric and aqueous (pH = 2 to 10) conditions: electronic structure and

mineralogy from X-ray absorption spectroscopy. *Geochimica et Cosmochimica Acta*, **67**, 881-893.

Todd, E.C., Sherman, D.M., Purton, J.A. 2003b. Surface oxidation of pyrite under ambient atmospheric and aqueous (pH = 2 to 10) conditions: electronic structure and mineralogy from X-ray absorption spectroscopy. *Geochimica et Cosmochimica Acta*, **67**(5), 881-893.

Tong, S., Rodriguez-Gonzalez, L.C., Feng, C., Ergas, S.J. 2016. Comparison of Sulfur Oxidizing Denitrification (SOD) and Particulate Pyrite Autotrophic Denitrification (PPAD) for Treatment of Nitrified Wastewater. *Water Science and Technology*.

Torrentó, C., Cama, J., Urmeneta, J., Otero, N., Soler, A. 2010. Denitrification of groundwater with pyrite and Thiobacillus denitrificans. *Chemical Geology*, **278**, 80-91.

Torrentó, C., Urmeneta, J., Otero, N., Soler, A., Viñas, M., Cama, J. 2011. Enhanced denitrification in groundwater and sediments from a nitrate-contaminated aquifer after addition of pyrite. *Chemical Geology*, **287**, 90-101.

Tuncuk, A., Stazi, V., Akcil, A., Yazici, E.Y., Deveci, H. 2012. Aqueous metal recovery techniques from e-scrap: Hydrometallurgy in recycling. *Minerals Engineering*, **25**(1), 28-37.

Utgikara, V., Chena, B.-Y., Tabaka, H.H., Bishopa, D.F., Govindb, R. 2000. Treatment of acid mine drainage: I. Equilibrium biosorption of zinc and copper on non-viable activated sludge. *International Biodeterioration & Biodegradation*, **46**, 19-28.

Veeramani, H., Scheinost, A.C., Monsegue, N., Qafoku, N.P., Kukkadapu, R., Newville, M., Lanzirotti, A., Pruden, A., Murayama, M., Hochella Jr., M.F. 2013. Abiotic Reductive Immobilization of U(VI) by Biogenic Mackinawite. *Environ Sci Technol*, **47**(5), 2361–2369.

Vidal, M., Santos, M.J., Abrão, T., Rodríguez, J., Rigol, A. 2009. Modeling competitive metal sorption in a mineral soil. *Geoderma*, **149**(3-4), 189-198.

Wang, S., Liang, P., Wu, Z., Su, F., Yuan, L., Sun, Y., Wu, Q., Huang, X. 2015. Mixed sulfur-iron particles packed reactor for simultaneous advanced removal of nitrogen and phosphorus from secondary effluent. *Environ Sci Pollut Res Int*, **22**(1), 415-24.

Watson, J.H.P., Cressey, B.A., Roberts, A.P., Ellwood, D.C., Charnock, J.M., Soper, A.K. 2000. Structural and magnetic studies on heavy-metal-adsorbing iron sulphide nanoparticles produced by sulphate-reducing bacteria. *Journal of Magnetism and Magnetic Materials*, **214**, 13-30.

Watson, J.H.P., Ellwood, D.C., Deng, Q., Mikhalovsky, S., Haytert, C.E., Evanst, J. 1995. Heavy metal adsorption on bacterially producted FeS. *Minerals Engineering*, **8**(10), 1097-1108.

Wei, F.S., Qi, W.Q. 2002. *Monitoring and analysis method of water and waste water*. China Environmental Science Press, China.

Weigel, B.L., Erwin, P.M. 2016. Intraspecific Variation in Microbial Symbiont Communities of the Sun Sponge, Hymeniacidon heliophila, from Intertidal and Subtidal Habitats. *Applied and Environmental Microbiology*, **82**(2), 650-658.

Wersin, P., Hochella, M.F., Persson, P., Redden, G., Leckie, J.O., Harris, D.W. 1994. Interaction between aqueous uranium (VI) and sulfide minerals: Spectroscopic evidence for sorption and reduction. *Geochimica et Cosmochimica Acta*, **58**, 2829-2843.

Wharton, M.J., Atkins, B., Charnockab, J.M., Livens, F.R., Pattrick, R.A.D., Collison, D. 2000. An X-ray absorption spectroscopy study of the coprecipitation of Tc and Re with mackinawite (FeS). *Applied Geochemistry*, **15**, 347-354.

WHO. 2005. Nickel in drinking water: background document for development of WHO. *Guidelines for drinking water quality*.

Widler, A.M., Seward, T.M. 2002. The adsorption of gold(I) hydrosulphide complexes by iron sulphide surfaces. *Geochimica et Cosmochimica Acta*, **66**(3), 383-402.

Widlera, A.M., Seward, T.M. 2002. The adsorption of gold (I) hydrosulphide complexes by iron sulphide surfaces. **66**, 383-402.

Wilkie, J.A., Hering, J.G. 1996. Adsorption of arsenic onto hydrous ferric oxide: effects of adsorbate/adsorbent ratios and co-occurring solutes. *Colloids and Surfaces A: Physicochemical and Engineering Aspects*, **107**(0), 97-110.

Wolthers, M., Charlet, L., van Der Linde, P.R., Rickard, D., van Der Weijden, C.H. 2005a. Surface chemistry of disordered mackinawite (FeS). *Geochimica et Cosmochimica Acta*, **69**(14), 3469-3481.

Wolthers, M., Charlet, L., van Der Weijden, C.H., van der Linde, P.R., Rickard, D. 2005b. Arsenic mobility in the ambient sulfidic environment: Sorption of arsenic(V) and arsenic(III) onto disordered mackinawite. *Geochimica et Cosmochimica Acta*, **69**, 3483-3492.

World Health Organization. 2005. Nickel in drinking water: background document for development of WHO World Health Organization

Wu, D., Ekama, G.A., Wang, H.-G., Wei, L., Lu, H., Chui, H.-K., Liu, W.-T., Brdjanovic, D., van Loosdrecht, M.C., Chen, G.-H. 2014. Simultaneous nitrogen and phosphorus removal in the sulfur cycle-associated Enhanced Biological Phosphorus Removal (EBPR) process. *Water research*, **49**, 251-264.

Xie, Q.Q., Chen, T.H., Fan, Z.L.e.a. 2014. Morphological characteristics and genesis of colloform pyrite in Xinqiao Fe-S deposit, Tongling, Anhui Province (in Chinese). *Scientia Sinica Terrae*, **44**, 2665–2674.

Xiong, Z., He, F., Zhao, D., Barnett, M.O. 2009. Immobilization of mercury in sediment using stabilized iron sulfide nanoparticles. *Water Res*, **43**(20), 5171-9.

Yang, W., Zhao, Q., Lu, H., Ding, Z., Meng, L., Chen, G.-H. 2015. Sulfide-driven autotrophic denitrification significantly reduces N2O emissions. *Water research*, **90**, 176-184.

Yang, Y., Chen, T., Li, P., Liu, H., Xie, J., Xie, Q., Zhan, X. 2014a. Removal and recovery of Cu and Pb from single-metal and Cu–Pb–Cd–Zn multimetal solutions by modified pyrite: fixed-bed columns. *Industrial & Engineering Chemistry Research*, **53**(47), 18180-18188.

Yang, Y., Chen, T., Li, P., Xie, Q., Zhan, X. 2016. Cu Removal from Acid Mine Drainage by Modified Pyrite: Batch and Column Experiments. *Mine Water and the Environment*.

Yang, Z., Kang, M., Ma, B., Xie, J., Chen, F., Charlet, L., Liu, C. 2014b. Inhibition of U(VI) reduction by synthetic and natural pyrite. *Environmental science & technology*, **48**(18), 10716–10724.

Yin, J., Zhang, P., Li, F., Li, G., Hai, B. 2015. Simultaneous biological nitrogen and phosphorus removal with a sequencing batch reactor–biofilm system. *International Biodeterioration & Biodegradation*.

Yousefi, S., Ardejani, F.D., Ziaii, M., Abedi, A., Zadeh, E.E. 2014. Investigating the origin and geochemical behaviour of toxic elements within the waste dumps using statistical analyses: a case study at waste dumps of Sarcheshmeh copper mine, SE of Iran. *Environmental Earth Sciences*, **73**(4), 1555-1572.

Zhang, M. 2011. Adsorption study of Pb(II), Cu(II) and Zn(II) from simulated acid mine drainage using dairy manure compost. *Chemical Engineering Journal*, **172**(1), 361-368.

Zhang, S., Xue, X., Liu, X., Duan, P., Yang, H., T., J., Wang, D., Liu, R. 2006. Current Situation and comprehensive utilization of iron ore tailing resources. *Journal of Mining Science*, **42**(4), 403-408.

Zhang, W.Y., Fang, M.X., Zhang, W.W., Xiao, C., Zhang, X.Q., Yu, Z.P., Zhu, X.F., Wu, M. 2012. Extensimonas vulgaris gen. nov., sp. nov., a novel member of the family Comamonadaceae. *International Journal of Systematic and Evolutionary Microbiology*, 2062-2068.

Zhang, Y., Tran, H.P., Hussain, I., Zhong, Y., Huang, S. 2015. Degradation of p-chloroaniline by pyrite in aqueous solutions. *Chemical Engineering Journal*, **279**, 396-401.

Zhang, Y., Zhang, K., Dai, C., Zhou, X., Si, H. 2014. An enhanced Fenton reaction catalyzed by natural heterogeneous pyrite for nitrobenzene degradation in an aqueous solution. *Chemical Engineering Journal*, **244**, 438-445.

Zhao, Y.C., Stanforth, R. 2000. Production of Zn powder by alkaline treatment of smithsonite Zn–Pb ores. *Hydrometallurgy*, **56**, 237–249.

Zou, G., Papirio, S., Lakaniemi, A.-M., Ahoranta, S.H., Puhakka, J.A. 2016. High rate autotrophic denitrification in fluidized-bed biofilm reactors. *Chemical Engineering Journal*, **284**, 1287-1294.

Zouboulis, A.I., Kydros, K.A., Matis, K.A. 1995. Removal of hexavalent chromium anions from solutions by pyrite fines. *Water Research*, **29**, 1755-1760.